Commissioning, Benchmarking and Clinical Application of a Novel Fiber Optic CT Scanner for

Precise Three-Dimensional Radiation Dosimetry

Yi-Fang Wang

Submitted in partial fulfillment of the
requirements for the degree of
Doctor of Philosophy
under the Executive Committee
of the Graduate School of Arts and Sciences

COLUMBIA UNIVERSITY

2024

Abstract

Commissioning, Benchmarking and Clinical Application of a Novel Fiber Optic CT Scanner for

Precise Three-Dimensional Radiation Dosimetry

Yi-Fang Wang

Radiotherapy is a prominent cancer treatment modality in medicine, aiming to deliver adequate doses to the target while minimizing harm to healthy tissue. Recent advancements in computer technology, machine engineering, and imaging have facilitated intricate treatment planning and accurate radiation administration. These advancements have allowed for more precise dose distributions to be delivered to cancer patients. However, even small discrepancies in setup or delivery can result in significant dose variations. While treatment planning systems provide 3D dose calculations, there is currently a lack of 3D measurement tools in the clinic to verify the accuracy of dose calculation and delivery. Presently, medical physicists rely on 2D dose plane comparisons with treatment planning calculations using gamma index analyses. However, these results do not directly correlate with clinical dose-volume constraints, and detecting delivery errors using 1D or 2D dosimetry is challenging. The implementation of 3D dosimetry not only ensures the safety of radiation treatment but also facilitates the development of new emerging radiation treatment techniques. This study aims to commission and validate a clinically viable optical scanner for 3D dosimetry and apply the developed system to address current clinical and pre-clinical challenges, thereby advancing our understanding of treatment uncertainties in modern radiotherapy.

The optical CT scanner that was developed comprises four key components: an LED illuminator, an aquarium with matching fluid, a fiber optic taper, and a CCD camera. The LED illuminator emits uniform and parallel red light at a peak wavelength of 625 nm and a full width at half maximum (FWHM) of 20 nm in continuous mode. The aquarium is constructed with transparent acrylic walls and is designed to accommodate the 3D dosimeter PRESAGE, which can be fixed on a rotation stage inside the tank. Clear acrylic has excellent optical clarity and light transmission, with a refractive index of 1.49 that is close to the average refractive index (1.54) of PRESAGE. To match the refractive index of the 3D dosimeters, a matching liquid composed of 90% Octyl Salicylate and 10% Octyl-P-Methoxy Cinnamate is filled in the tank. The fiber optic taper serves two functions: first, it demagnifies the projection images while preserving their shape, and second, it effectively reduces the acceptance angle of the light reaching the CCD camera. The CCD camera used in the system is an Allied Vision model with a resolution of 0.016 mm, capable of acquiring 2D projection images from various angles. The principle of the optical CT scanner follows that of CT imaging, where 2D projection images from different angles are used to reconstruct volumetric 3D dose images using the filtered back projection technique. To validate the dosimetric measurements and assess the uncertainties of the 3D dosimetry system, 21 benchmark experiments, including mechanical, imaging, and dosimetry tests were conducted. Furthermore, the developed system was employed for various applications, including patient-specific IMRT QA, small field dosimetry using kilovoltage and megavoltage beams, as well as end-to-end testing of stereotactic radiosurgery.

A comprehensive analysis assessed uncertainties in each scanner component. Mechanical tests showed maximum uncertainties below 1%. By employing background subtraction and

calibration techniques, measurement uncertainty was reduced to <1% in the optimal dose range. Background subtraction resulted in a remarkable 77% reduction in uncertainty by mitigating artifacts, ambient light, and refractive light. Reproducibility was excellent, with mean and standard deviation of dose differences below 0.4% and 1.1%, respectively, in three repeat scans. Dose distribution measurements exhibited strong agreement (passing rates: 98%-100%) between 3D measurements, treatment planning calculations, and EBT3 film dosimetry. Results confirm the optical CT scanner's robustness and accuracy for clinical 3D radiation dosimetry. The study also demonstrates that the developed 3D dosimetry system surpasses the limitations of traditional 2D gamma tests by providing clinicians with more clinically relevant information. This includes measured dose-volume histograms (DVHs) and the evaluation of gamma failing points in 3D space, enabling a comprehensive assessment of individual treatment plans. Furthermore, the study showcased the feasibility of utilizing this system to characterize a radiosurgery platform. It successfully assessed mechanical and dosimetric errors in off-axis delivery and evaluated the accuracy of treatment planning dose calculations, including modeling small fields, out-of-field dose, and multi-leaf collimator (MLC) characteristics. In addition, compelling evidence was presented that the high-resolution 3D dosimeter used in this study is capable of accurate dosimetry for both megavoltage and kilovoltage small fields. Importantly, the dosimeter exhibits no energy or dose rate dependence, further supporting its reliability and suitability for precise dosimetry measurements.

The intricate and three-dimensional nature of dose distributions in modern radiotherapy necessitated the development of 3D dosimetry measurements, particularly for treatments with precise margins, such as SRS and SBRT. The newly developed 3D dosimetry system offers

significant enhancements to current QA practices, delivering more clinically relevant comparison results and bolstering patient safety. Furthermore, it can be utilized for independent inspections across multiple institutions or remote dosimetry verification. Beyond its applications in clinical settings, the presented 3D dosimetry system holds the potential to expedite the development and utilization of novel radiation platforms.

Table of Contents

List of Charts, Graphs, Illustrations

Acknowledgments

I am deeply indebted to the countless individuals whose unwavering support and encouragement have made the completion of this doctoral thesis possible. Words cannot adequately express my profound gratitude and admiration for my esteemed PhD advisor, Professor Cheng-Shie Wuu. His invaluable guidance and unwavering commitment have not only shaped me into an independent researcher but also ignited my passion for both research and clinical practice in the field of medical physics. It is through his mentorship that I have acquired the necessary skills and determination to navigate the obstacles and triumph over the challenges that lie ahead in my career. I am truly honored and privileged to have had the opportunity to learn from Professor Wuu, and I extend my heartfelt appreciation for his exceptional guidance and support throughout this journey.

I am profoundly grateful to Dr. John Admovics for his invaluable contributions to this doctoral thesis. The innovative approach and unwavering dedication he displayed in developing the 3D dosimeter, PRESAGE, used for 3D radiation dosimetry, have truly inspired me. Throughout the past few years, his guidance and expertise have played a vital role in shaping this research. Dr. Admovics' consistent involvement and collaborative efforts have been essential in refining the formulation of PRESAGE, leading to the achievement of optimal dosimetric outcomes. His passion for scientific exploration has left a lasting impression on me, serving as a constant reminder to approach research with enthusiasm and dedication.

I would like to express my heartfelt gratitude to the esteemed members of my thesis advisory and examination committee, Professors Ismail C. Noyan and Marco Zaider. Their selfless dedication and valuable contributions have been instrumental in shaping the outcome of my research. I am deeply grateful for the time and effort they have generously invested in providing

understanding and flexibility in accommodating my academic pursuits alongside my clinical responsibilities have been invaluable.

I would also like to acknowledge and thank my esteemed medical physics colleagues at the department. Dr. Yuanguang Xu and Mr. Carl Elliston have been invaluable collaborators in our 3D dosimetry research, particularly in the application of Gamma knife and FLASH radiotherapy. Their expertise and insights have greatly influenced and enhanced my thesis work, providing solutions to challenges encountered along the way. Their guidance and collaboration have been indispensable to the overall success of my research. Furthermore, I extend my appreciation to Ms. Michelle Savacool for her extensive clinical knowledge and valuable perspectives. Her instruction and guidance have significantly shaped the relevance and applicability of my research in the clinical setting. Her insights have bridged the gap between theory and practice, allowing me to develop a deeper understanding of the practical implications of my work. Additionally, I would like to acknowledge and thank Dr. Reshma Munbodh for her exceptional mentorship throughout my academic journey. Her guidance in academic writing and research project initiation has been invaluable. I am grateful for her continued support and for sharing her knowledge and expertise, which have greatly contributed to my growth as a researcher.

Furthermore, I would like to express my sincere appreciation to all my friends in both the United States and Taiwan. Their companionship, laughter during joyful moments, and unwavering support during challenging times have been invaluable. Without their presence and encouragement, I would not have been able to navigate the difficulties and obstacles encountered along my journey. I am especially grateful for my husband, Shih-Chi Lin, who has been an incredible pillar of support in my life. He has taken care of me during times of illness and provided comfort and solace when I have felt down. His unwavering love and inspiration have propelled me

to become a better person. Furthermore, I want to extend my thanks to my entire family, including my parents and grandparents, who have unconditionally supported my decision to come to the United States. Despite the distance, their love and support have remained constant. They are the ones who may see me less frequently but love me unconditiona

Chapter 1

General Introduction

1.1 The Role of Radiation Dosimetry in Modern Radiotherapy

Radiation dosimetry, the process of quantifying the effects of ionizing radiation, holds immense significance within radiation oncology clinics. The clinical outcomes of patients are directly linked to the dose they receive. Tumor-control curves and normal tissue complication curves illustrate the impact of dose escalation on tumor control and normal tissue damage. Maximizing the disparity between these curves determines the optimal prescribed dose, underscoring the need for accurate dosimetry in radiotherapy to administer clinically meaningful doses without harm[1, 2, 3].

Currently, there are two major methodologies to quantify the radiation in the clinic, computer-based dose calculation using analytical models or Monte Carlo (MC) simulations and radiation dose measurements using radiation dosimeters. Computer-based dose calculation, employing analytical models or Monte Carlo simulations, focuses on treatment planning. Radiation oncologists delineate treatment targets and organs at risk (OAR) on patients' CT scans, with dosimetrists optimizing and calculating doses using the treatment planning system (TPS)[4, 5, 6]. Radiation dose measurements using dosimeters are primarily carried out by medical physicists. This methodology encompasses dosimetry quality assurance (QA) for treatment machines, in-vivo dosimetry, and patient-specific dose measurements. The results obtained from radiation measurements are used to verify dose calculations from the TPS, ensuring the safe delivery of doses to patients[7, 8].

Over the past decade, computer-based dose calculation has undergone significant advancements, transitioning from one-dimensional (1D) correction-based algorithms to three-dimensional (3D) kernel-based algorithm[9] or numerical Linear Boltzmann Transport Equation (LBTE) solvers[10, 11]. The numerical method has improved the modeling of secondary electron

2

transport, thus increasing the accuracy of heterogeneity correction. In addition, it can provide the dose deposition in high-Z implanted materials and report the dose as dose to medium[12]. The rapid advancement of dose calculation algorithms, combined with the state-of-the-art delivery and imaging system, facilitate the complex treatment delivery, such as intensity modulated radiotherapy (IMRT), stereotactic body radiation therapy (SBRT)[13], and stereotactic radiation surgery (SRS)[14]. More conformal dose distribution can be delivered to the treatment targets, thus sparing adjacent OARs.

In contrast to computer-based dose calculation, radiation dosimetry in clinical settings primarily involves point dose or two-dimensional (2D) dose distribution measurement[15, 16]. Ion chambers are the most commonly used standard, reference dosimeter in the clinics due to its stability and accuracy. The calibration coefficient of the chambers can be determined by American Association of Physicists in Medicine (AAPM) Accredited Dosimetry Calibration Laboratory (ADCL) through a reference chamber, calibrated by the National Institute of Standards and Technology (NIST) water calorimeter, or a NIST-calibrated source[17]. The main clinical purpose of the ion chamber is to calibrate the output of the treatment machine. For example, farmer chambers are used to calibrate the absorbed dose to water in the user's photon and electron beam quality through Task Group 51 (TG-51)[18]. Once the output of the treatment machine is known, all the other dosimeters can be calibrated using the treatment machine. Other dosimeters commonly used in the clinics include radiochromic film (RCF)[19], optical stimulated luminescence dosimetry (OSLD)[20, 21], diodes, electronic portal imaging device (EPID)[22] and metal-oxide semiconductor field-effect transistor (MOSFET)[23]. RCF, EPID, and diode arrays can provide 2D dose distributions, while the others are primarily used for point dose measurements. All of these dosimeters require known doses to be delivered by the treatment machine for calibration purposes.

2D dosimeters are generally employed for machine QA, commissioning, and patient-specific quality assurance (PSQA). RCF darkens with absorbed dose due to radiation-induced polymerization of diacetylene molecules and the formation of polydiacetylene dye polymers. Although RCF can provide high resolution 2D dose distribution, its measurement process is labor-intensive and time-consuming. The accuracy of the measurement relates to the handling and calibration methods, calibration curves, dose conversion methods, correction methodologies, and operation of the readout system. Unlike RCF, 2D diode devices can provide instant readout of the dose distribution and are extensively used in the clinics for TPS commissioning, flatness, and symmetry measurements of the treatment machines, and IMRT PSQA. Because of their high sensitivity, excellent reproducibility and mechanical stability can be achieved. The small sensitive volumes allow them to measure highly modulated dose distributions8.

In modern radiotherapy, the development of machine and software engineering, such as multi leaf collimators (MLC) and imaging technology, such as linear accelerator (LINAC)-integrated cone-beam computed tomography (CBCT) has facilitated advanced treatment delivery. IMRT allows an optimal dose distribution delivered precisely through diverse and complicated beam combinations delivered by MLC. SBRT and SRS utilize rapid dose fall-off and imaging guidance technologies to deliver high dose to the treatment targets, while sparing OARs. Compared to the traditional 3D radiotherapy, smaller margins are prescribed to the treatment targets and more modulated dose are delivered to the patients, meaning that small setup or delivery discrepancies could lead to a large dose difference. In addition, due to the complex delivery system, machine or dosimetry errors are less likely to be detected and have more significant impacts on the patients. 3D dosimetry can provide a comprehensive view of the complex 3D dose clouds delivered to the patient, providing detailed information of the patient's treatments and detecting

4

treatment errors. For example, by combining the measured 3D dose distribution with the patient's structures information, the actual target coverage and normal tissue sparing can be measured, thus improving clinical judgements. Besides the application of treatment verification, 3D dosimetry can be used to verify new radiation delivery techniques or treatment platforms. Although 3D dosimetry methodologies have been investigated and described in many publications for more than twenty years, they are not currently used in the clinic due to the limitations of efficiency and accuracy. A new type of 3D dosimetry system is necessary to facilitate the advancement of modern radiation dosimetry.

1.2 Brief History and Description of the Optical CT Scanner (OCT) and 3D Dosimeters

In 1996, the methodology of using an optical scanner to determine the 3D dose distribution in irradiated gels was proposed by Gore et al[24]. The optical scanner incorporates an He-Ne laser with 632 nm wavelength, water tank, photodiode detectors, and a rotating gel platform. The attenuation of a monochromic light beam, caused by scattering, passing through the irradiated optically turbid medium is directly related to the radiation dose delivered to the medium. The principle employed for deriving the 3D dose distribution is similar to the X-ray CT. Filtered back projection was used to reconstruct the 3D dose distribution from the line projections taken from different angles and slices. It was discovered that differences between the refractive index of the water, plastic wall of the cylindrical vessel of the dosimeter, and the polymer gel could result in spatial and angular deflection of the beam, and thus results in measurement uncertainties. The largest spatial and angular deflections occur when the laser beam approaches the edge of the vessel. To minimize these deflections, the refraction index of the water was adjusted by adding a dyeing material such as propylene glycol or glycerol to match the refraction index of the gel. The spatial

resolution of the measured dose matrix depends on the width of the laser beam, alignment of the axis of platform rotation with the midpoint of the translational scan, backlash of the motors, and the reconstruction filter. By reconstructing a 0.6 mm tube containing ink, the resolution was measured to be 3.25 mm. The reconstructed dose images had a standard deviation of 3.5%. During the same time, the optical properties of the BANG polymer gel was also published. The dose-response mechanism relies on the production of light-scattering polymer micro-particles in the gel at each site of radiation absorption. The attenuation of transmitted light cause by the scattering is directly related to the dose and independent of dose rate. At 500 nm, the attenuation coefficient increases by 0.7 mm^{-1}, when the dose increases from 0 to 5 Gy.

In 2004, the performance of a commercial optical CT scanner, OCTOPUS (MGS Research, Inc. Madison, CT), and BANG polymer gel was published[25]. Various sources of noise, including digitization, electronic, optical, and mechanical generated by the scanner were identified. In addition, the optical uniformity of the polymer gel and the reproducibility of the data acquisition process were analyzed. It was demonstrated that an overall uncertainty of 3% within approximately 75% of the radius of the container was introduced by the scanner, the gel, and its container. Small particles of dust on the lenses, photoelectric conversion factor at different spots of the photodetector, light reflection, and refraction near the cylinder wall, and optical nonuniformity of the container wall. The study compared the dose distribution of a 5-field coplanar 3D conformal plan from the optical scanner, treatment planning system, and the films. Although the 40 percent isodose lines from the gel measurements were distorted because of the refractive artifact, the gel measurements agree with the plan and the film within the "3% or 2 mm" criterion throughout the artifact-free central region.

Despite the promising preliminary results, there were still some fundamental issues of using gels as 3D dosimeters. For polymer gels, the attenuation of the transmitted beam is mainly caused by light scattering from the radiation induced optical contrast. The presence of scattering was shown to systematically influence the magnitude of the reconstructed attenuation coefficients. One study has shown that the scattering can cause significant depression (>10%) on the reconstructed images[26]. Secondly, the radiochromic gel dosimeter has the issue of radiochromic diffusion over the time. Lastly, the wall of the gel dosimeter can cause significant reflection and refraction artifacts around the edge of the dosimeter. In 2006, an optically clear 3D polyurethane dosimeter formulated with a halogenated hydrocarbon free radical initiator and a leuco dye, PRSAGE (Heuris Inc.), was developed[27,28,29]. The main material of PRESAGE is polyurethane, which consists of 61% carbon, 20% oxygen, 10% nitrogen, and 9% hydrogen. It has an effective atomic number of 6.6 and a density of 1.05 g/cm3. In addition, PRESAGE dosimeters are made up of leucomalachite green (LMG) dye and a halocarbon radical initiator. The free radicals created from halocarbon radiolysis and oxidization during radiation interaction change the LMG into malachite green (MG) which has a maximum absorbance at 633 nm which is detected by the OCT scanner. The advantages of the dosimeter include insensitivity to oxygen and diffusion, radiation induced light absorption rather than scattering, great variety of sensitivity, temporal stability, dose rate independent, tissue equivalence in the range of megavoltage energies, which is suitable for radiotherapy, and linear dose response. In addition, the issue of reflection and refraction artifacts from the wall can be resolved because the dosimeter doesn't require a container to maintain its shape.

Although OCTOPUS optical scanner has capability to produce clinically acceptable dose distribution, the raster scanning takes more than 10 hours. The process is time consuming and not

optimal for clinical use. In 2010, a commercial cone-beam optical CT scanner, Vista (Modus Medical Device Inc.) was developed to reduce the readout time[30]. The duration of the scan was shorter than 5 minutes with 2 hour warm up time and 30 minutes post-irradiation wait time. However, even with the use of custom-side blockers for stray light reduction, the stray light perturbation from the angled scattering was not acceptable. Modification of the optical scanner was presented by Granton et al to reduce the stray light contamination[31]. The scanner was modified by moving the spectral filter from the detector to the source, changing the light spatial fluence pattern, and lowering the acceptance angle by extending the distance between the source and the dosimeter. The modification reduced the stray-to-primary ratio (SPR) significantly from 0.24 to 0.06. However, using this design, the scanner was doubled in length, width and height, requiring brighter light source or longer exposure time. In addition, other sources of artifacts, such as glare, and mismatched refractive index material were revealed.

In 2011, Duke large-field-of-view optical-CT scanner (DLOS) was introduced to reduce the scanning time to 15 minutes[32, 33]. The light source of DLOS is a 3W red LED behind a weak optical diffuser and a narrow band pass filter. The light is collected by the matched telecentric imaging lens. An aperture stop is used to reject the stray light. Algorithms to correct nonuniformity of CCD pixel response, spectral artifacts, residual stray-light artifacts were developed[34]. Point spread function (PSF) deconvolution was employed to correct the stray light originating in the lenses and components of the optical chain[35]. This correction is for internal scatter caused by internal reflections within the imaging lens. An analytical method for correcting the spectral artifacts was applied. To increase the dynamic range of the CCD array, the images are converted such that pixel values are proportional to exposure rate (the ratio of grey scale values to exposure time). For benchmarking, the mean 3D passing rate of gamma analysis using (3%, 3 mm, 5%

8

threshold) over the benchmark tests was 97.3%. Using 2 mm reconstructions, noise was at 2% in the 4-12 Gy dose range. However, the errors from the stray light, and dynamic range correction can be up to 3%.

During the past decades, optical CT scanners have been developed to achieve higher scanning speed, larger field of view (FOV), and lower dosimetry errors from the artifacts. However, for the optical CT scanner to be used in the clinic, higher signal-to-noise ratio, less labor-intensive operation procedures and less manual imaging processing are required. The prescribed dose per fraction of a conventional IMRT treatment is around 2 Gy but the statistical noise could be up to 5% at the dose level. There are multiple sources of artifacts in the optical CT scanner system and the magnitude of which is not clear in the publication36. Manual corrections of the images and alignment of the optical system may improve the reconstructed results but they are time-consuming and not optimal for clinical use. A robust and easy-to-use 3D dosimetry system with less sources of artifacts and increased signal to noise ratio is necessary for the clinical implementation of 3D dosimetry.

1.3 Current Challenges and Limitations of the Optical CT Scanner and 3D Dosimeters

The current challenges of the optical CT scanners for 3D dosimetry can be divided into two main categories, the measurement uncertainties and the limitations for clinical implementation[36, 38]. Scanner-related artifacts can come from the light scattering originating in the lenses and components of the optical chain, mismatch of the refraction index between the matching liquid and the 3D dosimeter, impurities on the tank wall or any surface in the optical chain, light non-uniformity, light output drift, impurities in the matching liquid, mismatch of the rotation center and the center of the projection images, reflected and refracted rays produced in the ray path and

the malfunction of the rotational and translational motors. Using FBP reconstruction technique, stationary impurities on the projection images and rough translational motor motion can cause significant ring artifacts. Reflection and refraction artifacts due to the mismatch of refractive index of the fluid, water tank wall, and the dosimeter can cause signal loss at the edge of the dosimeter and "cupping" artifact. Background subtraction has been employed to correct the ring artifacts and the reflection and refraction artifacts, but it requires the user to place the dosimeter at the same location of the scanner after irradiation. Geometric distortion from the mismatch of the rotation center and the center of the projection images and the light non-uniformity can be mitigated by image post-processing. Scattering from the optical system can cause non-uniformity of the acquired projection images. To reduce the scattering from the optical system, control of the amount of scattered light entering the camera is necessary. An aperture collimator mounted in the system can reduce the scattering, but it also reduces the signal. Post-imaging correction is needed to improve the residual scattering artifacts. Although current proposed methodologies have successfully improved the reconstructed image qualities, the corrected uncertainties can be up to 3%[32]. A new type of hardware system is necessary to reduce the sources of artifacts.

Dosimeter-related artifacts encompass various factors such as light scattering from radiation-induced optical contrast, dosimeter impurities, intra-dosimeter non-uniformity, and inter-dosimeter variation in sensitivity. If the dosimeter's sensitivity is inadequate or the delivered dose falls outside the optimal range, statistical noise may arise. Over the past decades, Radiochromic 3D dosimeters such as PRESAGE have been developed to exhibit optical contrast mainly through light absorption rather than light scattering, thus mitigating the scattering artifacts[36]. Previous publication has shown that the intensities of the scattered photons at more than 3 mm off-axis distances are less than 1% of the primary beam. However, for the dosimeter with high optical

density, the intensity of the scattered light could be more than 3%. The scattered photons decrease sharply with increasing off-axis distance[39]. Intra-dosimeter non-uniformity can be corrected through background subtraction techniques. However, inter-dosimeter variation cannot be corrected and may introduce uncertainties in dose calibration. A study investigated the intra-dosimeter consistency and inter-dosimeter relative dose reproducibility of the PRESAGE dosimeter to be with 2% uncertainty[40]. For PRESAGE, the absorbed dose is directly proportional to the optical density, and thus a linear regression curve can be used to calibrate to dosimeter. However, the slope of the calibration curve depends on the sensitivity of the dosimeters. Inter-dosimeter sensitivity difference could lead to absolute dose calibration uncertainty if the dosimeter used for calibration has different sensitivity than the dosimeter used for the measurement. For relative dose measurement, the intra-dosimeter sensitivity and optical density uniformity is important. The advantages of the PRESAGE dosimeter include its tissue equivalence, negligible dose rate and energy dependency.

The clinical use of the optical CT scanner is limited by several factors. These include labor-intensive and time-consuming operational procedures that are dependent on the user. The dynamic range of the CCD camera, scanning time, and the size of the scanning field-of-view are also limitations that need to be addressed for broader clinical application. In clinical practice, it is crucial to have simple operational procedures with minimal uncertainty and the potential for mistakes. Troubleshooting, such as optical system alignment or image correction, may need to be performed by clinical personnel. Robustness of the dosimetry system can facilitate the clinical implementation. The dynamic range of the projected images is limited by the detector. Stray light could reduce the dynamic range of the measurement, and thus reduce the contrast of the reconstructed images. Depending on the dose irradiated to the dosimeter and the optical path

length, the image intensities of the projected images could be saturated, leading to erroneous reconstructed dose distribution. For high dose measurement, such as SRS or SBRT treatment verification, sufficient dynamic range should be ensured. The broad-beam optical CT scanner has addressed the issue of prolonged scanning time but compared to the instant read-out of diode dosimetry systems, the scanning and reconstruction process can still be time-consuming, especially with multiple imaging correction methodologies. For clinical efficiency, not only the robustness of the hardware system but also the software system for scanner operation and image reconstruction are important. The FOV limitation is influenced by the size of the light source and detectors. In addition, due to the reflection and refraction artifacts from the mismatch of the refraction index between the matching liquid and the 3D dosimeter, the signal close to the edge of the dosimeter can be distorted[36].

1.4 Motivations for the Development and Clinical Use of a Parallel-Beam Optical CT Scanner with Fiber Optic Taper Collimation

3D dosimetry using 3D dosimeters and optical CT scanner for readout has potential to provide fast, high resolution, and accurate 3D dose distribution, thereby advancing modern radiation dosimetry. With the advance of machine, software engineering, and imaging technology, radiation treatments with modulated dose distribution with hypofractionated dose regime, have been commonly delivered to the patients. However, the radiation dosimetry in the clinics remain as point dose, or 2D measurements. In this study, a newly developed fiber optic CT scanner, under U.S. patent application entitled "Three-Dimensional Dosimetry Procedures, Methods and Devices, and Optical CT Scanner Apparatus Which Utilizes Fiber Optic Taper for Collimated Images", was commissioned and benchmarked[37]. The study aims to comprehensively investigate the sources and

12

magnitude of the measurement uncertainties from the developed OCT. The results can provide insights into the potential clinical utility and limitations of the developed 3D scanner.

IMRT QA has been widely performed in the clinic to verify the TPS dose calculation algorithm and the delivery system of a LINAC. Previous publications have discussed the sensitivity of IMRT QA in detecting errors and its clinical meaning. A multi-institutional study was performed to evaluate the current measurement-based QA using the Imaging and Radiation Oncology Core (IROC) head and neck phantom[41]. The results showed that traditional IMRT QA methods performed consistently poorly in searching for a larger or moderate error regardless of whether a 3%/3 mm or 2%/ 2 mm criteria was used. In 2018, AAPM task group 218 was published to address the issues of existing measurement-based IMRT QA methods[42]. It was concluded that purely using the passing rate for evaluation could underestimate the clinical consequences because the passing rate only summarized the gamma test in aggregate. In addition, if a QA methodology can provide measured DVH constraints, the QA results are more clinically meaningful. For point-dose or 2D dose measurement, it's difficult to identify the location of the dose measured in the patient's anatomy, and thus measured DVH constraints cannot be acquired. Using the developed OCT, combined with fiducial registration and structure-mapping, measured DVH can be obtained and compared with the calculated DVH on the TPS. The methodology is an important step toward comprehensive treatment fields evaluation.

Single-fraction stereotactic radiosurgery (SRS) is an efficacious irradiation strategy for a variety of intracranial metastases. SRS using LINAC and volumetric modulated arc therapy (VMAT) has become widely used within the Radiation Oncology clinics. The main advantage is its faster treatment delivery to multiple targets using a single isocenter (SIMT). Rapid dose falloff into the surrounding normal tissue and the conformality of the prescription dose can be achieved through

13

the dose modulation from MLC, gantry, and collimator rotation. A comprehensive evaluation of the LINAC performance is crucial, particularly given the 1-3 mm setup margin for SRS treatments. Currently, there is a lack of adequate tools for end-to-end testing of SIMT. End-to-end testing can increase the confidence in all layers of the procedure as well as reduce costs and time. In this study, the developed 3D dosimetry system was employed to perform a high-fidelity end-to-end 3D dosimetry with the capability of measuring the conformality index (CT), dose gradient index (DGI), DVH constraints, and rotational and translational errors.

Lastly, 3D small field dosimetry data was acquired in this study. The measurement of small field dosimetry is difficult due to dosimetric disequilibrium, partial source occlusion with the consequence of reduced output, and partial volume averaging effects. International atomic energy agency (IAEA) Report No. 483 provided a technical approach to deal with the issues in small field dosimetry[43]. However, there is no published guidelines for 3D small field dosimetry. In this study, the capability of an OCT-3D dosimetry system to measure 3D small dose distribution was investigated and the measurement results were thoroughly characterized and benchmarked against other detectors.

1.5 Summary and Organization of the Dissertation

To enhance the clinical applicability of the optical CT scanner for 3D dosimetry, it is crucial to design a novel system that minimizes measurement uncertainty and improves procedural efficiency. This study aims to address three key questions: 1) Can the developed 3D dosimetry system deliver reliable and precise dosimetry measurements? 2) Does the developed 3D dosimetry system offer sufficient convenience for clinical implementation? 3) Can the developed 3D dosimetry system yield significant clinical advantages and streamline the commissioning of advanced treatment modalities? By exploring these questions, we aim to evaluate the effectiveness

and potential of the developed 3D dosimetry system in a clinical setting. Chapter 2 describes commissioning, performance benchmarking, and investigations of a parallel-Beam optical CT scanner with fiber optic taper collimation. The experiments include hardware tests, imaging tests, and dosimetric commissioning. For the hardware test, data to verify the motor rotational motion, light source stability and parallel, and detector calibration were collected. Optical test targets were employed to evaluate the distortion, modulated transfer function (MTF), Signal to noise ratio (SNR), linearity, and uniformity of the projection images. Dosimetric commissioning were performed to evaluate the end-to-end results of the 3D dose measurements by irradiating regular fields and treatment fields to the 3D dosimeters. The measured results were compared with those measured by the radiochromic film and calculated by the TPS. The end-to-end measuredment uncertainties were evaluated. Chapter 3 presents the clinical application of the developed 3D dosimetry system to IMRT QA measurements. In the study, a robust methodology of 3D IMRT QA using fiducial registration and structure-mapping was proposed to acquire organ-specific dose information and measured dose volume histogram (DVH) constraints. Chapter 4 features research related to 3D end-to-end commissioning of a new radiosurgery platform. This study attempts to fill the gap in understanding of the overall mechanical and dosimetric uncertainties of the radiosurgery treatments for tolerances analysis and setup margin estimation as well as provides the further evidence supporting the importance of 3D end-to-end testing. The proposed system has potential application in commissioning of a new radiosurgery platform, remote multi-institutional audits of radiosurgery treatments and remote commissioning service for developing countries, where dosimetry equipment and human resources are not universally accessible. Chapter 5 presents the application of 3D dosimetry on small field dosimetry. The 3D dose distribution of small regular fields (< 1 cm) and treatment fields (< 2 cm) were measured and compared with the

radiochromic film measurements and TPS calculations. The study provides insights into the accuracy of small field measurements using the optical-CT 3D dosimetry system. Finally, Chapter 6 provides the summary and conclusion, and Chapter 7 identifies the future areas of investigation.

References or Bibliography

1.   Bentzen, S. M., Constine, L. S., Deasy, J. O., Eisbruch, A., Jackson, A., Marks, L. B., ... & Yorke, E. D. (2010). Quantitative Analyses of Normal Tissue Effects in the Clinic (QUANTEC): an introduction to the scientific issues. International Journal of Radiation Oncology* Biology* Physics, 76(3), S3-S9.

2.   Brahme, A. (1984). Dosimetric precision requirements in radiation therapy. Acta Radiologica: Oncology, 23(5), 379-391.

3.   Withers, H. R. (1975). The four R's of radiotherapy. In Advances in radiation biology (Vol. 5, pp. 241-271). Elsevier.

4.   Khan, F. M., & Gibbons, J. P. (2014). Khan's the physics of radiation therapy. Lippincott Williams & Wilkins.

5.   Fraass, B., Doppke, K., Hunt, M., Kutcher, G., Starkschall, G., Stern, R., & Van Dyke, J. (1998). American Association of Physicists in Medicine Radiation Therapy Committee Task Group 53: quality assurance for clinical radiotherapy treatment planning. Medical physics, 25(10), 1773-1829.

6.   Jacqmin, D. J., Bredfeldt, J. S., Frigo, S. P., & Smilowitz, J. B. (2017). Implementation of the validation testing in MPPG 5. a "Commissioning and QA of treatment planning dose calculations–megavoltage photon and electron beams". Journal of applied clinical medical physics, 18(1), 115-127.

7.   Klein, E. E., Hanley, J., Bayouth, J., Yin, F. F., Simon, W., Dresser, S., ... & Holmes, T. (2009). Task Group 142 report: Quality assurance of medical accelerators a. Medical physics, 36(9Part1), 4197-4212.

8.   Miften, M., Olch, A., Mihailidis, D., Moran, J., Pawlicki, T., Molineu, A., ... & Low, D. A. (2018). Tolerance limits and methodologies for IMRT measurement-based verification QA: recommendations of AAPM Task Group No. 218. Medical physics, 45(4), e53-e83.

9.   Ulmer, W., & Harder, D. (1996). Applications of a triple Gaussian pencil beam model for photon beam treatment planning. Zeitschrift für Medizinische Physik, 6(2), 68-74.

10.   Fogliata, A., Nicolini, G., Clivio, A., Vanetti, E., & Cozzi, L. (2011). Dosimetric evaluation of Acuros XB Advanced Dose Calculation algorithm in heterogeneous media. Radiation oncology, 6(1), 1-15.

11.   Han, T., Followill, D., Mikell, J., Repchak, R., Molineu, A., Howell, R., ... & Mourtada, F. (2013). Dosimetric impact of Acuros XB deterministic radiation transport algorithm for heterogeneous dose calculation in lung cancer. Medical physics, 40(5), 051710.

12.   Seniwal, B., Bhatt, C. P., & Fonseca, T. C. (2020). Comparison of dosimetric accuracy of acuros XB and analytical anisotropic algorithm against Monte Carlo technique. Biomedical Physics & Engineering Express, 6(1), 015035.

13.   Benedict, S. H., Yenice, K. M., Followill, D., Galvin, J. M., Hinson, W., Kavanagh, B., ... & Yin, F. F. (2010). Stereotactic body radiation therapy: the report of AAPM Task Group 101. Medical physics, 37(8), 4078-4101.

14.   Lutz, W., Winston, K. R., & Maleki, N. (1988). A system for stereotactic radiosurgery with a linear accelerator. International Journal of Radiation Oncology* Biology* Physics, 14(2), 373-381.

15.   Kron, T., Lehmann, J., & Greer, P. B. (2016). Dosimetry of ionising radiation in modern radiation oncology. Physics in Medicine & Biology, 61(14), R167.

16.   Darafsheh, A. (Ed.). (2021). Radiation Therapy Dosimetry: A Practical Handbook. CRC Press.

17.   Muir, B. R. (2015). Ion chamber absorbed dose calibration coefficients, ND, w, measured at ADCLs: distribution analysis and stability. Medical Physics, 42(4), 1546-1554.

18.   Almond, P. R., Biggs, P. J., Coursey, B. M., Hanson, W. F., Huq, M. S., Nath, R., & Rogers, D. W. (1999). AAPM's TG-51 protocol for clinical reference dosimetry of high-energy photon and electron beams. Medical physics, 26(9), 1847-1870.

19.   Niroomand-Rad, A., Chiu-Tsao, S. T., Grams, M. P., Lewis, D. F., Soares, C. G., Van Battum, L. J., ... & Chan, M. F. (2020). Report of AAPM task group 235 radiochromic film dosimetry: an update to TG-55. Medical physics, 47(12), 5986-6025.

20.   Kry, S. F., Alvarez, P., Cygler, J. E., DeWerd, L. A., Howell, R. M., Meeks, S., ... & Mihailidis, D. (2020). AAPM TG 191: Clinical use of luminescent dosimeters: TLDs and OSLDs. Medical physics, 47(2), e19-e51.

21.   Mijnheer, B., Beddar, S., Izewska, J., & Reft, C. (2013). In vivo dosimetry in external beam radiotherapy. Medical physics, 40(7), 070903.

22.   Herman, M. G., Balter, J. M., Jaffray, D. A., McGee, K. P., Munro, P., Shalev, S., ... & Wong, J. W. (2001). Clinical use of electronic portal imaging: report of AAPM Radiation Therapy Committee Task Group 58. Medical physics, 28(5), 712-737.

23.   Hintenlang, D. (2011). TH-C-301-03: Utilization of MOSFET Dosimeters for Clinical Measurements in Radiology. Medical Physics, 38(6Part35), 3861-3861.

24.   Gore, J. C., Ranade, M., Maryanski, M. J., & Schulz, R. J. (1996). Radiation dose distributions in three dimensions from tomographic optical density scanning of polymer gels: I. Development of an optical scanner. Physics in Medicine & Biology, 41(12), 2695.

25.   Xu, Y., Wuu, C. S., & Maryanski, M. J. (2004). Performance of a commercial optical CT scanner and polymer gel dosimeters for 3-D dose verification: optical CT scanning of polymer gel. Medical physics, 31(11), 3024-3033.

26.   Oldham, M., & Kim, L. (2004). Optical-CT gel-dosimetry II: Optical artifacts and geometrical distortion. Medical physics, 31(5), 1093-1104.

27.   Adamovics, J., & Maryanski, M. (2004, June). OCT scanning properties of PRESAGE-A 3D radiochromic solid polymer dosimeter. In Medical Physics (Vol. 31, No. 6, pp. 1906-1906). STE 1 NO 1, 2 HUNTINGTON QUADRANGLE, MELVILLE, NY 11747-4502 USA: AMER ASSOC PHYSICISTS MEDICINE AMER INST PHYSICS.

28.   Doran, S. J., Krstajic, N., Adamovics, J., & Jenneson, P. M. (2004). Optical CT scanning of PRESAGE™ polyurethane samples with a CCD-based readout system. In Journal of Physics: Conference Series (Vol. 3, No. 1, p. 240). IOP Publishing.

29.   Guo, P. Y., Adamovics, J. A., & Oldham, M. (2006). Characterization of a new radiochromic three-dimensional dosimeter. Medical physics, 33(5), 1338-1345.

30.   Olding, T., Holmes, O., & Schreiner, L. J. (2010). Cone beam optical computed tomography for gel dosimetry I: scanner characterization. Physics in Medicine & Biology, 55(10), 2819.

31.   Granton, P. V., Dekker, K. H., Battista, J. J., & Jordan, K. J. (2016). Stray light in cone beam optical computed tomography: I. Measurement and reduction strategies with planar diffuse source. Physics in Medicine & Biology, 61(7), 2893.

32.   Thomas, A., Newton, J., Adamovics, J., & Oldham, M. (2011). Commissioning and benchmarking a 3D dosimetry system for clinical use. Medical physics, 38(8), 4846-4857.

33.   Thomas, A., & Oldham, M. (2010, November). Fast, large field-of-view, telecentric optical-CT scanning system for 3D radiochromic dosimetry. In Journal of Physics: Conference Series (Vol. 250, No. 1, p. 012007). IOP Publishing.

34.   Thomas, A., Pierquet, M., Jordan, K., & Oldham, M. (2011). A method to correct for spectral artifacts in optical-CT dosimetry. Physics in Medicine & Biology, 56(11), 3403.

35. Thomas, A., Newton, J., & Oldham, M. (2011). A method to correct for stray light in telecentric optical-CT imaging of radiochromic dosimeters. Physics in Medicine & Biology, 56(14), 4433.

36. Oldham, M. (2006, December). 3D dosimetry by optical-CT scanning. In Journal of Physics: Conference Series (Vol. 56, No. 1, p. 58). IOP Publishing.

37. Patent Application Publication: Pub No: US 2022/0412877 A1
Three-Dimensional Dosimetry Procedures, Methods and Devices, and Optical CT Scanner Apparatus Which Utilizes Fiber Optic Taper for Collimated Images

38. De Deene, Y., & Jirasek, A. (2015, January). Uncertainty in 3D gel dosimetry. In Journal of Physics: Conference Series (Vol. 573, No. 1, p. 012008). IOP Publishing.

39. Xu, Y., Adamovics, J., Cheeseborough, J. C., Chao, K. S., & Wuu, C. S. (2010, November). Light scattering in optical CT scanning of Presage dosimeters. In Journal of Physics: Conference Series (Vol. 250, No. 1, p. 012063). IOP Publishing.

40. Sakhalkar, H. S., Adamovics, J., Ibbott, G., & Oldham, M. (2009). A comprehensive evaluation of the PRESAGE/optical-CT 3D dosimetry system. Medical Physics, 36(1), 71-82.

41. Kry, S. F., Glenn, M. C., Peterson, C. B., Branco, D., Mehrens, H., Steinmann, A., & Followill, D. S. (2019). Independent recalculation outperforms traditional measurement-based IMRT QA methods in detecting unacceptable plans. Medical physics, 46(8), 3700-3708.

42. Miften, M., Olch, A., Mihailidis, D., Moran, J., Pawlicki, T., Molineu, A., ... & Low, D. A. (2018). Tolerance limits and methodologies for IMRT measurement-based verification QA: recommendations of AAPM Task Group No. 218. Medical physics, 45(4), e53-e83.

43. Palmans, H., Andreo, P., Huq, M. S., Seuntjens, J., Christaki, K. E., & Meghzifene, A. (2018). Dosimetry of small static fields used in external photon beam radiotherapy: summary of TRS-483, the IAEA–AAPM international Code of Practice for reference and relative dose determination. Medical physics, 45(11), e1123-e1145.

Chapter 2

Commissioning, Benchmarking and Clinical Application of a Novel Fiber Optic CT Scanner for Precise 3D Radiation Dosimetry

2.1 Introduction

Over the past decades, optical CT scanner has been used as a readout tool for the 3D dosimeters[1-6]. The methodology can provide 3D dose distribution of the delivered dose to the dosimeters. An ideal 3D dosimeter should be firm in structure, tissue equivalent, independent of response to the dose rate and energy delivered, sensitive to the irradiation, and reproducible dose response[7]. The 3D dosimeters, PRESAGE (Heuris, Inc.) used in this study are composed primarily of the synthetic polymer polyurethane[8-10]. The production of polymeric matrix can be separated into two steps. First, reacting an equivalent of commercially available polyol with two equivalents of a di-isocyanate forms a pre-polymer. The second step involves mixing the leuco dye, a free radical initiator, a catalyst, with a commercially available polyol and previously formed pre-polymer. The resulting polymer hardens in 6-48 hours. After being irradiated, the leuco malachite green has a visible absorbance maximum at 633 nm. Radical initiator produces radicals during the irradiation, and thus increases the detectability of the color development. However, it was shown that the weight per cent of the halogen content added to the polyurethane can increase the effective atomic number. The PRESAGE formulations with lower halogen contents show more radiologically water equivalent properties.

The basic principle of the dosimeter readout with optical CT scanning is based on the Beer-Lambert Law[11], which describes the relationship between the attenuation of light through a substance and the properties of that substance. According to the Beer's Law, the light attenuation of a physical material is related to the attenuation coefficient of the attenuating species, optical path length, and the concentration of the attenuating species. Applying Beer's law to the radiation dosimetry, the attenuation coefficient is related to the 633 nm light absorption of the leuco dye in the irradiated PRESAGE phantom, and thus the dose delivered to the phantom. The transmittance,

T of the substance can be defined as the ratio of the transmitted intensity, I, over the incident intensity, I_0, of the 633 nm light and it's related to the absorbance, A, by the following definition:

$$T = \frac{I}{I_0} = 10^{-A} \qquad (1)$$

$$A = log_{10}\frac{I_0}{I} \qquad (2)$$

In radiation dosimetry, the absorbance, also known as optical density, can be related to the dose delivered to the dosimeter. Optical CT scanner consisting of a 633 nm light source and a camera detector can measure the incident intensity and transmitted intensity of the light through the 3D dosimeter[12]. The 3D dosimeter can be rotated by a rotation stage, and thus 2D projections of the optical density from different angles can be acquired. The reconstruction process to compute a 3D image set of the optical density from the 2D projections is similar to the computed tomography. Using filtered back projection (FBP) algorithm[13], the attenuation profile at each angle is back projected across the image plane for each slice. Figure 1 shows the step-by-step process of inverse radon transformation for filtered back projection. The input of the inverse radon transformation is a sinogram and the output is a slice of the reconstructed images. A sinogram is generated by sorting and storing the detected projection at each angle. The algorithm assumes parallel beam geometry and the center of the projection matching the center of the rotation stage. In reality, the parallelism of the light source and the coincidence of the two centers need to be verified, thus avoiding introducing uncertainties. The transform process involves two main steps, the image is back projected and unblurred with a two-dimensional ramp filter in the Fourier domain. A 3D image data set can be reconstructed once all the slice images are reconstructed.
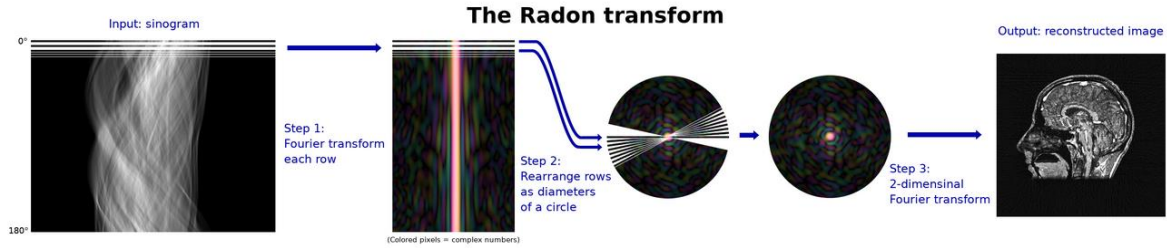
Figure 1. Illustration depicting the step-by-step process of the inverse Radon transformation for filtered back projection, utilized in 3D image reconstruction.

Limitations of filtered back projection algorithm include the artifacts from the scattering or refracted photons due to the assumption of straight light transmission, ring artifacts from the defected detector or impurities along the light path, photon starvation from the high dose pattern, structured noise from the different response of individual detector elements, statistical noise, and electronic noise when the number of photons reaching the detector is low[14]. The design of the optical CT scanner and its reconstruction program need to take these limitations into account and mitigate the uncertainties by carefully calibrating the system or applying corrections.

In the previous publication, PRESAGE, 3D dosimeters have been readout by two main types of optical CT scanner, OCTOPUS (MGS Research, Inc.)[15-19] and Duke large-field-of-view optical-CT scanner (DLOS)[20-24], for the investigations of clinical applications. OCTOPUS has the capability to produce clinically acceptable dose distribution with the least scattering photons but the raster scanning of a single dosimeter takes more than 10 hours, which is not optimal for clinical use. In addition, the alignment and adjustment of the optical system for optimal dosimeter scanning is labor-intensive. Duke DLOS was introduced to reduce the scanning time to 15 minutes. However, it requires analytical corrections for spectral artifacts, stray-light artifacts, reflection, and refraction distortions, and nonuniformity of CCD pixel response. The errors from the corrections can be up to 3%. Similar to OCTOPUS, the system requires labor-intensive alignment and adjustment of the optical lens. The factors limiting the optical CT scanner for clinical use

24

include its user-dependent, and time-consuming operational procedures. In clinical practice, reproducible results with minimal uncertainty and probability of mistake are important.

In this study, a newly designed optical CT scanner was commissioned and benchmarked. The primary innovation is the application of fiber optic taper[25, 26] to the optical CT system for image transfer and demagnification without distorting the image. Fiber optic taper can offer compact and lens-free solution for optical CT imaging. It doesn't require the user to adjust the focus and it can be directly coupled to sensors, which improves the light efficiency (>70% transmittance) and simplifies the operational procedures. The optical CT scanner using optical fiber taper can become more robust, lighter, and more compact compared with lens system. The fiber optic taper is manufactured by heating the central zone of a fiber optic block, and gently stretching the fiber as evenly as possible. Each optical fiber is comprised of a core with a higher refractive index surrounded by a cladding with a lower refractive index. According to the Smell's law, there is total internal reflection at the boundary of cladding if the light incident on the cladding with an angle larger than the critical angle, q_c. Figure 2 illustrates the correlation between the critical angle and the acceptance angle, q_{max} of an optical fiber. The light must fall within the acceptance angle in order to be guided into the fiber core. Additionally, optical fiber taper can block stray light from the surrounding. The scattered photons with large incidence angle can thus be removed by optical fiber[27, 28].
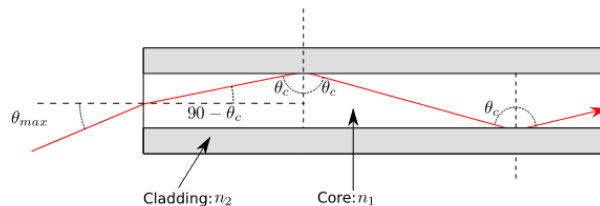
Figure 2. Diagram illustrating the relationship between the critical angle and the acceptance angle in an optical fiber.

$$\theta_c = sin^{-1}\left(\frac{n2}{n1}\right) \qquad\qquad (3)$$

$$\theta_{max} = sin^{-1}\left(\frac{n1}{1}\sin(90 - \theta_c)\right) \qquad\qquad (4)$$

The acceptance angle can be measured as numerical aperture (NA), which is related to the refractive index of the core, n_1 and the cladding, n_2[27, 28]:

$$NA = \sqrt{n_1{}^2 - n_2{}^2} \qquad\qquad (5)$$

A compact LED telecentric illuminator was also employed as the broad beam light source. It is up to 60% smaller than other telecentric illuminators and has the capability to provide a uniform parallel beam with a peak wavelength of 625 nm and 20 nm FWHM in continuous mode. The light source can be mounted on the optical system without the requirement of user-dependent alignment, which is an important feature for clinical applications.

In this study, a comprehensive performance benchmarking of the developed optical CT scanner was conducted. The benchmark tests can be categorized into three main groups: mechanical, imaging, and dosimetry. The mechanical tests encompass several assessments including the scanner motor test, parallel light test, stray light measurement, camera calibration, liquid scanning uniformity, determination of camera dynamic range, linearity of camera response to exposure time, light source stability, measurements of light spectrum change, and reproducibility of scanner measurements. These mechanical tests provide an overview of the scanner's functionality. Following the mechanical tests, imaging tests were performed using optical test targets to further explore the limitations of the captured images. The evaluation of imaging quality involved examining geometric distortion, modulation transfer function (MTF)[29], and signal-to-noise ratio (SNR) for each optical density level on the test target. Additionally, the linearity of the camera response to the optical density was assessed. The quality of the projection images directly affects the measured optical density and, consequently, the dose measurements. Lastly, dosimetry tests

were conducted using a 3D dosimeter PRESAGE. These tests included determining the SNR at each dose level, examining the linearity between the measured optical density and the delivered dose, measuring regular square fields and treatment fields, assessing measurement reproducibility, and comparing the dose with EBT3 radiochromic films[30, 31]. Furthermore, measurements were taken with and without background subtraction to understand the impact of stray light, reflection, refraction light, and the magnitude of corrected artifacts.

The purpose of this study is to provide a comprehensive evaluation of the measurement uncertainty of a novel parallel-beam optical CT scanner with fiber optic taper collimation and evaluate its clinical utility.

2.2 Materials and Methods

2.2.1 The design of a parallel-beam optical CT scanner with fiber optic taper collimation

The developed optical CT scanner consists of six components, an LED light illuminator, a water tank with a rotation stage and matching liquid inside, a window frame, a fiber optic taper, fiber optic wiondow, and a fiber-coupled CCD detector (Figure 3 and 4). A compact LED telecentric illuminator, LTCLHP CORE series (Opto Engineering, Houston, Tx) was employed for the light source. The telecentricity (<0.04 degree), uniformity (<1%), and working distance (33.6 cm $\pm$ 3%) of the light source were tested by the vendor. It can provide uniform and parallel red light (625 nm, 20 nm FWHM) without user-dependent alignment and modification. An aluminum stage was custom-made to hold the light source with fixed position and orientation. The orientation and position of the light source was aligned precisely with the position of the rotation stage and the camera to achieve optimal image acquisition. The vendor-defined light source is not in circular shape, and thus positioning each component to achieve optimal field-of-view is important. The current design has a field of view of 7.2 cm (height) $\times$ 11 cm (width). The aquarium contains two

acrylic windows along the beam path, while the remaining two walls, located outside of the beam path, are constructed from opaque materials. The opaque walls are designed to prevent stray light from the surrounding environment from interfering with the measurements or imaging process. An fiber optic taper with the taper ratio of 3:1 was mounted to the exit window with a window frame for light collection, transfer, and demagnification. The smaller end of the fiber optic taper is coupled to a fiber optic window, bonded to a CCD camera (Allied Vision, Houston, Tx) with dimensions of 110 mm (L) × 66 mm (W) × 66 mm (H) and resolution of 4008 (H) × 2672 (V). The fiber optic window can preserve the images and significantly increase the amount of light collected by the CCD camera. To avoid transmission losses, the CCD camera and fiber bundle are in close proximity since any gap between will lead to light emerging from the individual fiber at large angles.
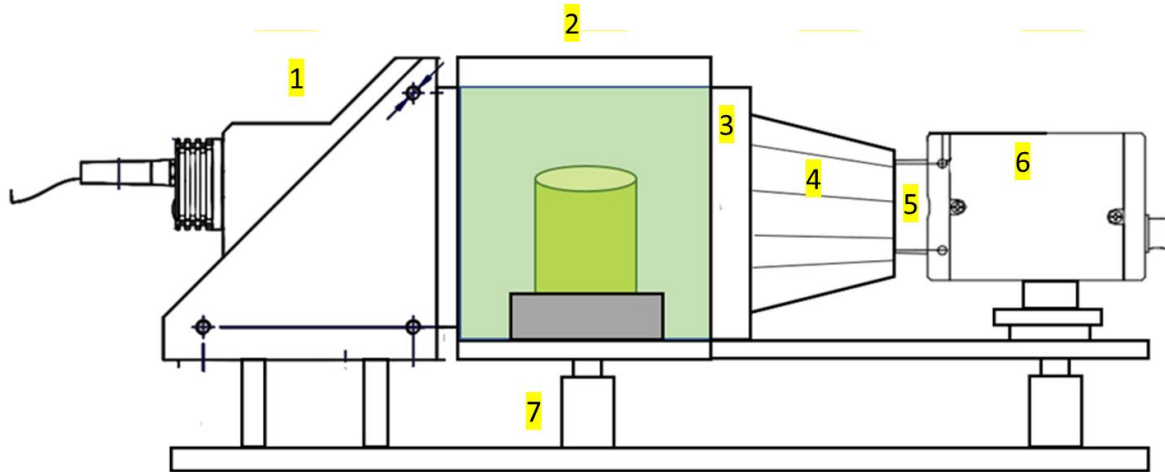
Figure 3. Schematic diagram of the developed optical CT scanner, showcasing the following components: (1) LED light illuminator, (2) aquarium filled with optical matching liquid, (3) window frame, (4) fiber optic taper, (5) fiber optic window, and (6) CCD camera.
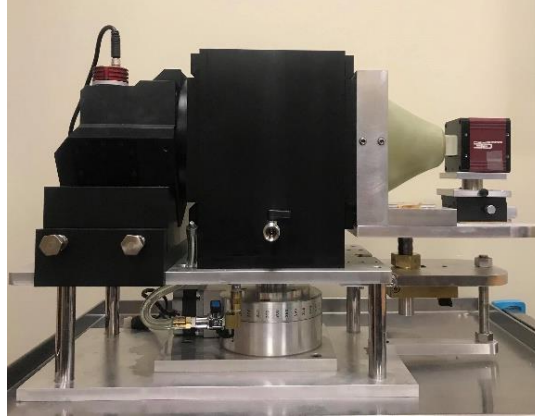
Figure 4. Photograph of the developed optical CT scanner.

Two software programs were developed for image acquisition and image reconstruction. An in-house LabVIEW (National Instruments Corp, Austin, Tx) program was developed to control the stage rotation and image acquisition automatically (Figure 5). In this program, the user can determine the degree of rotation, rotation speed, rotation direction, and time delay before image acquisition. In addition, the scanned dosimeter is displayed in real time for the user to monitor the scanning process. The program automatically saved 16-bit images with the resolution of 9 μm in TIFF format. For a dosimeter scan with 360 degrees and 1 degree per step, 360 images were saved to the file location. 3D image reconstruction was performed utilizing an in-house Matlab program. Due to the parallelism of the LED light source, inverse radon transform function can be employed to reconstruct images. The detected 2D projections can be thought of as a set of line projections. A sinogram, produced by combining the line projection at each angle, is the input of the inverse transform function to reconstruct a slice of tomographic images. A set of 3D dose images can be produced from multiple sinograms. During the reconstruction, local regression using weighted linear least squares and a second-degree polynomial model was applied to remove the noisy pixels. For the filtered-back projection, Ram-Lak filter multiplied by a sinc function was used to de-

emphasize high frequency signals and shape-preserving piecewise cubic interpolation was used for the interpolation during back projection.
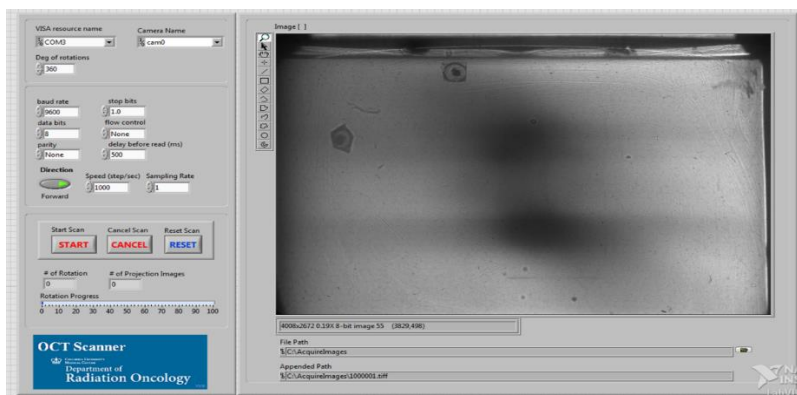
Figure 5. User interface of the developed optical CT scanning software. The left side of the interface presents the scanning parameters and control buttons, while the right side displays real-time projection images of the scanned dosimeter.

2.2.2 Operational procedures for dosimeter scanning

Prior to conducting the optical CT scanning, the exposure time was carefully adjusted to ensure that the measured image intensities fall within the dynamic range of the CCD camera. This adjustment is directly linked to both the dose delivered to the dosimeter and the length of the irradiated region along the beam path. When a larger dose is delivered and the path length increases, it may result in smaller image intensities being measured. By increasing the exposure time, it becomes possible to capture a signal that is adequate for precise dose measurement while ensuring that the acquired data remains within the dynamic range of the camera. This adjustment helps prevent overexposure or underexposure of the images, enabling accurate and reliable dose measurements during the optical CT scanning process. Once the exposure time is determined, before irradiating a dosimeter, the blank dosimeter was scanned by the optical CT scanner for background subtraction. There's no warmup time for the developed optical scanner. The background subtraction was performed for each measurement to reduce the structural artifacts, such as ring artifacts from the impurities on the window surface, optic fiber surface, source surface,

30

or the presage dosimeter, reflection and refraction artifacts, stray light. The magnitude of the artifact reduction was evaluated in the dosimetry tests. The dosimeter was then positioned at the treatment room for dose irradiation. Figure 6 shows a picture of an irradiated dosimeter. After irradiation, the irradiated dosimeter was put at the same orientation and position in the rotation stage as the background scanning. The rotation stage has four notches to make sure the reproducibility of the phantom positioning before and after the irradiation. The reproducibility was evaluated in the dosimetry tests. The scanner parameters of the irradiated dosimeter scan should be the same as the blank dosimeter scan to make sure the magnitude of the artifacts is consistent in the two scans for subtraction. Background subtraction can improve the accuracy of dose measurements, but erroneous results can be acquired if the two scans don't match, and thus the scanner's capability for reproducible scan is important for 3D dosimetry. To simplify the workflow, a background scan could be used for multiple measurements if the dimensions and image intensities of each 3D dosimeter is consistent, although the artifacts from impurities in each dosimeter cannot be corrected this way. After acquiring the two data sets, the images were transferred to the Matlab program for image reconstruction. The acquired images can be resized to make sure optimal image resolution and signal to noise ratio can be achieved. In this study, a resolution of 1 mm was selected to match the highest resolution of the treatment planning system, Eclipse (Varian, Palo Alto, CA). Before image reconstruction, the measured image intensities were transformed to optical density based on equation (2). Due to the linear response of the 3D dosimeter to the dose, the reconstructed optical density is proportional to the dose delivered. A relative 3D dose matrix can be acquired. In the same program, beam profiles and isodose lines can be plotted for dose analysis. SlicerRT, an extension of 3D Slicer was utilized for 2D, 3D gamma comparison, 3D dose cloud visualization.
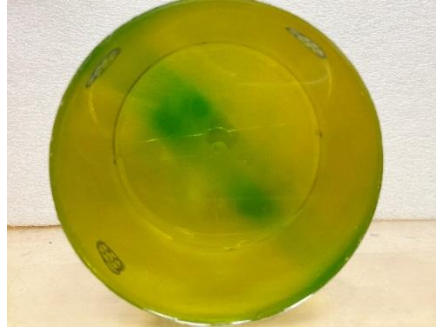
Figure 6. Photograph of an irradiated 3D dosimeter. The darkened region indicates the location where the radiation dose is deposited.

2.2.3 Mechanical tests of the optical CT scanner

Table 1 presents a comprehensive list of the benchmark tests conducted in this study, categorized into mechanical, imaging, and dosimetry tests. In the mechanical tests, the rotational accuracy of the motor was examined. To assess this, the motor was set to rotate 1 degree per step for a full 360 degrees. The 361st scanned image was then compared to the 1st scanned image to determine if they matched. A fiducial marker was placed on the dosimeter during scanning, and the two images were overlaid to evaluate any positioning differences of the fiducial. A line profile was generated to assess the accuracy of motor rotation. In addition to the motor test, the parallelism of the LED light was evaluated. This involved placing a ruler at seven different locations along the beam path. If the light was parallel, the length of the 1 cm interval at each of the seven locations should be consistent. Thomas *et al.*[36] have measured the stray light detected by the camera of Duke DLOS scanner by placing an opaque light block in the beam path. In their study, the signal behind the light block should have approached dark field values but was significantly higher. It is worth noting that most of the stray light generated in the scanner originates within the imaging lens. However, in the developed lens-free fiber optic CT scanner, this stray light is expected to be negligible. To further understand the magnitude of stray light contamination, a similar test was performed in this

study. An opaque light block was placed in the beam path, immersed in a matching liquid. A line profile of the signal behind the light block was then plotted to assess the stray light levels.

For CCD camera calibration[32, 33], dark field (DI) and flat field (FI) were acquired. The dark field was taken without any light, and thus the signal collected is from the 'dark current'. Dark current was produced in the pixel element due to the thermal excitation of electrons into the conduction band, and thus the collection in the CCD wells. Although the dark current is directly proportional to the exposure time, the exposure times used in this study are short, and thus the change may be negligible. The change of dark field according to the exposure time was investigated. Although dark fields are reproducible, there is statistical noise in the dark current that can influence a weak signal. A flat field was acquired using the LED illuminator without the aquarium and fiber optic taper in between. The flat field images provide information of pixel-dependent quantum efficiency. Using these two images, a calibrated image (CI) can be obtained from the raw image (RI):

$$CI = \frac{RI - DI}{FI - DI} \qquad (6)$$

The measured optical density (OD) can be obtained from the calibrated image (CI) and the calibrated background image CI_0:

$$OD = log_{10}\frac{CI_0}{CI} = log_{10}CI_0 - log_{10}CI \qquad (7)$$

$$= log_{10}(RI - DI) - log_{10}(FI - DI)$$

$$-(log_{10}(RI_0 - DI) - log_{10}(FI_0 - DI))$$

$$= log_{10}(RI - DI) - log_{10}(RI_0 - DI)$$

The process of flat field calibration is incorporated into the background subtraction technique. To obtain a calibrated image, three key components are required: a raw signal image, a raw background image, and a dark field image. The dark field and flat field corrections are applied to correct the nonuniformity of light source and pixel-dependent detection efficiency of CCD camera.

To investigate the impact of dark field and flat field correction, a liquid scan was conducted to assess the non-uniformity of both the raw and calibrated images. The operational procedure included adjusting the exposure time prior to the measurement to ensure that the measured image intensities fell within the dynamic range of the CCD camera. For high dose measurements where lower image intensities are expected, longer exposure times were set to ensure that the pixel values remained higher than the dark fields. However, it's important to note that increasing the exposure time runs the risk of saturating the background intensities. Therefore, in this study, the optimal dynamic range of the CCD camera was determined to strike a balance. To verify the camera's linear response to exposure time, pixel values were measured using six different exposure times.

To have accurate dosimetric data, the light source stability over the measurement time is important. Using the current design, the measurement time is within 15 minutes. 360 liquid scans were acquired in 15 minutes and the pixel values over time were plotted. In addition, the mean value and standard deviation of the measured image intensities in a region of interests (ROI) in the projection images over ten scans were plotted to evaluate the scanner reproducibility.

The spectrum of the light source was measured by a spectrometer placed before and after the optical CT scanner, and after the optical CT scanner with a dosimeter in the tank. The three measurements can provide us an overview of the spectrum change due to the optical system and the 3D dosimeter.

Table 1. Benchmark tests performed in this study, including mechanical, imaging and dosimetry evaluations.

Item	Description
OCT Mechanical Tests	
Scanner Motor Test	Motor should rotate 1 degree/step, 360 degrees/full scan.
Parallel Light Test	The LED light source should emit parallel light

Stray Light Collimation	Measure the stray light collimation by the optic fiber taper
Camera Calibration	Dark field and flat field image acquisition. Camera calibration based on the acquired images.
Dynamic Range	Determine the dynamic range of the CCD acquisition
Exposure Time	Examine the linear relationship between the exposure time and the measured signal. Examine the dark field constancy over exposure time
Light Source Stability	Examine the stability of the LED light source over time
Light Spectrum	Measure light spectrum change in the optical system
Scanner Reproducibility	Reproducibility of the scanned image intensity
Uniformity	Determine the uniformity and standard deviation of the liquid and blank phantom images
OCT Imaging Tests	
Geometric Distortion	Image distortion measurements using distortion test target
MTF	Modulation transfer function (MTF) measurement using high quality test target
SNR	Evaluate the signal to noise ratio (SNR) of each optical density level
Optical Density Linearity	Evaluate the linearity of the measured optical density to the phantom-defined optical density
OCT 3D Dosimetry Tests	
SNR	Evaluate the signal to noise ratio (SNR) of each dose level
Dose Linearity	Evaluate the linearity of the measured optical density to the delivered dose
Regular Field Measurements	Evaluate the dosimetric accuracy of regular field measurements
Treatment Field Measurements	Evaluate the dosimetric accuracy of treatment field measurements
Measurement Reproducibility	Evaluate the reproducibility of the treatment field measurements
EB3 Film Comparison	Compare the treatment field measurements with the EBT3 film dosimetry
Background Subtraction	Evaluate the measurement uncertainty before and after the background subtraction

2.2.4 Imaging tests of the optical CT scanner

Image distortion can lead to misplaced signals in the image, and thus become troublesome for accurate dose distribution. Theoretically, our lens-free optical system using optical fiber taper can preserve the image shape, but the fiber bundles may influence the acquired image if it's not manufactured well. One of the imaging tests is to evaluate the geometric distortion by placing a

Glass distortion target (Edmund Optics Inc., Barrington, NJ) in the water tank, immersed in the

matching liquid (Figure 7). The accuracy of dot-to-dot distance is within 0.002 mm and the flatness

of the test target is within 0.0254 mm. The magnitude of the geometric distortion can be calculated

using the following equation:

$$Distortion \% = \frac{MD-AD}{AD} * 100 \qquad (8)$$

Where MD is the measured distance, AD is the actual distance on the phantom.

To evaluate the resolution of the imaging system, modulated transfer function (MTF) was

measured using transmitted, sinusoidal test target (Edmund Optics Inc., Barrington, NJ), shown in

Figure 8. The test target was placed in the water tank, immersed in the matching liquid. The test

frequency ranges from 0.375 lp/mm to 80 lp/mm. The measured image resolution is the maximal

resolution of the optical system. For the dosimetry purpose, the tradeoff between the SNR and

resolution was made to reduce the statistical uncertainty. The target also provides patterns of

different optical densities ranging from 0.2 to 1.2. Using the same sinusoidal test target, the

linearity of the measured optical density to the phantom-defined optical density was evaluated. An

ROI was plotted on each optical density material to evaluate the signal to noise ratio. Theoretically,

the statistical noise across the image detector is the same. Higher optical density materials produce

larger signal and higher signal to noise ratio.
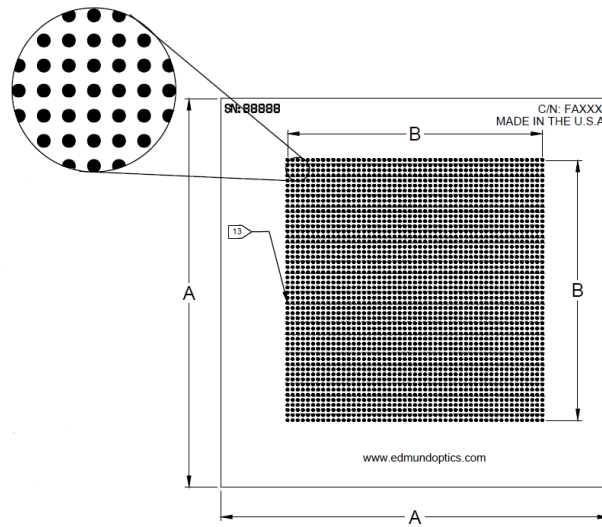
Figure 7. Glass optical test phantom utilized for assessing geometric distortion.
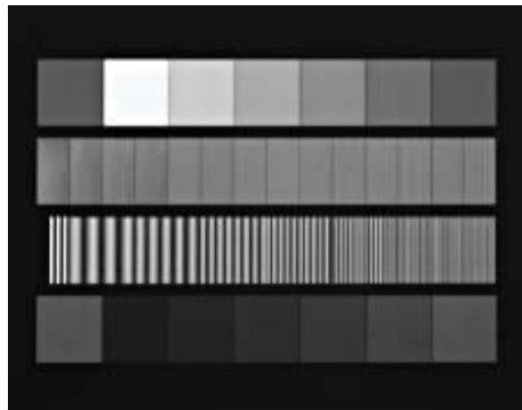
Figure 8. Transmitted sinusoidal test target employed for measuring the modulated transfer function and assessing the resolution of the imaging system.

2.2.5 Dosimetry tests of the optical CT scanner

After the fundamental analysis of the optical system, the overall measurement uncertainty can be tested by measuring the irradiated dosimeters with different test patterns following the operational procedures. First, four 6 MV photon beams with field size of 2×2 cm^2 were delivered to a single 3D dosimeter using linear accelerator, TrueBeam (Varian, Palo Alto, CA). The MU number of

each beam was calculated so that eight different dose levels, 386, 500, 772, 1000, 1389, 1800, 1930, 2500 cGy can be measured. The linear relationship between the dose delivered and measure optical density in the reconstructed images were plotted. To evaluate the linearity, mean absolute percentage error (MAPE), also called the mean absolute percentage deviation (MAPD) was employed[34]:

$$M = \frac{1}{n}\sum_{t=1}^{n}\frac{(A_t - F_t)}{A_t} \qquad (9)$$

n is the number of the fitting point, A_t is the actual value, and F_t is the forecast value. The linearity error is directly related to the dose measurements. It is noteworthy that each 3D dosimeter may have different response to the radiation, and thus the slope of the linear curve may change. Currently, relative dosimetry can be obtained by applying the linear relationship. In the future, if the response of each dosimeter is consistent, the dose response curve of a certain dosimeter can be applied to other dosimeters, and thus absolute dosimetry can be achieved. Besides linearity, SNR at each dose level can be measured using the same acquired scan. A ROI was drawn at each dose level to acquire the mean and relative standard deviation of the measurement. The measured relative standard deviation corresponds to the overall measurement uncertainty without the consideration of structural artifacts.

To verify the background subtraction and evaluate its effect on the measured dose distribution, a blank dosimeter was placed in the tank for background scanning three times. The three images were subtracted from each other to evaluate the residual measurement uncertainties. Theoretically, structural artifacts, such as ring artifacts, reflection and refraction artifacts, stray light artifacts, and impurities in the dosimeter can be subtracted.

A regular 2×2 cm^2 was delivered to the dosimeter to evaluate the dose measurement accuracy. 2D isodose lines from the measurement and calculation were overlayed for evaluation. Gamma

index analysis using 2%/2mm criteria were employed to compare the measured dose distribution with the calculated dose distribution from Eclipse treatment planning system with and without the background subtraction. The distance to agreement (DTA), defined as the distance from a pixel in the reference distribution to the nearest pixel in the evaluated distribution with the same dose, was introduced to better evaluate high gradient dose distribution. This is because a shift in the high dose gradient area can produce significant errors. In low gradient region, absolute dose differences can be used for evaluation. Gamma value was proposed by Dr. Low to combine the DTA with the absolute dose difference using the below equation[35]:

$$Gamma = \sqrt{\left(\frac{d}{d_0}\right)^2 + (\frac{r}{r_0})^2} \qquad (10)$$

Where, d is the point dose difference between measured image and the calculated image, d_0 is the dose criteria, r is the distance between the measured point and the calculated point, r_0 is the distance criteria. The gamma passing rate refers to how many percentages of the points having the gamma value smaller than 1.

To evaluate the treatment field measurements, a stereotactic body radiotherapy treatment (SBRT) plan with a prescription dose of 7 Gy was delivered to a 3D dosimeter. The measured dose distribution in sagittal, coronal, and transverse plane were compared with the calculated dose distribution using isodoseline comparison. In addition, gamma test using 3%/2 mm criteria was employed to evaluate the dose difference. To analyze the impact of background subtraction, 2D dose distribution and line profiles comparison before and after the background subtraction were plotted. To have a comprehensive view of the treatment field measurements, an intensity modulated radiotherapy treatment plan with a lower prescription dose, 3 Gy, was delivered to a 3D dosimeter with higher sensitivity. 2D isodose line comparison and gamma tests were

39

performed. These measurements can provide insights into the clinical utility of the proposed 3D dosimetry system.

In order to further evaluate the dosimetry accuracy of the optical CT scanner, a comparison was made between the dose distributions measured by the scanner and those obtained using EBT3 radiochromic film. EBT3 radiochromic films are recognized for their ability to measure accurate relative dose distributions with high resolution. Two types of comparisons were conducted: AP dose measurement and IMRT dose measurement. In the case of AP dose comparison, it is possible for the geometry of the solid water used for the film measurement to differ from the geometry of the 3D dosimeter. However, for IMRT measurement comparison, the beams can come from different angles. To ensure the same geometry for comparison purposes, the 3D dosimeter was divided in half, and a piece of radiochromic film was placed in between. Both comparisons involved the use of isodose lines and gamma tests.

To assess the reproducibility of the treatment field measurement, an irradiated dosimeter was scanned three times. Between each measurement, the dosimeter was removed from and reinserted into the water tank to simulate the uncertainties that can occur during actual scanning procedures. The isodose lines obtained from the three scans were overlaid and compared to evaluate any differences or variations. Additionally, a gamma test and histogram of the dose differences were plotted to examine the level of uncertainty present in the measurements. The magnitude of the measured uncertainty provides an overview of the statistical errors associated with the measurement. The reproducibility of a dosimetry measurement is an important characteristic because it indicates the system's ability to minimize random errors. By focusing on reducing random errors, systematic errors can be more effectively corrected. Therefore, evaluating the

reproducibility of the measurement helps determine the reliability and consistency of the dosimetry data generated by the system.

2.3 Results

2.3.1 Mechanical tests

2.3.1.1 Scanner Motor Test

The scanner rotation stage underwent testing to ensure a full 360-degree rotation in each scan. For visualizing the rotation status, a fiducial marker was placed on a dosimeter. By comparing the first projection image with the 361st projection image, the shift of the fiducial marker and, consequently, the rotation shift could be examined. Figure 9 displays the images of the fiducial marker in the two projection scans, along with the line profiles taken across the fiducials. The line profiles demonstrate that the two fiducials correspond to each other within the highest resolution of the camera, which is 0.027 mm. This analysis confirms the accuracy of the scanner rotation stage, as there is no significant shift or misalignment observed in the fiducial marker between the first and 361st projection images.

(a)
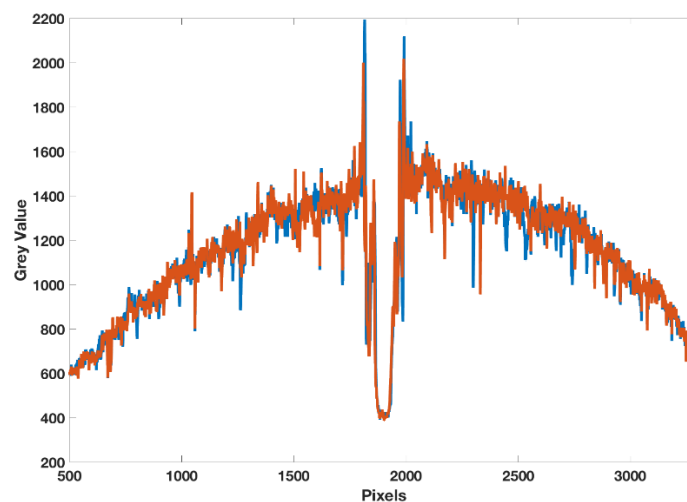
(b)
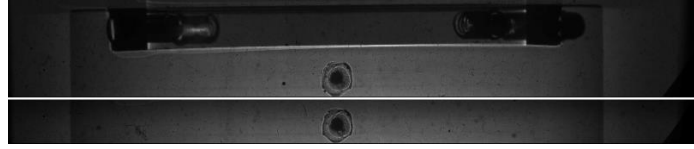
Figure 9. Results of motor rotation accuracy. (a) Line profiles across the fiducials at 0 and 360 degrees of rotation of the motor. (b) Images of the fiducials in the two projection scans at 0 and 360 degrees of rotation of the motor.

2.3.1.2 Parallel light test

The vendor has reported the telecentricity of the light source to be less than 0.04 degree. To ensure the optical system has constant magnification regardless of the object's distance or location in the field of view, a ruler was placed in the water tank at seven different distances from the light source across the water tank. The measured length of '1 cm' interval was recorded at each position. In Figure 10, no trend of magnification was observed. The maximum deviation of the length measured is within 0.01 mm. The parallelism of the light source is essential to the dose reconstruction since the inverse radon transform used for the filtered-back projection assumes the light is parallel, and any unparallel light can be misplaced by the reconstruction code.

(a)

(b)
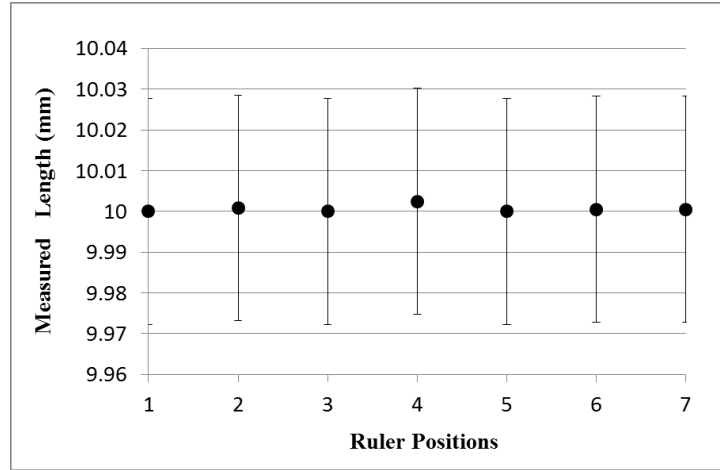
Figure 10. Evaluation of light parallelism. (a) A projection image of the ruler placed in the tank. (b) Measured ruler length at seven different locations across the water tank.

2.3.1.3 LED light spectrum

Figure 11 presents the measured spectra of the pure light source, the light after passing through the optical scanner, and the light after passing through both the dosimeter and the optical scanner. All three spectra exhibit a peak at the wavelength of 626.8 nm. The pure light source spectrum has the narrowest full width at half maximum (FWHM) value, measuring 12.8 nm. However, after passing through the optical CT scanner, the FWHM increases to 14.3 nm due to light scattering within the system. Furthermore, when the light traverses the dosimeter and the optical CT scanner, the FWHM further increases to 16.6 nm as a result of more light absorption at the peak wavelength. Based on these findings, the influence of the spectrum change on the dosimetry measurement can be considered negligible. Although there are slight variations in the FWHM values due to light scattering and dosimeter absorption, the fact that all three spectra peak at the same wavelength suggests that the dosimetry measurement can still be reliably performed without significant impact from the spectrum change.
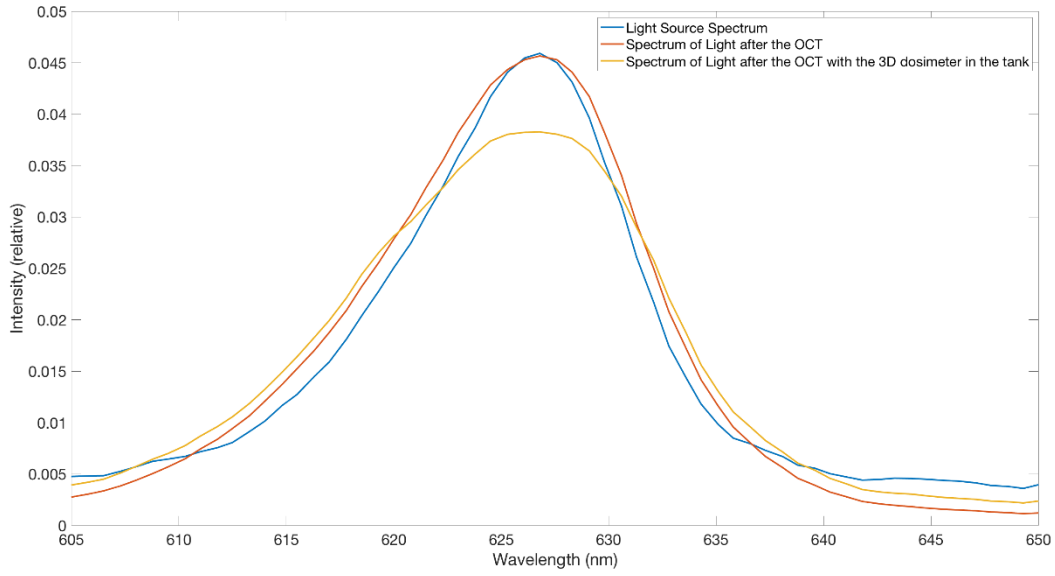
Figure 11. Plots of the measured spectrum for different stages of light propagation. (a) Spectrum of the pure light source. (b) Spectrum of the light after passing through the optical scanner. (c) Spectrum of the light after passing through the dosimeter and optical scanner.

2.3.1.4 Stray light measurement

Figure 12 displays a line profile taken across the light block, providing insight into the measured image intensities behind the block. The analysis reveals that the mean intensity is 31, with a standard deviation of 1.875. These values correspond to the dark current of the system. Moving towards the edge of the light block, the intensity increases to 59, which can be attributed to scattering effects. However, the impact of this increased intensity on the measurement is deemed negligible. This measurement demonstrates that the stray light contamination can be effectively mitigated by the use of a fiber optic taper. By employing the taper, the stray light is reduced, resulting in a more accurate and reliable measurement of the desired signal.

(a)
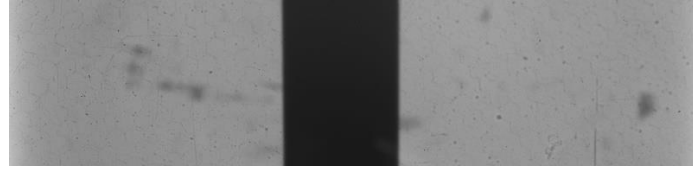
(b)
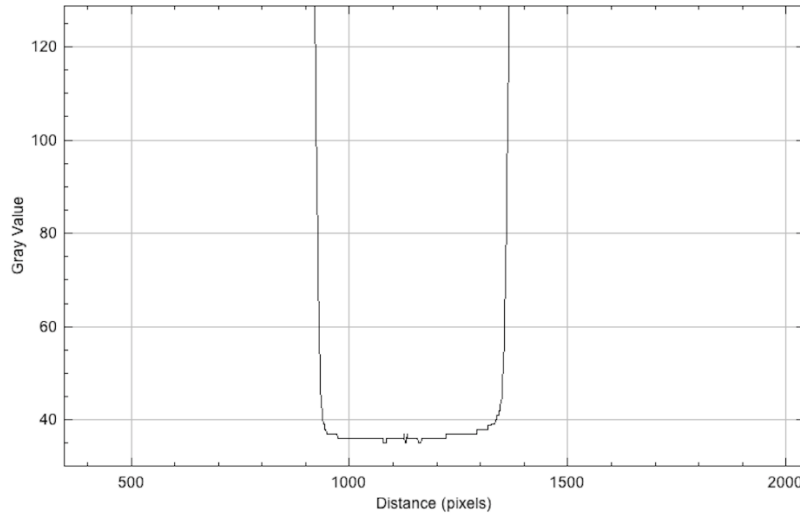
Figure 12. Evaluation of stray light contamination. (a) Projection image showing the presence of a light block placed in the beam path. (b) Line profile plot across the light block, illustrating the extent of stray light contamination.

2.3.1.5 Scanner Reproducibility

To assess the reproducibility of the scanned image intensities, ten projection images were acquired with liquid in the water tank. In order to evaluate the consistency of the pixel values, a region of interest (ROI) was selected within each image. Figure 13 illustrates the ROI placement and the resulting measurements of the mean and standard deviation of the pixel values. The analysis reveals that the mean values obtained from the ten scans exhibit a high level of agreement, with

variations within 0.05%. This indicates a strong level of reproducibility in the measured image
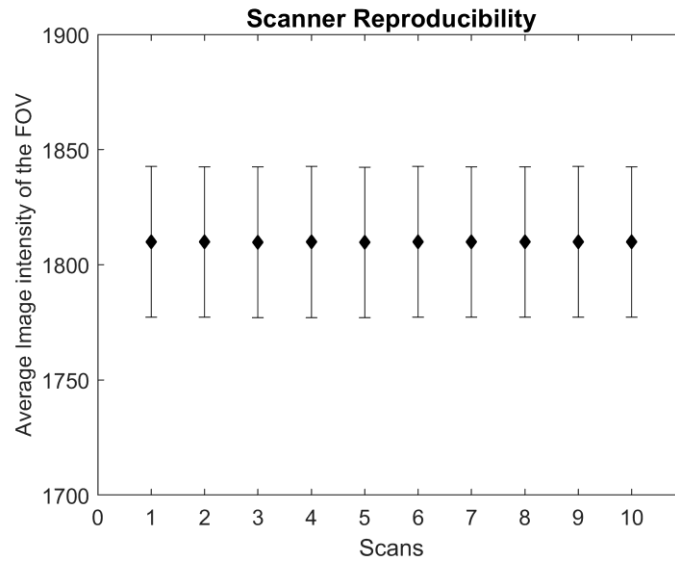
intensities.

Figure 13. Plot showing the measured average image intensity in 10 repeated projection scans. The error bars represent the standard deviation of the measurements.

2.3.1.6 Light source stability

To assess the variation in light intensity over an extended period of time, a liquid scan was

conducted with a total scanning duration of 16 minutes. During this scan, the pixel value at a

specific point within each projection image was recorded. Figure 14 showcases the results of this

evaluation, indicating the recorded pixel values over the course of the scan. The maximum

recorded value was 3133.52, while the minimum recorded value was 3126.29. The difference between these two values amounts to only 0.23%. This analysis demonstrates that the light intensity remains relatively stable and consistent throughout the 16-minute scanning period.

2.3.1.7 Exposure time linearity

The linearity of the measured signal to the exposure time was evaluated by measuring the liquid scan using six different exposure times. The mean value of an ROI was recorded for each scan (Figure 15). The MAPE of the linear fitting is 0.72%. Linearity of the exposure time is important when different exposure times are used. If it's linear, the same optical density value can be acquired even with different exposure time.
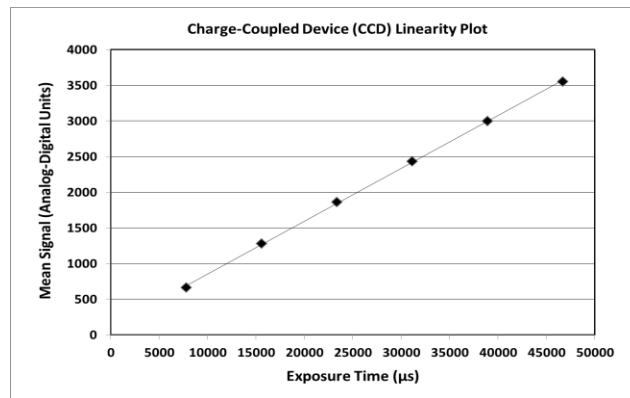
Figure 15. Plot demonstrating the linearity of the measured signal to the exposure time. The x-axis represents the exposure time, while the y-axis represents the measured signal intensity.

Besides the linearity of the signal to the exposure time, the change of dark current to the exposure time was measured. Figure 16 shows the histogram of the image intensities in three dark field images using three different exposure time. The mean and standard deviation of the pixel values

using 0.0415 s, 0.0831 s, and 0.1662 s exposure time are 47.8 (±3.632), 48 (±3.691), and 50 (±4.053). Although the dark current can increase with the exposure time, the exposure time used in this study is no longer than 0.16 s, and thus the change is minimal. It is noteworthy that the standard deviation of the dark image can lead to measurement uncertainty when the measured signal has low pixel values, which happens when high irradiation dose is delivered to the dosimeter. To have measured uncertainty from the dark image noise lower than 1 %, the measured signal should have pixel value larger than 400. In addition, if the measured intensity is higher than 4095, the highest measured pixel value of the CCD camera, the signal will be saturated. The optimal dynamic range of this optical system is between 400 to 4000. Adjusting the exposure time can change the measured image intensities to be within the dynamic range.
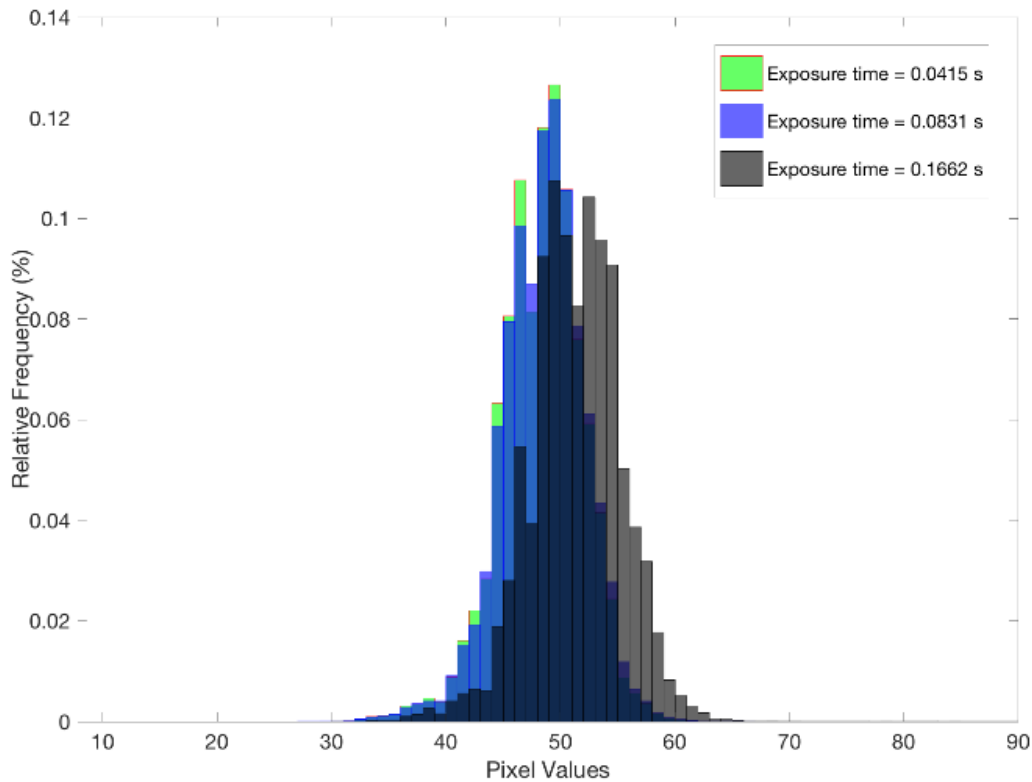
Figure 16. Measured histograms of image intensities in three dark fields with different exposure times. The histograms correspond to exposure times of 0.0415 s, 0.0831 s, and

0.1662 s, respectively. The x-axis represents the image intensity, and the y-axis represents the relative frequency.

2.3.1.8 Camera calibration

As mentioned in section 2.2.3, the variation of photon sensitivity at each pixel can be corrected by applying the flat field image using equation 6. Figure 17 shows image intensities of each pixel using different exposure times before and after the camera calibration. Each line represents a pixel. Due to different quantum efficiency, each pixel has a different slop of the linear curve. After camera calibration, the linearity curves converge into one curve.
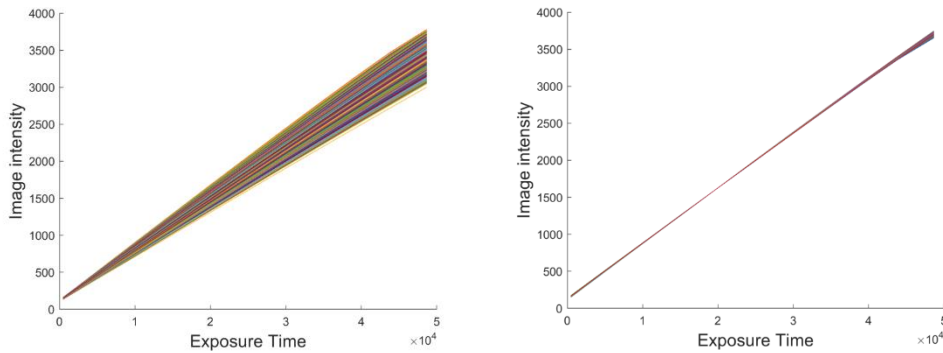
Figure 17. Image intensities of each pixel with different exposure times before (left) and after (right) camera calibration. Each line represents the measurement of an individual pixel.

The effect of camera calibration on liquid scan uniformity can be seen in Figure 18. Figure 18 shows the horizonal and vertical profiles of the liquid scan before and after camera calibration. Before camera calibration the relative standard deviation in 80%, and 100% field of view of the camera are 1.8% and 3.5%. After the camera calibration, the relative standard deviation in 80%, and 100% field of view of the camera are 0.29% and 0.3%.
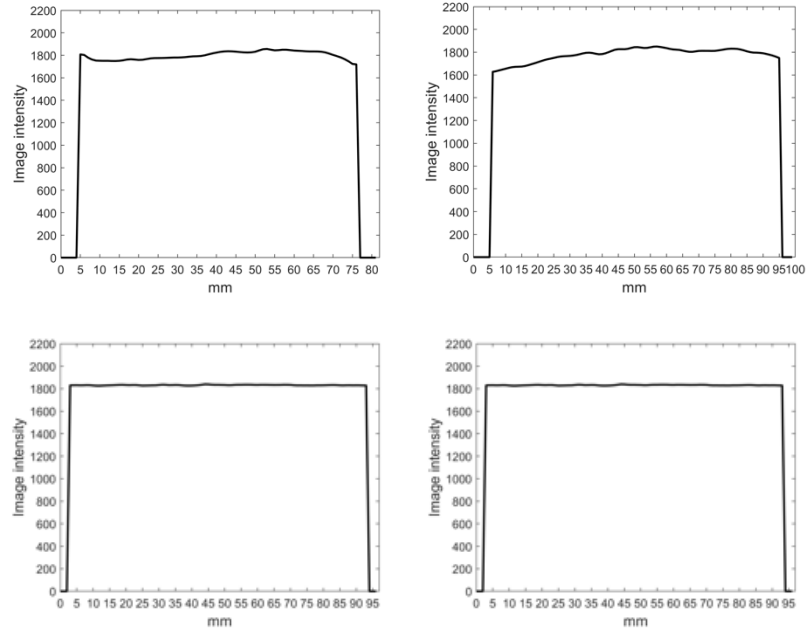
Figure 18. Line profiles of the liquid scan before (Top) and after (Bottom) camera calibration. The left subplots illustrate the horizontal line profiles, while the right subplots depict the vertical line profiles. The top row displays the line profiles before camera calibration, and the bottom row shows the line profiles after camera calibration.

2.3.2 Imaging tests

2.3.2.1 Geometric distortion

The magnitude of the geometric distortion can be calculated using equation 8. The measured percentage distortion in horizontal and vertical are 0.23% and -0.13%. At the edge of the image,
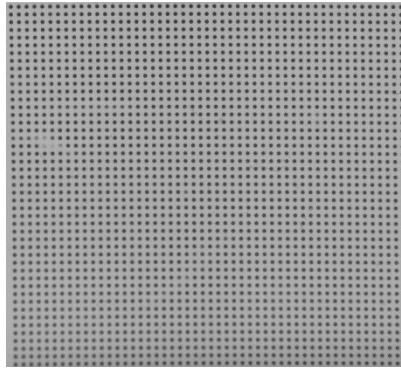
Figure 19. Acquired projection image of the geometric distortion phantom.

the measured percentage distortion in horizontal and vertical are 0.12% and -0.19%. Figure 19 shows an image of the distortion phantom placed in the water tank.

2.3.2.2 MTF measurement

In Figure 20, the modulation transfer function (MTF) plot of the imaging system is presented. The MTF plot provides insight into the system's ability to accurately resolve spatial details. The MTF curve reaches 10% of its maximum value at a spatial frequency of 0.0693 mm, which represents the resolution limit of the optical system. To facilitate a meaningful comparison with the calculated dose distribution, the image size was rescaled to a resolution of 1 mm. This resolution limit corresponds to the resolution of the treatment planning system, allowing for a more accurate and appropriate evaluation of the dose distribution.
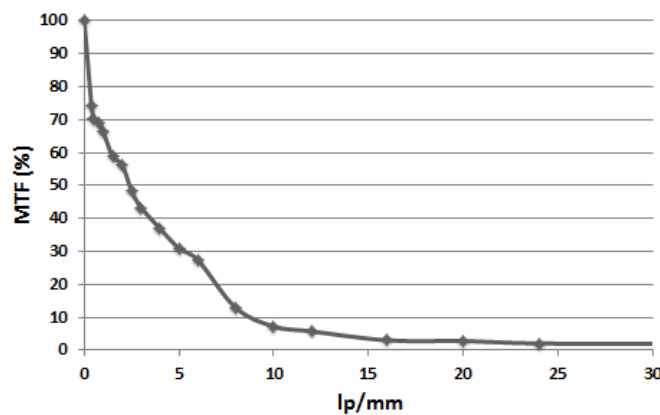
Figure 20. MTF plot of the optical scanner imaging system. The MTF plot provides valuable information about the imaging system's resolution and the preservation of image sharpness across different spatial frequencies.

2.3.2.2 Optical density linearity and SNR
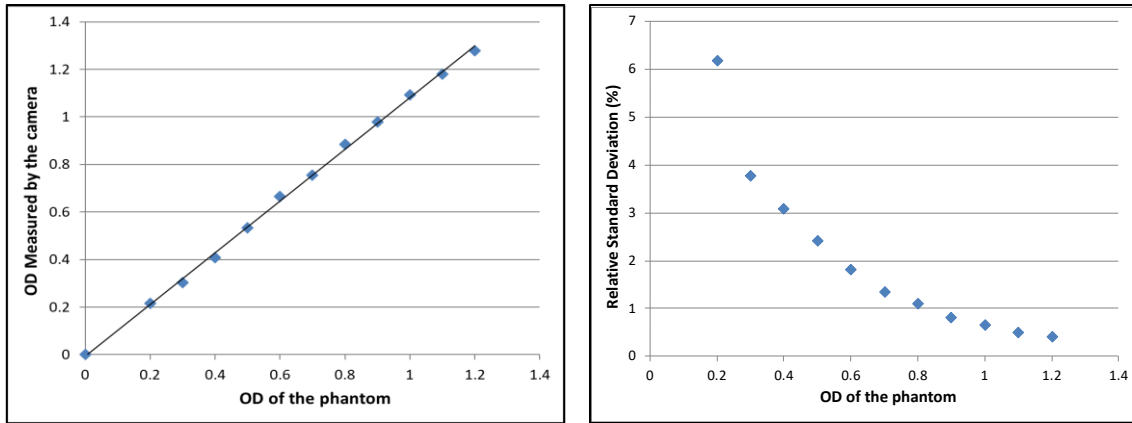
Figure 21. Linear relationship and relative standard deviation of optical density measurements. The figure presents two plots. On the left, there is a plot illustrating the linear relationship between the measured optical density and the vendor-determined optical density of the phantom. On the right, there is a plot showing the relative standard deviation at each optical density level.

By imaging the test target with known optical density materials, the linear relationship between the measured optical density and the actual optical density of the phantom can be plotted (Figure 21). The MAPE of the linear relationship is 1.8%. However, excluding data with optical density lower than 0.5, the MAPE is 0.9%. For optimal dose measurements, the optical densities measured should be controlled to be more than 0.5. The relative standard deviation in a region of interest (ROI) is within 2% for the materials with optical densities more than 0.5, but it can be up to 6% for the materials with optical density at 0.2. The sensitivity of the dosimeter relates to the optical density measured at each dose level. The current formulation of the PRESAGE dosimeter offers the flexibility to choose dosimeters with different sensitivities based on the desired dose range. When performing low dose measurements, it is advisable to select dosimeters with higher sensitivity. This choice ensures that the dosimeter can accurately capture and respond to lower levels of radiation, enabling precise dose measurements in the low dose range.

However, when it comes to high dose measurements, the use of high sensitivity dosimeters can introduce a potential issue. High sensitivity dosimeters may produce image intensities that are

lower than the optimal value for accurate dosimetry. Consequently, the statistical noise originating from the dark image can influence the dosimetry, potentially affecting the precision and reliability of the measured dose distribution.

2.3.3 Dosimetry tests

2.3.3.1 Background subtraction

To evaluate the effect of background subtraction on the reconstructed dose images, three background scanning were conducted and the results of subtraction were evaluated. Between each scan, the dosimeter was taken out of the tank and put back to mimic the real measurement situation. Figure 22 shows the reconstructed image of the three background scans. The structural artifacts are reproducible in the scans and should be subtracted in the ideal situation. Figure 23 shows the line profiles of the three background scans. The location of each peak is similar in each scan. The line profiles of the background scans after subtraction (black: scan1-scan2, red: scan2-scan3) were plotted in Figure 24. The largest peak in Figure 24 is 3 times smaller than the same peak in Figure 23. The standard deviation of the background scan after subtraction is 77% lower than the scan before subtraction. The residual noise can be due to slightly mismatch of each scan when the dosimeter was repositioned and the random noise.
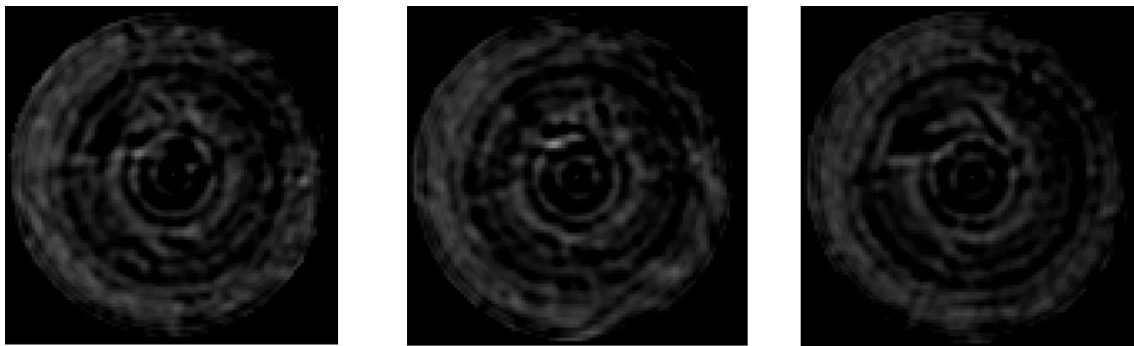
Figure 22. Reconstructed images of three repeated background scans.
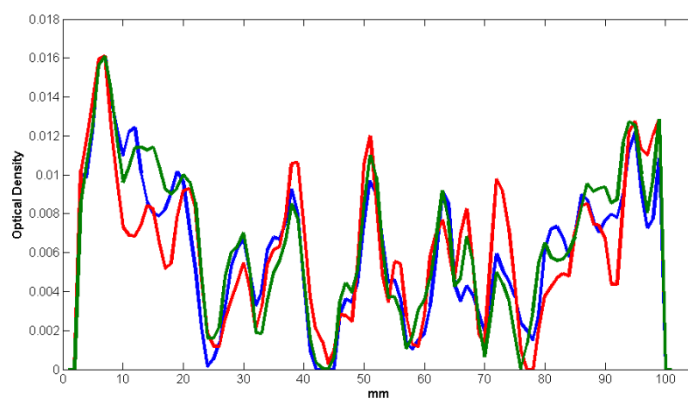
Figure 23. Line profiles of the three background scans.
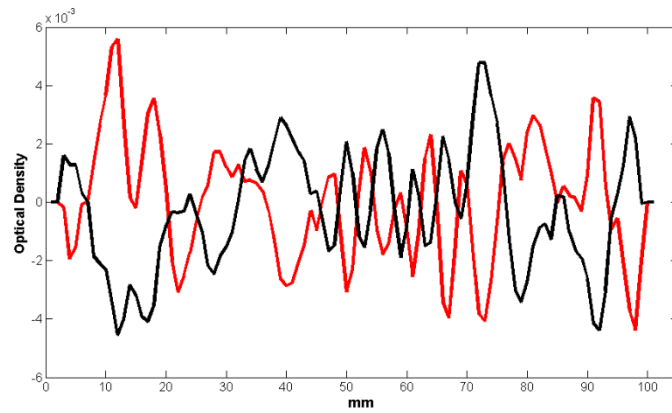
Figure 24. Line profiles of the net background scans after background subtraction. The black line represents the result of subtracting scan 2 from scan 1, while the red line represents the subtraction of scan 3 from scan 2. The analysis of these profiles aids in understanding the effectiveness of background subtraction in minimizing background noise and enhancing the accuracy of subsequent measurements.

2.3.3.2 Dose linearity and SNR

The linearity of the measured optical density to the dose delivered was plotted in Figure 25. The linear plot on the left side is the results with dark field subtraction and the plot on the right side is the results without the dark field subtraction. Dark field subtraction is important especially for high dose measurements. With the dark field subtraction, the MAPE is 0.31% up to 25 Gy. However, without the dark field subtraction, the measured optical densities deviate from the linear line at the high dose region. Percentage errors at 15, 18, 20, and 25 Gy are 1.3%, 6.8%, 10.6%, and 20.1%. With the dark field subtraction, the relative standard deviation in a ROI at each dose level was plotted in Figure 26. The relative standard deviation decreases when the dose delivered increases due to the larger optical densities. It's lower than 2% when the dose delivered is larger than 6 Gy. However, it's important to monitor the image intensity of the high dose measurement. If the intensity is too low, the measurements can be affected by the statistical noise from the dark field.

55
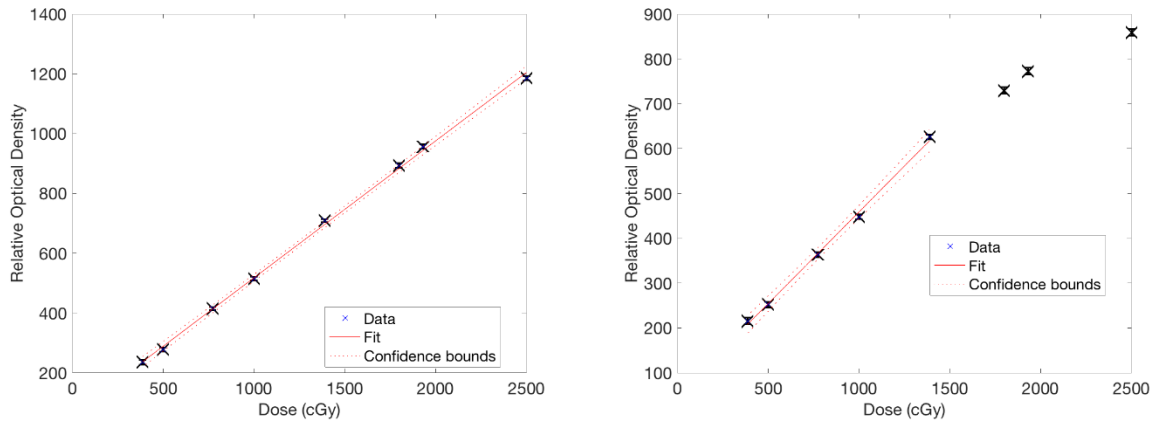
Figure 25. Linearity of measured optical density to dose with (left) and without dark field subtraction (right).
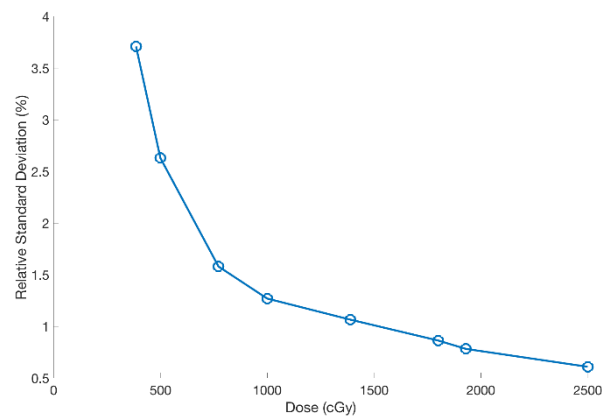
Figure 26. Relative standard deviation at each dose level. This plot depicts the relative standard deviation at each dose level, providing an assessment of the measurement variability across different doses. The x-axis represents the dose levels, while the y-axis represents the relative standard deviation expressed as a percentage.

2.3.3.3 Regular field measurements

Before measuring the clinical treatment fields, regular square fields with 3 cm field size were measured, and the results were compared with the calculated dose from the treatment planning system. In Figure 27, measured results with (right) and without (left) the background subtraction were compared. The gamma passing rate using 2%/2mm criteria for the background subtraction

56

and non-background subtraction scans was 99% and 94%. In the isodose line comparison, the results without background subtraction have less uniform dose distribution and more deviation from the calculated dose in the low dose region (10-30% isodose lines). The isodose lines with the background subtraction correspond to the calculated isodose lines.
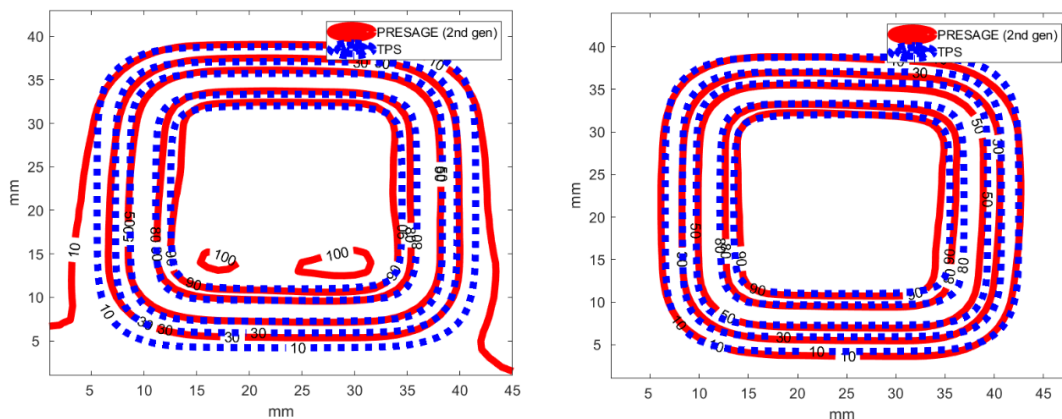
Figure 27. Comparison of isodose lines for the measured and calculated regular field, with (right) and without (left) background subtraction.

2.3.3.4 Treatment filed measurements (SBRT)

The 3D measurement of a SBRT treatment plan with 700 cGy prescription dose was performed. 2D planes in coronal, sagittal, and transverse views were extracted from the 3D measured matrix for the comparison with the calculated dose distribution. 2D gamma tests with 3%/2mm criteria were employed for dose comparison. Figure 28 shows the isodose line comparison between the measured dose distribution and the calculated dose distribution with and without background subtraction. The isodose lines match well except for the regions close to the dosimeter edge. With background subtraction, the gamma passing rates in coronal, sagittal, and transverse view are 99.7%, 99%, and 99.4%. Without background subtraction, the gamma passing rates in coronal, sagittal, and transverse view are 98%, 99%, and 99.3%. Figure 29 shows the line profiles in coronal, sagittal, and transverse view with and without the background subtraction. The local

57

percentage dose difference is around 3% at the edge of the dosimeter. Due to the high dose delivered to the patients, SBRT dose distribution generally has high gradients outside the target. To evaluate the dose distribution in high dose gradient region, 2D dose planes in coronal, sagittal, and transverse views at 1 cm from the isocenter were evaluated. Figure 30 shows the isodose line comparison between the measured and calculated dose distribution. With background subtraction, the gamma passing rates in coronal, sagittal, and transverse view are 99%, 100%, and 98.3%. Without background subtraction, the gamma passing rates in coronal, sagittal, and transverse view are 99%, 98.3%, and 96.6%. The gamma passing rate difference between the results from background subtraction and non-background subtraction at 1 cm from isocenter is larger than those at the isocenter. Figure 31 shows the line profiles in coronal, sagittal, and transverse view with and without the background subtraction. The local percentage dose difference is around 3% at the edge, similar to the isocenter measurements.
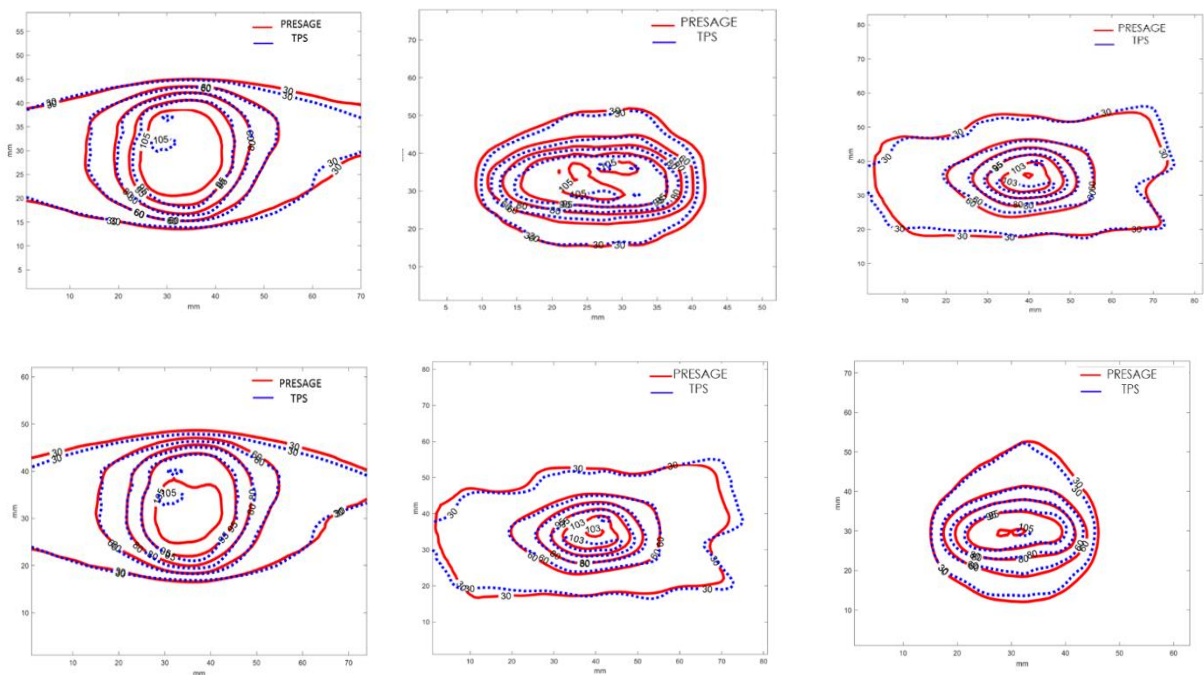
Figure 28. Comparison of isodose lines for the measured and calculated SBRT fields on the transverse (middle), coronal (left), and sagittal (right) plane, with (top) and without (bottom) background subtraction.
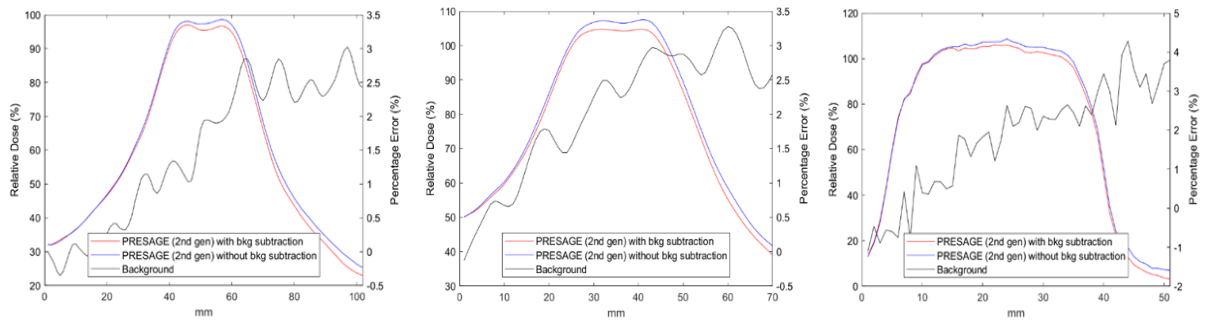
Figure 29. Comparison of line profiles for the measured SBRT fields on the transverse (middle), coronal (left), and sagittal (right) plane, with and without background subtraction.
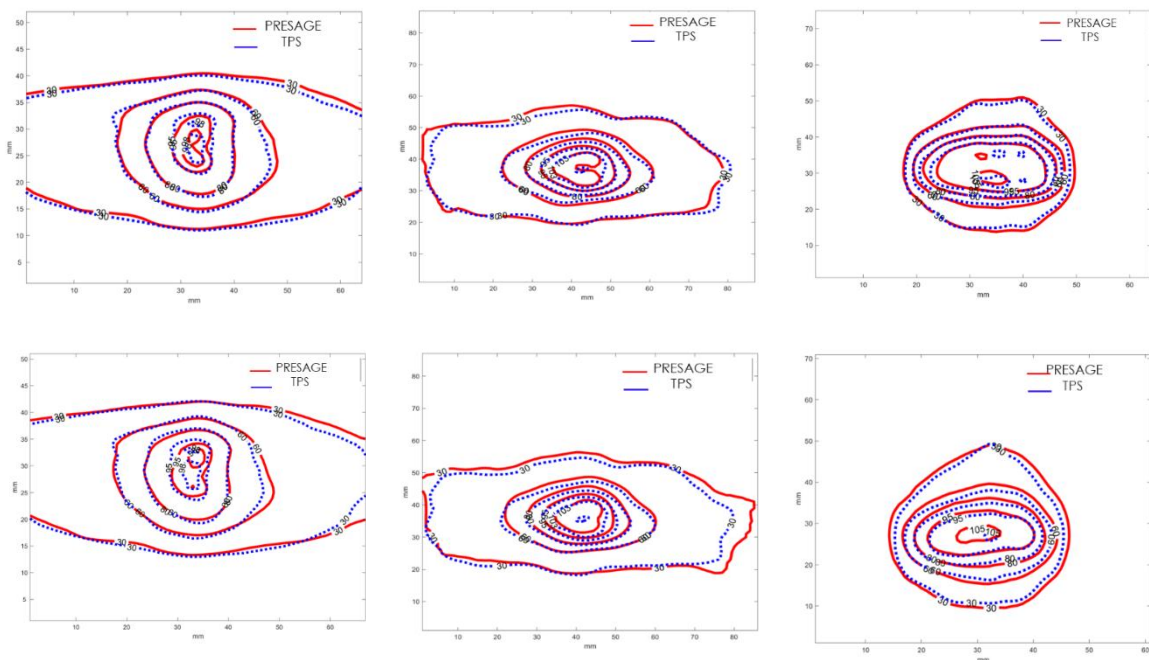
Figure 30. Comparison of isodose lines for the measured and calculated SBRT fields on the transverse (middle), coronal (left), and sagittal (right) plane at 1 cm from the isocenter, with (top) and without (bottom) background subtraction.
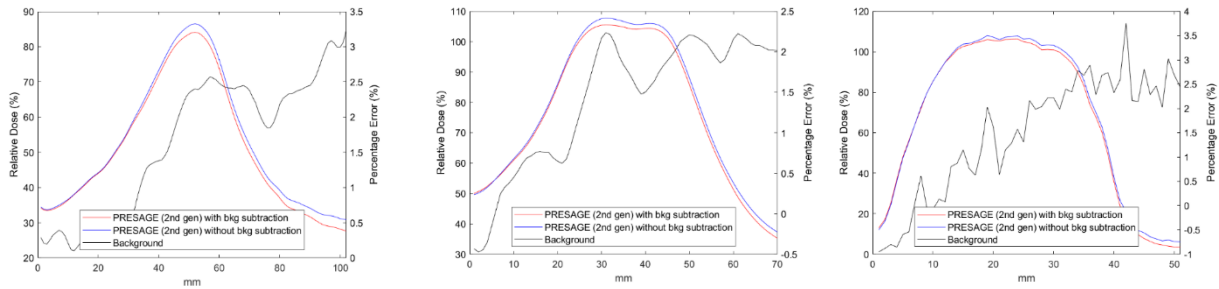
Figure 31. Comparison of line profiles for the measured SBRT fields on the transverse (middle), coronal (left), and sagittal (right) plane at 1 cm from the isocenter, with and without background subtraction.

2.3.3.5 Treatment field measurements (low dose IMRT)

In this section, an IMRT field with 3.6 Gy at the 100% isodose line was measured and compared with the treatment planning system. The reconstructed image from the 3D measurement and the calculated image are shown side-by-side in Figure 32 and the isodose lines comparison are shown in Figure 33. The passing rates using 3%/2mm criteria in the coronal, sagittal, and transverse views are 98.4%, 99.1%, and 97.1%.
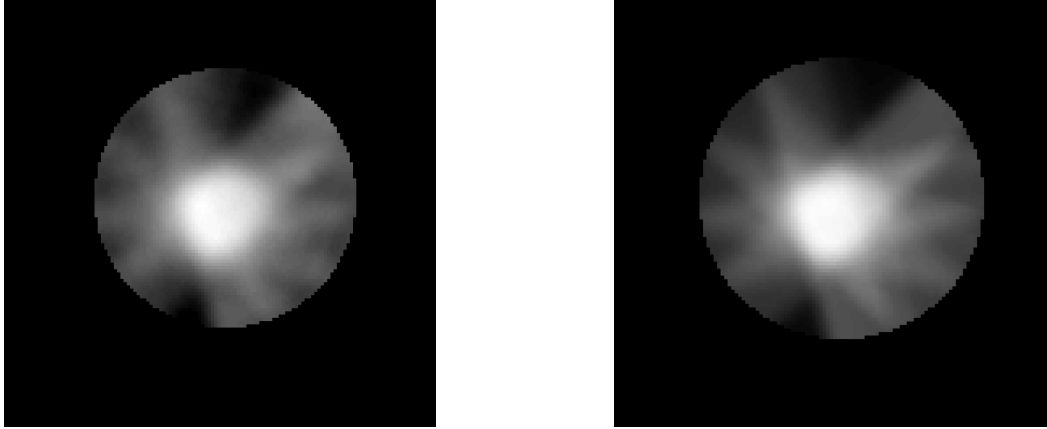
Figure 32. Comparison of the reconstructed dose image from the 3D dosimetry system (left) and the calculated image (right) of an IMRT treatment field.
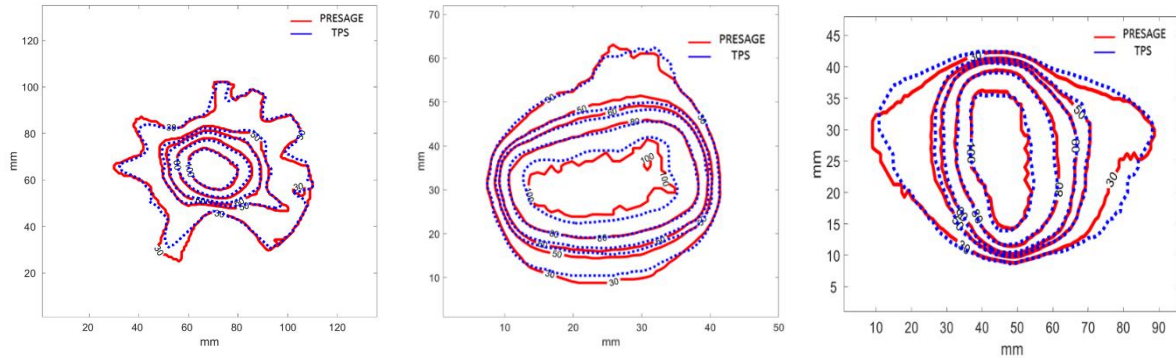
Figure 33. Comparison of isodose lines for the measured and calculated IMRT fields on the transverse (left), coronal (middle), and sagittal (right) plane.

2.3.3.6 Measurement reproducibility

In this section, a single dosimeter was scanned three times to evaluate the reproducibility of the reconstructed images. Figure 34 shows the reconstructed images of the three scans, and Figure 35 shows the isodose lines comparison. The isodose lines in the three scans correspond to each other. To further investigate the difference, gamma tests using 2%/2mm criteria were performed, and the histograms of local percentage dose difference were plotted (Figure 36). The passing rates between

the three scans are all 100%. In the histograms, the mean and standard deviation of the dose difference of the three comparisons are 0.2%±1.1%, 0.2%±0.6%, and 0.4%±1.1%.
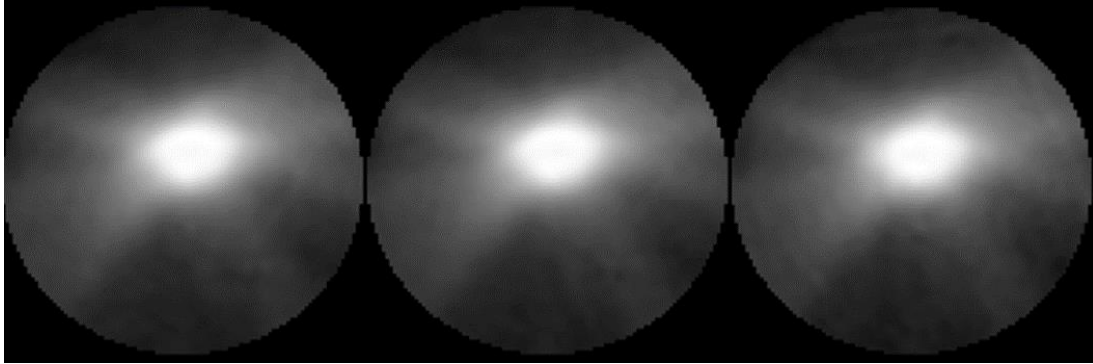
Figure 34. Reconstructed images of the three repeat scans.
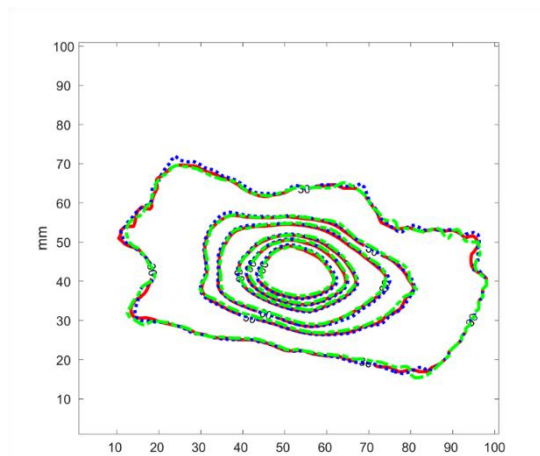
Figure 35. Comparison of the isodose lines from the three repeat measurements
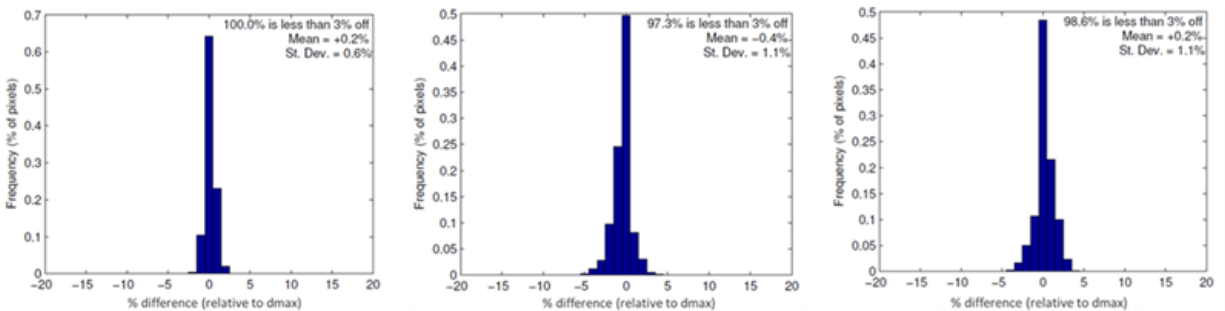
Figure 36. Histograms depicting the local percentage difference of the three repeat scans (Left: scan 1- scan2, middle: scan2-scan3, right: scan1- scan3).

2.3.3.7 EBT3 film comparison

In this section, two IMRT cases were conducted to provide a comprehensive evaluation of the 3D dosimetry results by comparing them with EBT3 radiochromic films. In the first setup, a modulated radiation beam was delivered with the gantry at 0 degrees, targeting both the 3D dosimeter and the film separately. Figure 37 displays the dose images obtained from both the 3D dosimetry system and the radiochromic film, along with a comparison of the corresponding isodose lines. The comparison demonstrates a high level of agreement between the 3D dosimetry system and the radiochromic film. The gamma passing rates, which assess the agreement between the measured and calculated dose distributions, were determined using two criteria: 3% dose difference and 2mm distance-to-agreement, as well as 2% dose difference and 2mm distance-to-agreement. For the first criteria (3%/2mm), the gamma passing rate was determined to be 100%, indicating excellent agreement between the 3D dosimetry system and the radiochromic film. Even with the more stringent criteria of 2%/2mm, the gamma passing rate remained impressively high at 99.8%, further highlighting the reliability and accuracy of the 3D dosimetry system.

(a)
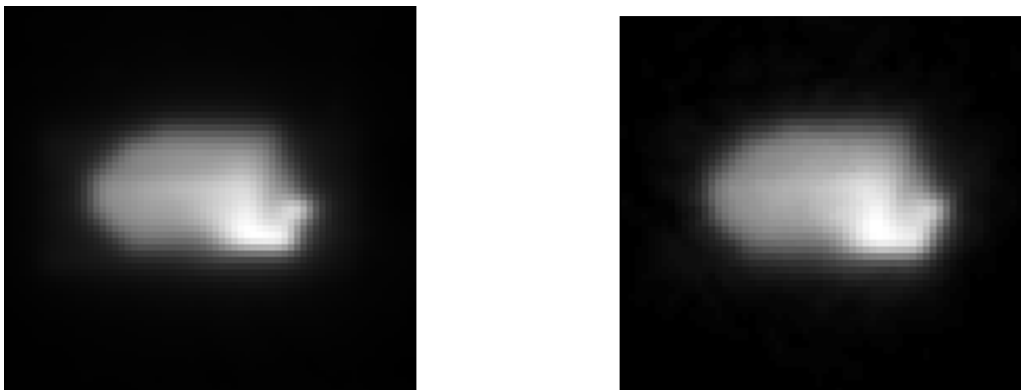
(b)
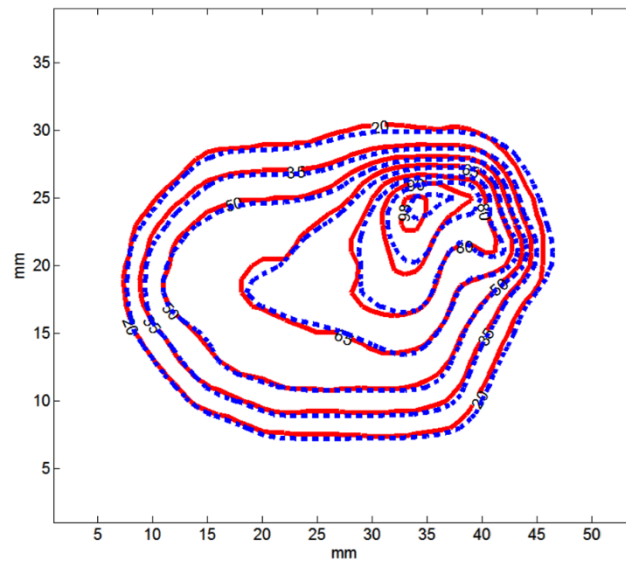
Figure 37. Comparison of a modulated treatment field measurement from a 3D dosimeter and radiochromic film. (a) Acquired dose images from the 3D dosimeter (left) and radiochromic film (right). (b) Isodose line comparison between the 3D dosimeter (red) and radiochromic film (blue).

In the second setup, an IMRT field with multiple different gantry angles was delivered to the film and 3D dosimeter separately. To create the same geometry as 3D dosimeter for the film measurement, a 3D dosimeter was cut in half and a piece of film was placed in between. Figure 38 shows the picture of the irradiated film and the 3D dosimeter used as a film phantom. Figure 39 shows the reconstructed dose image and film image, and the isodose line comparison. Using 3%/3mm and 3%/2mm gamma criteria, the passing rates are 100% and 99.3%. These results provide strong evidence of the capability of the 3D dosimetry system to accurately measure and

analyze radiation dose distributions, effectively corroborated by the excellent agreement observed

when compared to the well-established EBT3 radiochromic films.
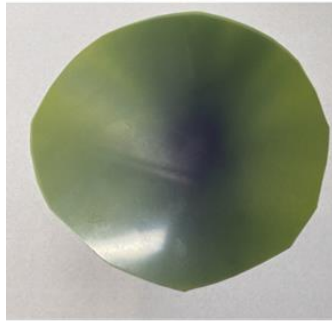
Figure 38. Photographs of the irradiated radiochromic film (left) and the 3D dosimeter phantom for film measurement (right).

(a)

(b)
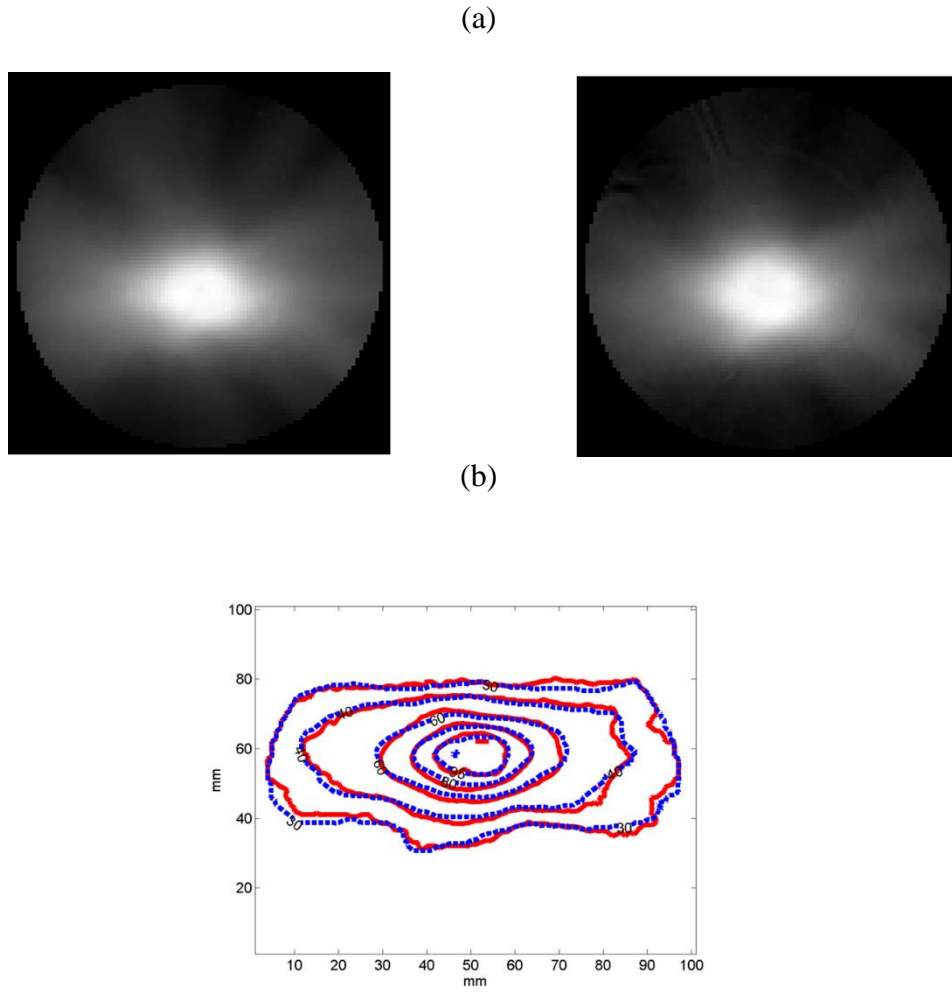
Figure 39. Comparison of a modulated treatment field measurement from a 3D dosimeter and radiochromic film. (a) Acquired dose images from the 3D dosimeter (left) and radiochromic film (right). (b) Isodose line comparison between the 3D dosimeter (red) and radiochromic film (blue).

2.4 Discussion

This study conducted a comprehensive and systematic analysis of the uncertainties associated with a parallel-beam optical CT scanner equipped with a fiber optic taper. The measurement uncertainties in optical CT scanning can be attributed to both mechanical factors and imaging factors. The mechanical uncertainties include factors such as the accuracy of the step motor, the

telecentricity and stability of the light source, and other related mechanical parameters. The imaging uncertainties encompass camera calibration, geometric distortion, resolution, and signal-to-noise ratio. Additionally, factors like stray light, light spectrum change, and the influence of reflection and refraction can impact the accuracy of dose measurements. To evaluate the overall uncertainty, dosimetry tests were performed. The mechanical tests yielded promising results, with a maximum uncertainty of 0.23% originating from source stability. The imaging system demonstrated its capability to provide uniform liquid scans, with a standard deviation of 0.3% after camera calibration. Furthermore, high-resolution images with minimal geometric distortion were achieved, with the largest percentage distortion measuring only 0.23%. The robustness of the system's hardware forms the foundation for an accurate dosimetry system. The relative standard deviation at each optical density level offers insights into the overall imaging uncertainty, which tends to increase as the optical density decreases. At an optical density of 0.2, the uncertainty can reach up to 6%. Therefore, it is crucial for the 3D dosimeter to have sufficient sensitivity, enabling the measurement of larger optical densities for a given dose level. By utilizing optimal dosimeters, the majority of the measured dose range can achieve optical densities higher than 0.6, resulting in relative standard deviations lower than 2%. Finally, the dosimetry tests assess the overall uncertainty in dose measurements at each dose level, as well as the results obtained from regular field and treatment field measurements. These evaluations provide valuable information about the overall accuracy and reliability of the dosimetry system. Overall, the measurement uncertainty depends on the dose delivered. Depending on the sensitivity of the dosimeter, the uncertainty is lower than 2.5% for the dose delivered higher than 5 Gy. Although higher dose can provide larger SNR, the user needs to make sure that measured image intensity is higher than 400, so that the influence of the dark current noise will be smaller than 1%. The image intensity in the projection

image relates to the dose delivered and the length of the dose delivered along the beam path. Exposure time can be adjusted to make sure the measured image intensities are within the optimal range (400, 4000). The gamma comparison shows that the 3D measurements correspond with the calculated dose from treatment planning system and EBT3 film dosimetry well. With gamma criteria 3%/2mm and 2%/2mm, most of the passing rates are within 98%-100%.

The current optical scanner design has some limitations that impact its performance and capabilities. One limitation is the field of view size, which is currently limited to 11 cm $\times$ 7.2 cm. This can be addressed by utilizing a larger optic fiber taper with a larger taper ratio and employing a larger light source. By implementing these modifications, it is possible to achieve a larger field of view, such as 20 cm. Another limitation is related to the dynamic range of the CCD camera used in the scanner. The exposure time needs to be carefully adjusted to ensure that the measured intensities are within the camera's dynamic range and not saturated at either end. However, in cases where the delivered dose is high, the intensity range can exceed the dynamic range of the camera, resulting in the loss of some information. This restricts the current system to performing only relative dose measurements. Furthermore, the sensitivity variation between individual 3D dosimeters presents a limitation in terms of applying a dose calibration curve from one dosimeter to another. This variation hampers the ability to establish a standardized calibration curve that can be universally applied across different dosimeters. This limitation could be addressed through standardized manufacturing processes that ensure greater consistency and reduce the inter-dosimeter variation. Overall, these limitations highlight areas for potential improvement in the optical scanner design, including expanding the field of view, enhancing the dynamic range of the camera, and implementing standardized manufacturing processes to reduce inter-dosimeter variation and enable more reliable dose measurements.

This study also emphasized the importance of background subtraction, and dark field subtraction. The standard deviation of the liquid scan after background subtraction is 77% lower than the scan without subtraction. In the square field and treatment field measurements, background subtraction can improve the measured dose up to 3%. It is noteworthy that background subtraction can also mitigate the influence of the structural artifacts, especially ring artifacts from the dirt on any surface in the beam path. In the future, a compact system to avoid any contamination from the surrounding is important.

2.5 Conclusion

The conducted study presents a comprehensive and systematic approach to benchmark a novel optical CT scanner designed for dosimetry measurements. The scanner demonstrates several advantageous features, including high-resolution 3D dose measurements, minimal stray light contamination, and negligible geometric distortion. Through a series of 21 benchmark tests, encompassing mechanical, imaging, and dosimetry aspects, the study provides valuable insights into measurement uncertainty, operational procedures, and the clinical utility of the scanner. The mechanical tests evaluate the accuracy and stability of the scanner's components, such as the rotational accuracy of the motor and the parallelism of the LED light. The imaging tests assess the system's imaging capabilities, including camera calibration, geometric distortion, resolution, and signal-to-noise ratio. Dosimetry tests investigate the accuracy and reliability of the dose measurements, comparing them with calculated doses from treatment planning systems and EBT3 radiochromic film measurements. The results of these benchmark tests demonstrate the efficacy and reliability of the optical CT scanner for 3D dose measurements. Gamma passing rates, ranging from 98% to 100%, indicate excellent agreement between the measured dose distributions and the expected values. These findings provide strong evidence supporting the clinical and research utility

of the 3D dosimetry system. Overall, the study contributes to the advancement of dosimetry technology by providing a comprehensive evaluation of the novel fiber optic CT scanner and highlighting its potential for clinical implementation and research applications.

References or Bibliography

1. Oldham, M. (2006, December). 3D dosimetry by optical-CT scanning. In Journal of Physics: Conference Series (Vol. 56, No. 1, p. 58). IOP Publishing

2. Sakhalkar, H. S., Adamovics, J., Ibbott, G., & Oldham, M. (2009). A comprehensive evaluation of the PRESAGE/optical-CT 3D dosimetry system. Medical Physics, 36(1), 71-82.

3. Krstajić, N., & Doran, S. J. (2007). Fast laser scanning optical-CT apparatus for 3D radiation dosimetry. Physics in Medicine & Biology, 52(11), N257.

4. Krstajić, N., & Doran, S. J. (2007). Characterization of a parallel-beam CCD optical-CT apparatus for 3D radiation dosimetry. Physics in Medicine & Biology, 52(13), 3693.

5. Sakhalkar, H. S., & Oldham, M. (2008). Fast, high-resolution 3D dosimetry utilizing a novel optical-CT scanner incorporating tertiary telecentric collimation. Medical physics, 35(1), 101-111.

6. Campbell, W. G., Rudko, D. A., Braam, N. A., Wells, D. M., & Jirasek, A. (2013). A prototype fan-beam optical CT scanner for 3D dosimetry. Medical physics, 40(6Part1), 061712.

7. Jordan, K. (2010, November). Review of recent advances in radiochromic materials for 3D dosimetry. In Journal of Physics: Conference Series (Vol. 250, No. 1, p. 012043). IOP Publishing.

8. Gorjiara, T., Hill, R., Kuncic, Z., Adamovics, J., Bosi, S., Kim, J. H., & Baldock, C. (2011). Investigation of radiological properties and water equivalency of PRESAGE® dosimeters. Medical Physics, 38(4), 2265-2274.

9. Khezerloo, D., Nedaie, H. A., Takavar, A., Zirak, A., Farhood, B., Movahedinejhad, H., ... & Knuap, C. (2017). PRESAGE® as a solid 3-D radiation dosimeter: A review article. Radiation Physics and Chemistry, 141, 88-97.

10. Guo, P., Adamovics, J., & Oldham, M. (2005). PRESAGE-A promising new material for 3D dosimetry. International Journal of Radiation Oncology, Biology, Physics, 63, S206.

11. Khezerloo, D., Nedaie, H. A., Farhood, B., Zirak, A., Takavar, A., Banaee, N., ... & Kron, T. (2017). Optical computed tomography in PRESAGE® three-dimensional dosimetry: Challenges and prospective. Journal of cancer research and therapeutics, 13(3), 419-424.

12. Krstajić, N., Wai, P., Adamovics, J., & Doran, S. (2004). Spectrophotometry of PRESAGE™ polyurethane dosimeters. In Journal of Physics: Conference Series (Vol. 3, No. 1, p. 244). IOP Publishing.

13. Lauritsch, G., & Härer, W. H. (1998, June). Theoretical framework for filtered back projection in tomosynthesis. In Medical Imaging 1998: Image Processing (Vol. 3338, pp. 1127-1137). SPIE.

14. Oldham, M., & Kim, L. (2004). Optical-CT gel-dosimetry II: Optical artifacts and geometrical distortion. Medical physics, 31(5), 1093-1104.

15. Sakhalkar, H. S., & Oldham, M. (2008). Fast, high-resolution 3D dosimetry utilizing a novel optical-CT scanner incorporating tertiary telecentric collimation. Medical physics, 35(1), 101-111.

16. Sakhalkar, H. S., Adamovics, J., Ibbott, G., & Oldham, M. (2009). A comprehensive evaluation of the PRESAGE/optical-CT 3D dosimetry system. Medical Physics, 36(1), 71-82.

17. Xu, Y., Wuu, C. S., & Maryanski, M. J. (2004). Performance of a commercial optical CT scanner and polymer gel dosimeters for 3-D dose verification: optical CT scanning of polymer gel. Medical physics, 31(11), 3024-3033.

18. Clift, C., Thomas, A., Adamovics, J., Chang, Z., Das, I., & Oldham, M. (2010). Toward acquiring comprehensive radiosurgery field commissioning data using the PRESAGE®/optical-CT 3D dosimetry system. Physics in Medicine & Biology, 55(5), 1279.

19. Islam, K. T. S., Dempsey, J. F., Ranade, M. K., Maryanski, M. J., & Low, D. A. (2003). Initial evaluation of commercial optical CT-based 3D gel dosimeter. Medical Physics, 30(8), 2159-2168.

20. Wang, Z., Thomas, A., Newton, J., Ibbott, G., Deasy, J., & Oldham, M. (2010, November). Dose verification of stereotactic radiosurgery treatment for trigeminal neuralgia with presage 3D dosimetry system. In Journal of Physics: Conference Series (Vol. 250, No. 1, p. 012058). IOP Publishing.

21. Thomas, A., Pierquet, M., Jordan, K., & Oldham, M. (2011). A method to correct for spectral artifacts in optical-CT dosimetry. Physics in Medicine & Biology, 56(11), 3403.

22. Oldham, M., Thomas, A., O'Daniel, J., Juang, T., Ibbott, G., Adamovics, J., & Kirkpatrick, J. P. (2012). A quality assurance method that utilizes 3D dosimetry and facilitates clinical interpretation. International Journal of Radiation Oncology* Biology* Physics, 84(2), 540-546.

23. Thomas, A., Newton, J., & Oldham, M. (2011). A method to correct for stray light in telecentric optical-CT imaging of radiochromic dosimeters. Physics in Medicine & Biology, 56(14), 4433.

24. Miles, D., Yoon, P., Kodra, J., Adamovics, J., & Oldham, M. (2017, May). A prototype optical-CT system for PRESAGE 3D dosimeter readout. In Journal of Physics: Conference Series (Vol. 847, No. 1, p. 012026). IOP Publishing.

25. Liu, H., Karellas, A., Harris, L. J., & D'Orsi, C. J. (1993, September). Optical properties of fiber tapers and their impact on the performance of a fiber optically coupled CCD x-ray imaging system. In Clinical Applications of Modern Imaging Technology (Vol. 1894, pp. 136-147). SPIE.

26. Xue, S., van Eijkelenborg, M. A., Barton, G. W., & Hambley, P. (2007). Theoretical, numerical, and experimental analysis of optical fiber tapering. Journal of Lightwave Technology, 25(5), 1169-1176.

27. Bagad, V. S. (2007). Optical Fiber Communication. Technical Publications Pune

28. Snyder, A. W., Pask, C., & Mitchell, D. J. (1973). Light-acceptance property of an optical fiber. JOSA, 63(1), 59-64.

29. Schroeder, M. R. (1981). Modulation transfer functions: Definition and measurement. Acta Acustica united with Acustica, 49(3), 179-182.

30. Niroomand-Rad, A., Chiu-Tsao, S. T., Grams, M. P., Lewis, D. F., Soares, C. G., Van Battum, L. J., ... & Chan, M. F. (2020). Report of AAPM task group 235 radiochromic film dosimetry: an update to TG-55. Medical physics, 47(12), 5986-6025.

31. Girard, F., Bouchard, H., & Lacroix, F. (2012). Reference dosimetry using radiochromic film. Journal of applied clinical medical physics, 13(6), 339-353.

32. Healey, G., & Kondepudy, R. (1992, January). CCD camera calibration and noise estimation. In Proceedings 1992 IEEE Computer Society Conference on Computer Vision and Pattern Recognition (pp. 90-91). IEEE Computer Society.

33. Beyer, H. A. (1992, January). Accurate calibration of CCD-cameras. In Proceedings 1992 IEEE Computer Society Conference on Computer Vision and Pattern Recognition (pp. 96-97). IEEE Computer Society.

34. Khair, U., Fahmi, H., Al Hakim, S., & Rahim, R. (2017, December). Forecasting error calculation w. ith mean absolute deviation and mean absolute percentage error. In journal of physics: conference series (Vol. 930, No. 1, p. 012002). IOP Publishing.

35. Low, D. A., & Dempsey, J. F. (2003). Evaluation of the gamma dose distribution comparison method. Medical physics, 30(9), 2455-2464.

36. Thomas, A., Newton, J., & Oldham, M. (2011). A method to correct for stray light in telecentric optical-CT imaging of radiochromic dosimeters. Physics in Medicine & Biology, 56(14), 4433.

Chapter 3

Fiducial Detection and Registration for 3D IMRT QA with Organ-Specific Dose Information

3.1 Introduction

Intensity modulated radiation therapy (IMRT) quality assurance (QA) or patient-specific QA has been widely performed in the clinic to verify treatment planning dose calculation as well as the delivery system of a linear accelerator (LINAC) with multileaf collimators (MLCs)[1-4]. However, its sensitivity in detecting errors and its relevance to clinical judgment has been extensively discussed by physicists[5-8]. In 2018, AAPM task group 218 was published in order to address the issues of IMRT QA and review the existing measurement-based methods and computer reconstruction methods[9]. It was concluded that the conventional gamma test should be reviewed on a structure by structure basis if the QA method allows for it. Purely using the passing rate for evaluation could underestimate the clinical consequences because the passing rate only summarizes the gamma test in aggregate. In addition, computed and measured DVH comparisons can provide more clinically relevant information. The study also addressed that the dose difference criterion would ideally be customized for different anatomical structures and the predicted dose in the structures. For example, the dose criterion in the spinal cord for a predicted cord dose of 45 Gy should be tighter than the tolerance in the cord with a predicted dose of 20 Gy. A recent study evaluated current measurement-based QA at multiple institutions using the IROC head and neck IMRT phantom[10]. The results showed that traditional IMRT QA methods performed consistently poorly in searching for a large error or a moderate error regardless of whether a 3%/3 mm or a 2%/2 mm criteria was used.

This work aims to resolve the issues regarding IMRT QA by demonstrating a measurement-based methodology using fiducial registration and structure-mapping to acquire organ-specific dose information. PRESAGE 3D dosimeters (Heuris Inc.) have been recognized as true 3D dosimeters because dose deposition in the 3D space is readout using an optical scanner with no computer

modeling involved[11,12]. The dosimeter consists of an optically clear polyurethane matrix, containing a leuco dye and free radical initiators that exhibits a radiochromic response when exposed to ionizing radiation. In 2012, the first comprehensive application of 3D dosimetry to verify a complex radiation treatment was proposed[13]. The novelty of this work was to transform measured 3D dose distribution in the phantom back to the patient CT data, and thus enabling DVHs comparison. However, the study addressed that the methodology was limited to the accuracy of the 3D dose measurement, as well as the dose transformation between the phantom CT and the patient CT since the dose deposition at the two different geometries cannot be adequately described by a simple transformation matrix. Also, it was not clear how the correlation between the coordinates of the evaluation space and the reference space was established.

Furthermore, several publications have shown 3D dose measurement of IMRT fields using different types of 3D dosimeters (Gel, PRESAGE etc) and dose read-out tools11,[14-23]. One of the most significant source of errors remains in the 3D registration between the measured dose and planned dose, which requires fiducial markers to be shown with sufficient contrast in two different image modalities, simulation CT and optical CT. The registration error is important for 3D measurement-based QA because the dosimeters were read-out by an optical CT scanner with different orientations than the CT scan. No previous research has analyzed the effect of the registration errors in 3D dose comparison, or have reported the accuracy of the registration. Previous studies have addressed that the result of registration errors in the manual alignment of the measured and calculated dose distributions leads to the gamma failing points at the sharp dose gradient regions[15,18]. A robust and accurate registration between the treatment planning coordinates and the dosimeter coordinates is therefore one of the key components to true 3D dose comparison. One could find the 'best match' through the extended use of manual registration.

However, a rigorous and fair dose distribution comparison cannot be established when exclusive manual registration is used to align the dose distributions and the results are operator-dependent. This study aims to resolve these concerns by proposing a methodology using automatic fiducial registration algorithm and commercially available structure-mapping application in clinical TPS. First of all, fiducial-based registration was employed to register the optical CT dose images to the simulation CT dosimeter images in order to correlate the two coordinate systems. Secondly, using the coordinates of the fiducials, patients' anatomical structures were mapped to the dosimeter coordinates for structure-by-structure 3D dose comparison using Eclipse structure mapping application (Varian Inc). Finally, measured and calculated 3D dose distributions on the phantom were compared using clinically relevant information such as dose volume histogram (DVH), 2D dose distribution in any arbitrary plane and spatial positions of the failing gamma points in 3D. The main goal of this work is to propose a robust methodology of 3D measurement-based IMRT QA with organ-specific dose information and demonstrate its clinical feasibility. With the acquired information, organ-specific dose difference criterion could be implemented in the future.

3.2 Materials and Methods

3.2.1 3D IMRT QA with Organ-Specific Dose Information

The proposed methodology includes four main phases: CT simulation, dosimeter irradiation, dosimeter readout, and registration. In the first phase, six CT skin markers (Beekley Medical Inc.) were placed on the PRESAGE dosimeter with two purposes: setting up the dosimeter for the CT simulation and irradiation, and registration between the measured dose distribution and calculated dose distribution. Figure 1 shows the dimensions of the dosimeter and the relative positions of the six fiducials. Fiducial A, B, and C were aligned to the lasers before the CT simulation and treatment field irradiation. Fiducial D was used for left-right discrimination when it was placed on the couch.

77

Fiducial A, C, E, and F were employed as the registration markers. The geometrical positions of the fiducials were designed to achieve the optimal target registration errors, which were both calculated and measured in the study. As shown in Figure 2, the dosimeter was placed on the couch with the axial plane perpendicular to the couch surface. A CT simulator, SOMATOM Definition AS (Sienmens, Inc) was used to acquire CT images of the dosimeter with 120 kVp and 1 mm slice thickness. In this study, two real patient plans were used as examples. The first case is a VMAT treatment of cerebellar metastasis (Figure 2) with a total dose of 27 Gy in three fractions; the second case is a single isocenter, multiple lesions VMAT treatment of secondary malignant neoplasm of brain with 21 Gy in three fractions. The Acuros-XB dose calculation algorithm (version 15.6, Varian, Inc) was used to calculate the dose distribution with a 1 mm calculation grid size, and hybrid plan verification of the VMAT treatment plans were created (Figure 2) with the same dose grid size. A shift in the longitudinal direction was used to move the irradiation isocenter from the setup position to the central region of the dosimeter. With the setup fiducials, the setup position can be accurately identified. Using Eclipse image registration software, PRESAGE CT images were registered to the patient CT images based on the irradiation isocenter and then the anatomical structures (GTV, PTV, brain stem, chiasm, left cochlea and right cochlea) from the patient CT image volume were mapped to the registered PRESAGE CT images volume (Figure 3). After the treatment plan preparation, the dosimeter was positioned in the treatment room for the irradiation of the verification plan using a Varian TrueBeam LINAC (Varian, Inc). In this study, the dosimeter received only one fraction of dose while in the Results section, the measured dose was scaled to the prescribed total dose for the presentation.
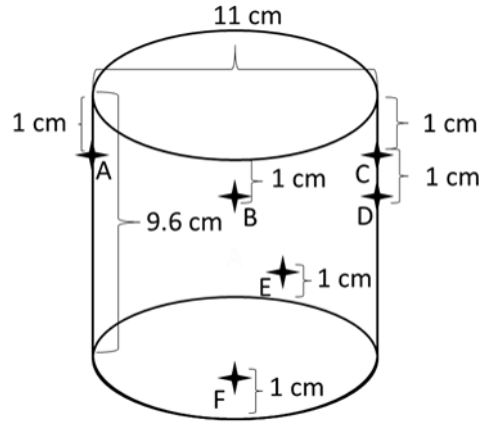
Figure 4. Diagram of a PRESAGE dosimeter with six fiducials placed on the surface.
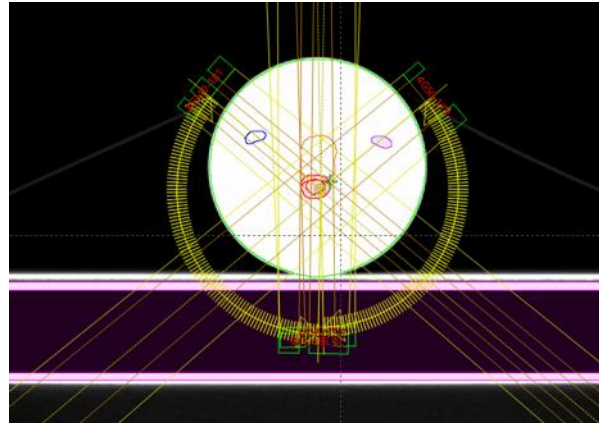
Figure 5. An axial view of a PRESAGE dosimeter placed on the treatment couch.

After irradiation, the 3D dose distribution of the irradiated dosimeter was readout by a single laser beam optical-CT scanner (OCT) modified from the OCTOPUSTM scanner11 at our institution. Four hundred projections were generated for one slice with slice thickness of 1 mm. For each projection (13.5 cm), 5000 data points were acquired. 3D dose images with submillimeter resolution were reconstructed using filtered back-projection algorithm. An in-house MATLAB (MathWorks, Inc) code was developed to perform the reconstruction algorithm and an automatic fiducial localization algorithm to register the markers in the OCT dose images to the CT simulation

79

images. Figure 4 shows each step of the algorithm. Before localizing the markers, three image sets, CT simulation images, calculated dose images, OCT dose images were resampled to have the same size and resolution (1 mm). A region of interests (ROI) was selected to reduce the image size and pixels with image intensities higher or lower than a specific range were filtered out. In the marker localization phase, the prominence, of each pixel was calculated for both the CT and OCT image sets. The prominence measures how one pixel stands out from the surrounding pixels. Four pixels with the highest prominence values were selected in both image sets representing the fiducial points. Using singular-value decomposition, rotation (R) and translation matrix (t) for the point-based registration were found[24]:

$$XY^t = U\Lambda V^t \tag{1}$$
$$R = VDU^t \tag{2}$$
$$t = \bar{y} - R\bar{x} \tag{3}$$

, where X, Y are the matrices, consisting of three rows and four columns. U, V are left and right singular vector matrices. The elements of each column in X and Y are the coordinates of the four fiducial points in the two image sets. respectively. $D = diag(1,1,\det(VU))$, $\bar{x}$ and $\bar{y}$ are the first column in X and Y. By applying the rotation and translation matrix to the OCT images, the OCT images were registered to the CT images and the calculated dose images from TPS (Figure 5). All the medical images, structures and dose images were imported to 3D Slicer, an open-source software platform for image processing and visualization. SlicerRT, an extension of 3D Slicer,

was employed in this study to visualize the structure sets, the measured and calculated dose distributions on the phantom as well as to calculate the DVHs, isodose lines, and gamma index.

3.2.2 Registration Error Estimation

The overall dose comparison errors between calculated dose on the phantom and measured dose include real delivery errors to be detected, dosimetry uncertainties and registration errors between two different image modalities, CT, and OCT dose images in 3D. Previous studies have examined the dosimetry uncertainties using 3D dosimeters and various read-out techniques extensively[11, 14-23] while the registration errors have not been analyzed in detail. In this study, fiducial localization error (FLE), which is the error in locating the fiducials, fiducial registration error (FRE), which is the root mean square distance between corresponding fiducials after registration, and target registration error (TRE), which is the distance between corresponding targets (not fiducials) after registration, were used to evaluate the fiducial registration technique. FRE was evaluated by comparing the coordinates of the fiducial points in the registered OCT images and the CT images. Twenty fiducials were registered to evaluate FRE. By using approximate expressions derived by Fitzpatrick et al., the expected squared FLE can be calculated from FRE[25,26,27]:

$$\left\langle FRE^2 \right\rangle = ((N-2)/N)\left\langle FLE^2 \right\rangle \qquad (4)$$

where N is the number of the fiducials. The expected squared FLE can be used in the following equation to predict the expected squared TRE at a point r:

$$\left\langle TRE^2(r) \right\rangle \approx \frac{\left\langle FLE^2 \right\rangle}{N}\left(1 + \frac{1}{3}\sum_{k=1}^{3}\frac{d_k^2}{f_k^2}\right) \qquad (5)$$

81

where $\langle FLE^2 \rangle$ is the expected squared FLE, and N is the number of the fiducials. d_k is the root-mean-square (RMS) distance to axis k for the evaluated point, r, and f_k is the RMS distance to axis k for the fiducials. FLE and FRE relate to the image qualities of the OCT and CT images while TRE is influenced by the number and the location of the fiducials placed on the PRESAGE phantom. In this study, TRE was calculated and directly measured. To directly measure TRE, four fiducials were placed on the phantom as registration markers and ten fiducials were placed on the same phantom as the targets for evaluation.
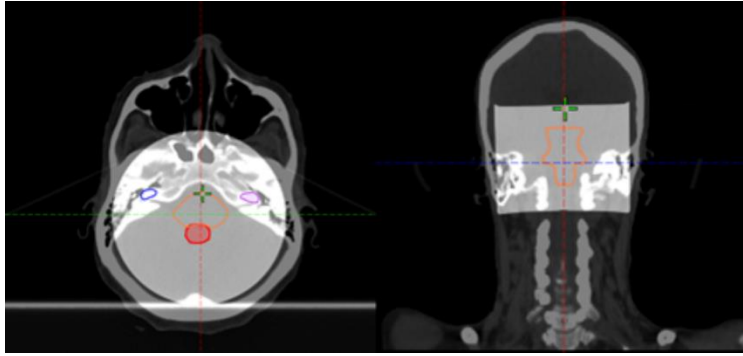
Figure 6. Mapping patient's anatomical structures from patient's CT image volume to phantom's CT image volume. The two image volumes were registered based on the treatment plan isocenter. (Left: axial view, Right: coronal view)
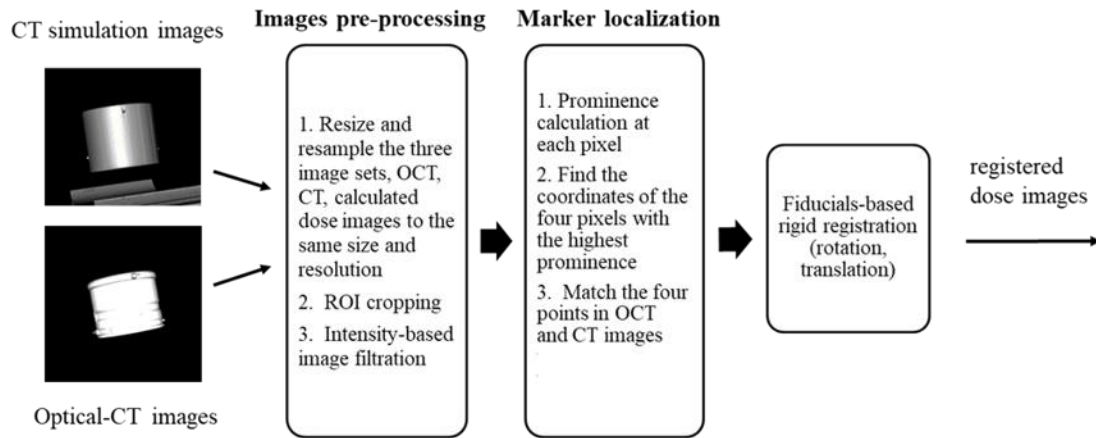
Figure 7. Schematic diagram of the developed algorithm for automatic fiducial detection and registration.
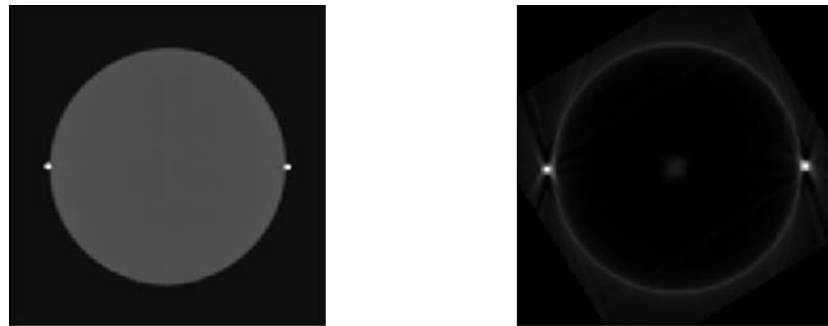
Figure 8. Registered CT simulation images (left) and OCT reconstructed images (right)

3.3 Results

3.3.1 3D IMRT QA With Organ-Specific Dose Information

The proposed 3D IMRT QA method can provide relevant clinical information for the patient's treatment plan, including evaluation of 2D isodose lines and gamma index at any arbitrary plane, 3D views of the dose distribution and structures, DVH of the targets and organs at risks (OAR), 3D gamma index and the location of the failing points relative to the structures. In the first case, a

VMAT plan for cerebellar metastasis was selected for the demonstration. Figure 6 shows the results of the measured dose distribution and its relative location to the structures from 3D Slicer. In this case, the target is close to the brainstem and thus, sparing of the OAR is critical. With the proposed method, dose fall- off in the high dose gradient region between the target and the OAR can be evaluated.

In Figure 7, isodose line comparison of the measured and calculated dose distribution on three orthogonal planes is presented. 2D isodose comparison is a straightforward evaluation of the measured dose distribution. The presented case shows a good agreement between the measurement and the calculation at all dose levels except for the hot spots. The maximum doses of the calculated and measured dose distributions were 109% and 103%, respectively. Gamma analysis showed the passing rates of 99% for all three orthogonal planes respectively (using 3% and 3 mm criteria) and 97%, 98%, and 97% for the transverse, sagittal and coronal planes (using 3% and 2 mm criteria). In addition to conventional 2D dose comparison, using the SlicerRT, we can calculate the DVHs and 3D gamma. Figure 8 presents the DVH comparison between the calculation and the measurement for this examined case. The measured coverage for the target is slightly lower than the calculated one. For the GTV and PTV, V27Gy is 100% and 93.7% in the calculated dose distribution and 99.2% and 91.4% in the measured distribution. In addition, the hot spot value from the measurement (113%) is higher than what obtained by calculation (109%). For the brainstem, the measured mean dose and maximum dose were 5.5 Gy and 24.7 Gy while the calculated doses were 5.5 Gy and 24.3 Gy respectively. The received maximum dose of the right and left cochlea are much smaller than the constraint (17 Gy) in this plan. The calculated maximum dose of the right and left cochlea were 5.49 Gy and 6.75 Gy while the measured were 5.67 Gy and 6.39 Gy.

In addition to the DVH comparison, 3D gamma analysis was performed on the measured and calculated dose matrices. The passing rates were 99.2% and 96% using 3%, 3 mm and 3%, 2 mm criteria (with a 30% threshold). However, merely looking at the passing rate is challenging to make a clinical judgment. Using 3D Slicer, pixels that fail the 3%, 3 mm gamma test can be shown in 3D space (Figure 9). The failing pixels are mostly in the region of a steep dose fall-off outside the PTV, where the coverage of the PTV is influenced.

In the second case, three malignant lesions in brain, PTV at the frontal lobe (PTV frontal), PTV near thalamus (PTV thalamus) and PTV near globus pallidus (PTV GP) were irradiated using three non-coplanar arcs with a single isocenter. Figure 10 shows the measured dose distribution in 3D using 3D Slicer. In this case, high gradient dose regions were scattered at different places to cover three targets. Both OAR, chiasm and brain stem were in the low dose region. The proposed method not only assessed the dose coverage of individual lesions but also the dose fall-off outside the targets and low dose spill into normal brain.

An oblique slice showing three targets was extracted from the 3D measured dose volume and compared with the calculated dose. Figure 11 and 12 show the reconstructed image and planning image of the slice as well as their dose distribution comparison. The gamma passing rates of this slice are 96.2% and 91.6% using 3%/3mm and 3%/2mm criteria. The measured dose in region connecting the two close targets were higher than the calculated dose. Figure 13 presents the DVH comparison of the measured and calculated organ dose. The measurement shows that 95% of PTV Frontal, PTV Thalamus and PTV GP receive at least 21.9, 21.3 and 22.1 Gy with maximum dose of 26 Gy while the calculation shows that 95% of PTV Frontal, PTV Thalamus and PTV GP receive at least 21.1, 21.1 and 21.7 Gy with maximum dose of 25 Gy. For chiasm, the measured maximum dose is 2 Gy and calculated maximum dose is 2.25 Gy. Brain stem dose from calculation

and measurement were both much lower than the constraint, 12 Gy. The 3D gamma passing rates were 98.03% and 91.52% using 3%, 3 mm and 3%, 2 mm criteria. Most of the gamma failing points are at the intermediate dose region (50-70%) between the two close lesions.
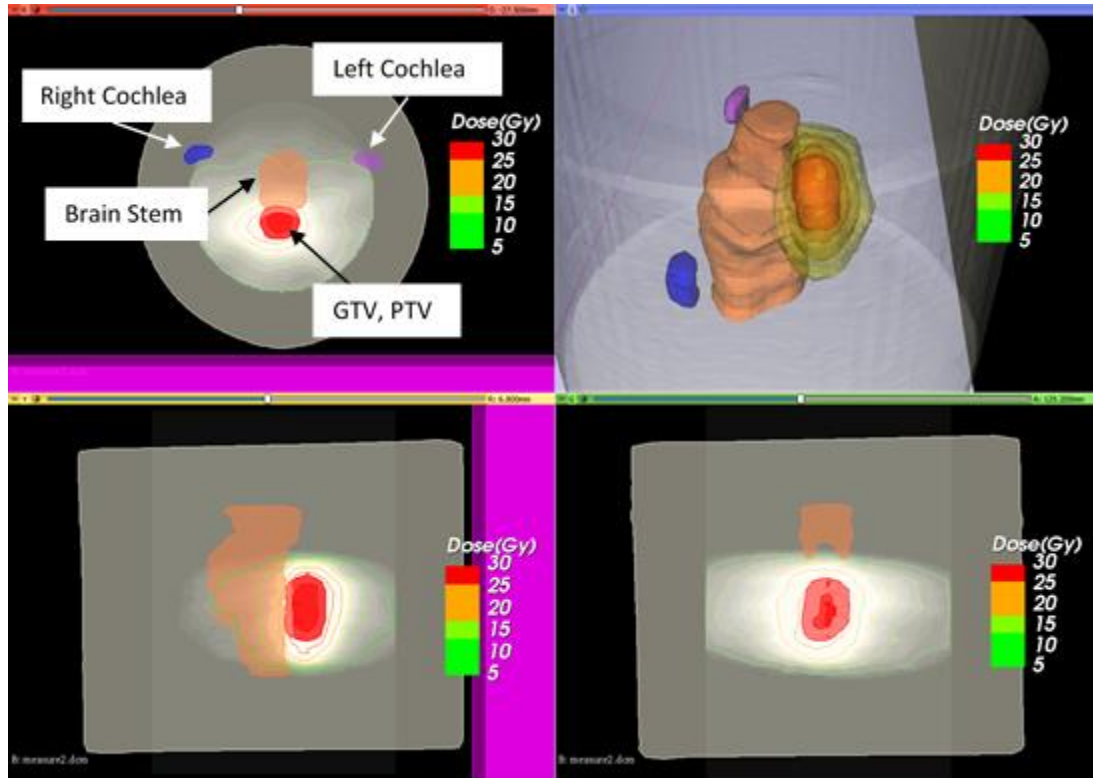
Figure 9. Imported 3D measured dose distribution of the cerebellar metastasis case and patient's anatomical structures in 3D Slicer.
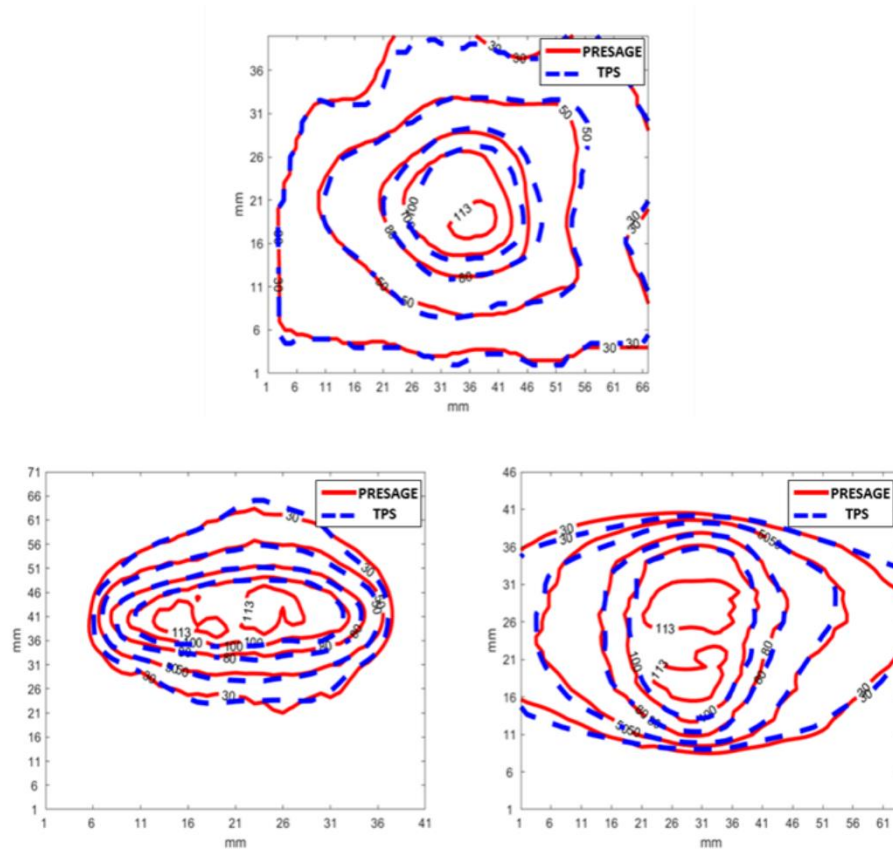
Figure 10. Three orthogonal views of the measured (red) and TPS-calculated (blue) dose distribution comparison
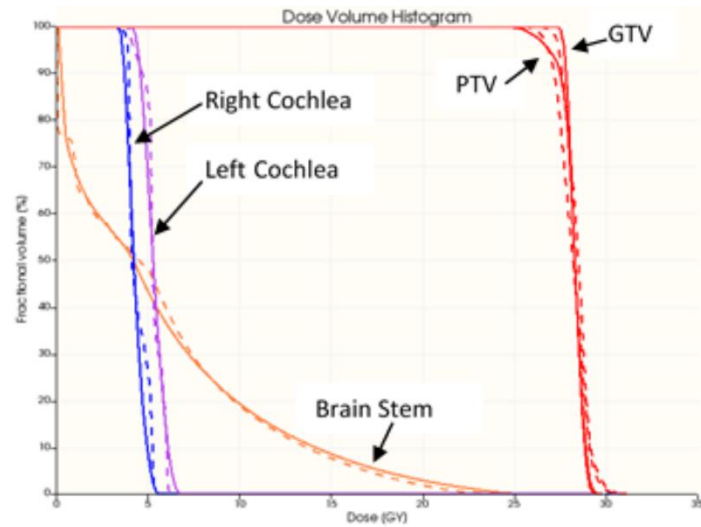
Figure 11. DVH comparison of the measurement (dashed line) and TPS-calculation (solid line) of the cerebellar metastasis case.
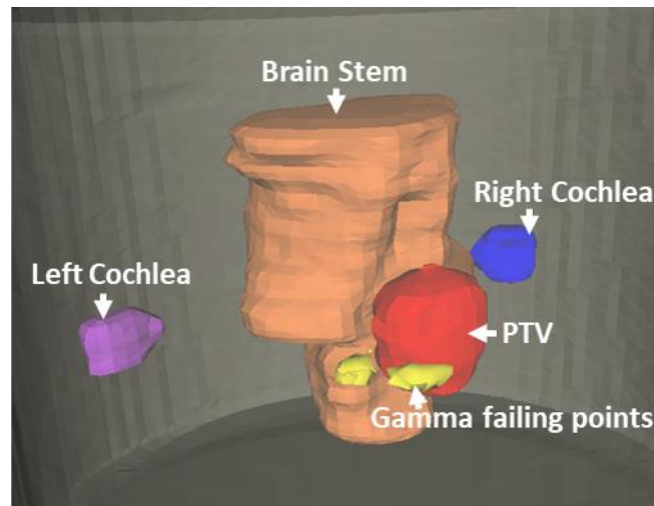
Figure 9. Visualization of the gamma failing points (yellow) in 3D space.
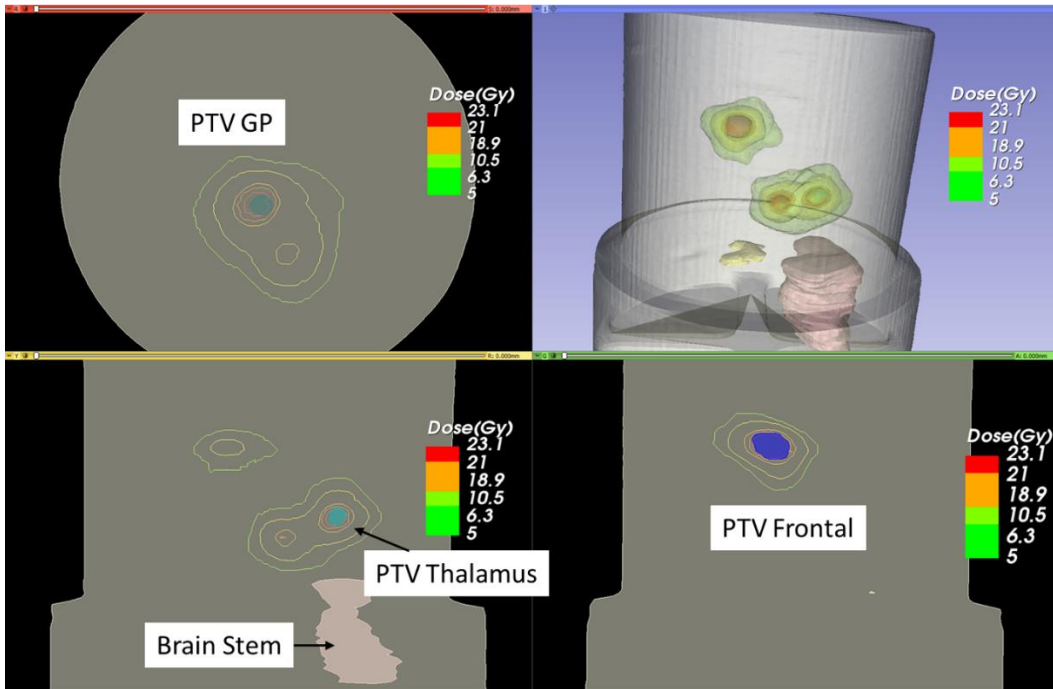
Figure 12. Imported 3D measured dose distribution of the multi-lesions case and patient's anatomical structures in 3D Slicer.
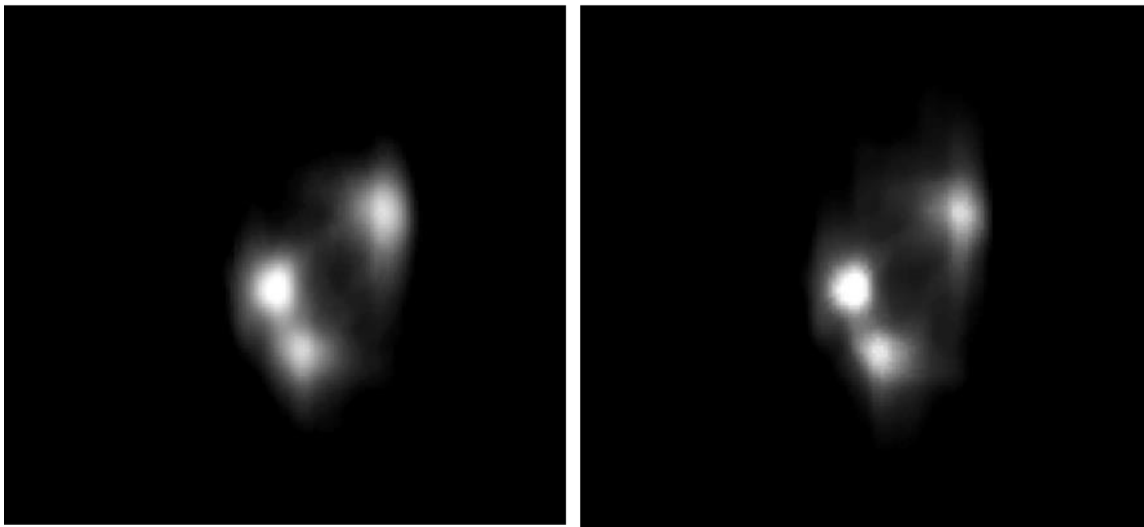
Figure 13. Extracted oblique slice images from measurement (left) and calculated (right) dose volume.

3.3.2 Registration Error Estimation

Essential factors affecting FLE and FRE are the image features of the fiducial markers in both image sets (OCT and CT images). In Figure 14, normalized profiles of the fiducial markers are presented for both image sets. Due to different attenuation of the light sources (a HeNe laser and 120 kV photon beam), the shape of the fiducial markers on the images was different. The higher contrast of the fiducials in the CT images leads to narrower beam profiles of the fiducials in the CT images than the OCT images. Most importantly, in both image sets, one pixel of the peak value represents the location of the fiducials. This critical feature results in submillimeter FLE and FRE.

Additionally, the prominence values of the fiducial and other points are shown in the histogram (Figure 15). The top two histograms comprise data from CT images and the two histograms at the bottom comprise data from OCT images. First, the prominence values of the fiducial markers on CT images are higher than what on OCT images. Moreover, prominence values at other pixels are much smaller than the fiducial pixels in both image sets, which leads to the negligible possibility of misdetection of the fiducial points. In CT images, prominence values are in the range of 0 to 500 at non-fiducial pixels and 8000 to 19000 at fiducial pixels. In OCT images, prominence values are in the range of 0 to 16 at non- fiducial pixels and 4150 to 4510 at fiducial pixels. From the analysis of 20 fiducial registrations, FRE was measured to be 0.62 mm and FLE was calculated to be 0.44 mm using equation (4). TRE in the 3D space can be estimated from FLE by using equation (5). Figure 16 shows the isovalue lines of TRE in the axial and coronal views. Due to symmetric configuration of the fiducial points, the results in coronal view are the same as those in sagittal view. In the region of measured dose distribution, which is usually at the center of the dosimeter, the estimated TRE is smaller than 0.3 mm. In addition, TRE was estimated by analyzing 10 fiducial markers, previously registered as targets. After registration, all of them are shown to be at the same

coordinates in the CT and OCT images. We were unable to measure submillimeter registration errors because the resolution limit of treatment planning exported dose images and CT images is 1 mm.
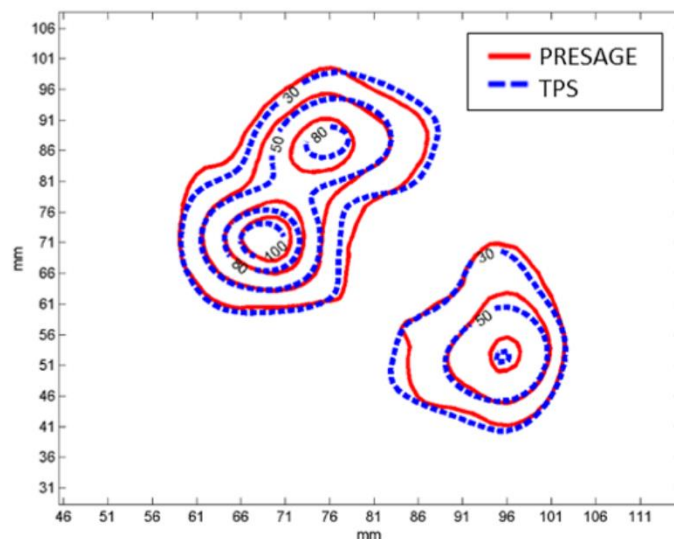
Figure 14. The measured (red) and TPS-calculated (blue) dose distribution comparison of the extracted oblique plane.
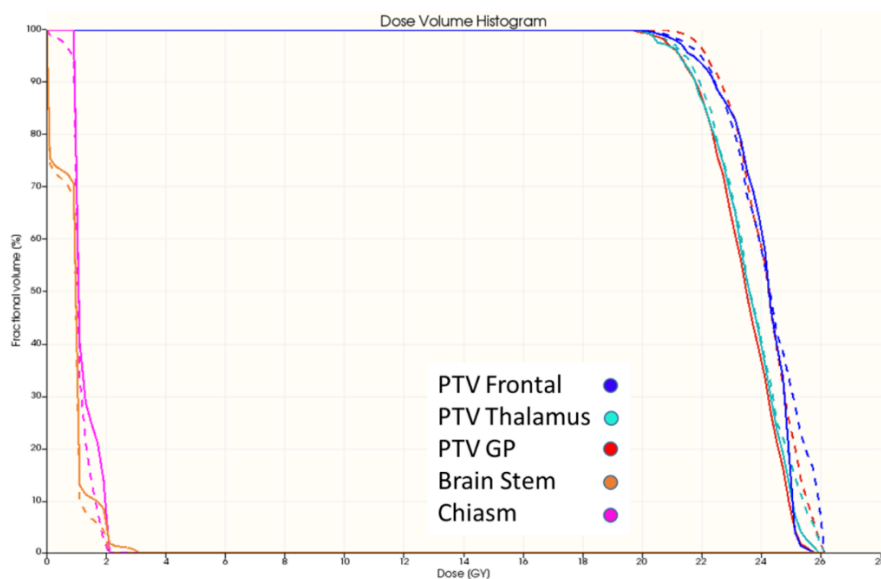
Figure 15. DVH comparison of the measurement (dashed line) and TPS-calculation (solid line) of the multi-lesions case.
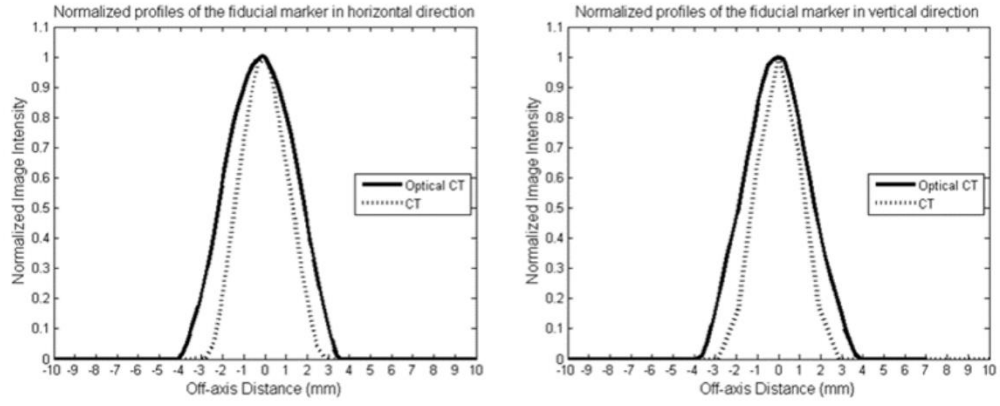
Figure 16. Normalized profiles of the fiducial markers on CT and OCT images in horizontal (left) and vertical (right) direction.
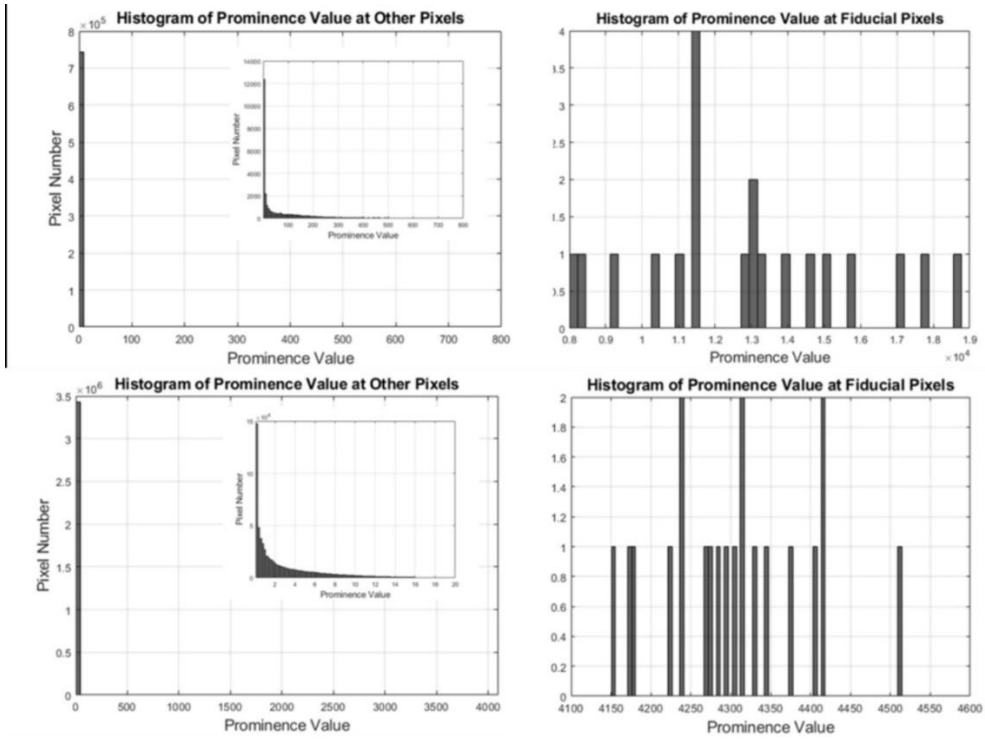
Figure 17. Prominence Values of the fiducial pixels (right) and other pixels (left) on CT (top) and OCT images (bottom).
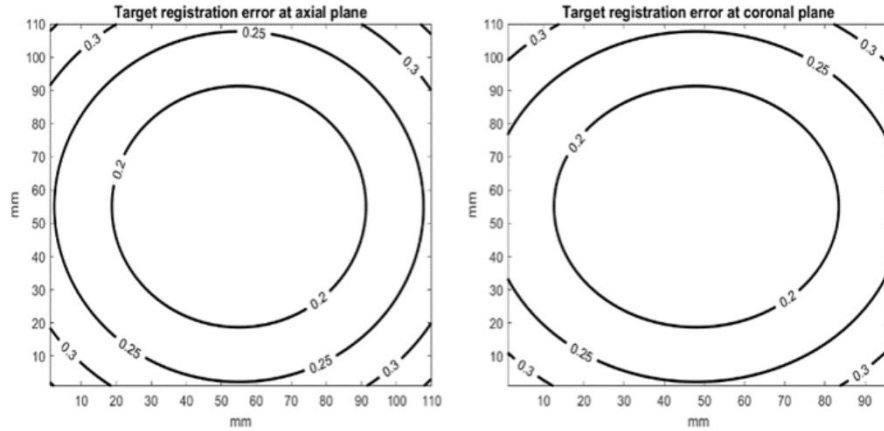
Figure 18. Estimated TRE shown in axial and coronal plane.

3.4 Discussion

A robust methodology of 3D IMRT QA using point-based registration and structure mapping was proposed in this study, which aims to improve the correlation between IMRT QA evaluation and the underlying planning and delivery errors. In previous publications[5-8], concerns were raised about 2D measurement-based IMRT QA using the gamma index. First of all, investigators presented situations where the conventional single field 2D dose distribution comparison using the gamma index was insensitive in detecting dose errors as well as specific delivery errors due to the relatively low resolution of the dosimeters, loose constraints or errors washed out in the composite dose images. Secondly, clinical acceptability does not correlate with the passing rate of the gamma index. The gamma failure points could be distributed throughout either the target or critical organs. To have a comprehensive view of an individual treatment plan, the IMRT QA method needs to have the capability of detecting small delivery errors as well as providing spatial information of the errors relative to the important structures. For the cases presented in this study, conventional 2D IMRT QA cannot provide failing points location relative to the structure but only evaluate the overall dose difference. In the first case, ArcCHECK (Sun Nuclear) shows average 97.4% passing

93

rate using 3%, 3 mm criteria. However, this study shows that most of the failing points are at the edge of PTV where dose gradient is high, which influences the PTV coverage. In the second case, although average passing rate using conventional 2D gamma (3%, 3 mm) is only 94.7%, this study shows that the dose coverage of all PTVs is preserved and most of the failing points are at the intermediate dose regions (50-70%) between the two close lesions.

The proposed method can be an effective tool for commissioning of novel treatment techniques, such as multiple lesions radiosurgery treatments. It has sufficient resolution and signal-to-noise ratio to detect small delivery errors. Besides, accurate point-based registration was employed to correlate the measurement coordinate system and planning coordinate system. Accurate registration of the planning and measurement systems enabled acquisition and translation of relevant structural information. Using the proposed method, clinical-relevant information such as DVH, 3D location of gamma failing points and 2D dose distribution in the high gradient region can be employed to make comprehensive clinical judgments.

The sensitivity and specificity of an IMRT QA method to detect planning or delivery errors relates to the uncertainties of the whole QA procedure. Therefore, the source and magnitude of the uncertainties should be estimated. More significant uncertainties than the errors to be detected could result in a high rate of false positives. The sources of uncertainties of the proposed IMRT QA method include fiducial registration, dose measurements, structures mapping and dosimeter setup. Using the pixel-to-pixel mapping of the Eclipse treatment planning system, the uncertainty from structure mapping is negligible. The dosimeter setup error relates to the laser error and operator error, which is similar to all the measurement-based IMRT QA methods. In this study, errors from fiducial registration was analyzed. FLE, FRE and TRE were estimated to be less than a millimeter. TRE of pixels in 3D space of the dosimeter was calculated to be smaller than 0.3

mm. The highest resolution of Eclipse treatment planning dose calculation is 1 mm. Therefore, the proposed fiducial markers and configuration can provide sufficient accuracy for dose comparison.

The PRESAGE dosimeter is accurate in terms of relative dose distribution measurement but is not ready for absolute dosimetry. The selection of the normalization point of the measured dose distribution could affect the interpretation of the results. In this study, the normalization point was chosen to be in a uniform high dose region. Moreover, there are differences between the inhomogeneity of the real patient and the dosimeter, and thus the magnitude of the discrepancy between the measurement and the calculation evaluated using the phantom could be different than the real discrepancy in the patients. This is the same as all the other measurement-based IMRT QA methods used routinely in clinical practice. To improve the correlation, phantom size and shape should be close to patient's geometry. As 3D printing becomes more common and low-cost, patient-specific phantom could be utilized for radiotherapy dosimetry[28].

This work has provided a clinically feasible methodology utilizing an automatic fiducial registration algorithm and commercially available structure-mapping application in clinical TPS, which is a step toward the implementation of a foolproof 3D dosimetric verification system with organ-specific dose information for routine clinical use. With the acquired information, organ-specific dose difference criterion could be implemented in the future. Moreover, our study adds on to the current methods for 3D dosimetric analysis by reporting the registration error as part of the dose comparison error. More convenient, user-independent and time-efficient optical scanners and programs are being developed at our lab so that 3D dosimetry can become clinically available and easily accessible in the future.

3.5 Conclusion

In this study, we introduced a robust methodology of 3D measurement-based IMRT QA for organ-specific dose comparison. With accurate point-based registration between measured and calculated image spaces, a precise spatial correlation between the two can be found. In addition, the patient's anatomical structures can be mapped to the CT images of the phantom using the coordinates of the fiducials. This work demonstrates two clinical cases and shows the capability of 3D organ-specific dose comparison. In addition, a comprehensive analysis of the registration uncertainties was performed. This work aims to improve the current 2D measurement based IMRT QA and shows the clinical feasibility of 3D dosimetry for future use.

References or Bibliography

1. Ezzell, G.A., Galvin, J.M., Low, D., Palta, J.R., Rosen, I., Sharpe, M.B., Xia, P., Xiao, Y., Xing, L. and Cedric, X.Y., 2003. Guidance document on delivery, treatment planning, and clinical implementation of IMRT: report of the IMRT Subcommittee of the AAPM Radiation Therapy Committee. Medical physics, 30(8), pp.2089-2115.

2. Ezzell, G.A., Burmeister, J.W., Dogan, N., LoSasso, T.J., Mechalakos, J.G., Mihailidis, D., Molineu, A., Palta, J.R., Ramsey, C.R., Salter, B.J. and Shi, J., 2009. IMRT commissioning: multiple institution planning and dosimetry comparisons, a report from AAPM Task Group 119. Medical physics, 36(11), pp.5359-5373.

3. Moran, J.M., Dempsey, M., Eisbruch, A., Fraass, B.A., Galvin, J.M., Ibbott, G.S. and Marks, L.B., 2011. Safety considerations for IMRT: executive summary. Medical physics, 38(9), pp.5067-5072.

4. Hartford, A.C., Galvin, J.M., Beyer, D.C., Eichler, T.J., Ibbott, G.S., Kavanagh, B., Schultz, C.J. and Rosenthal, S.A., 2012. American College of Radiology (ACR) and American Society for Radiation Oncology (ASTRO) practice guideline for intensity-modulated radiation therapy (IMRT). American journal of clinical oncology, 35(6), pp.612-617.

5. Pawlicki, T., Yoo, S., Court, L.E., McMillan, S.K., Rice, R.K., Russell, J.D., Pacyniak, J.M., Woo, M.K., Basran, P.S., Shoales, J. and Boyer, A.L., 2008. Moving from IMRT QA measurements toward independent computer calculations using control charts. Radiotherapy and Oncology, 89(3), pp.330-337.

6. Smith, J.C. and Dieterich, S., 2012. 2.2. It is STILL necessary to validate each individual IMRT treatment plan with dosimetric measurements before delivery. Controversies in Medical Physics: a Compendium of Point/Counterpoint Debates Volume 2, p.58.

7. Siochi, R.A.C., Molineu, A. and Orton, C.G., 2013. Patient-specific QA for IMRT should be performed using software rather than hardware methods: Point/Counterpoint. Med. Phys, 40, p.070601.

8. Kruse, J.J. and Mayo, C.S., 2013. Comment on "Catching errors with patient-specific pretreatment machine log file analysis". Practical radiation oncology, 3(2), pp.91-92.

9. Miften, M., Olch, A., Mihailidis, D., Moran, J., Pawlicki, T., Molineu, A., Li, H., Wijesooriya, K., Shi, J., Xia, P. and Papanikolaou, N., 2018. Tolerance limits and methodologies for IMRT measurement-based verification QA: recommendations of AAPM Task Group No. 218. Medical physics, 45(4), pp.e53-e83.

10. Kry, S.F., Glenn, M.C., Peterson, C.B., Branco, D., Mehrens, H., Steinmann, A. and Followill, D.S., 2019. Independent recalculation outperforms traditional measurement-based IMRT QA methods in detecting unacceptable plans. Medical physics, 46(8), pp.3700-3708.

11. Wuu, C.S. and Xu, Y., 2006. Three-dimensional dose verification for intensity modulated radiation therapy using optical CT based polymer gel dosimetry. Medical physics, 33(5), pp.1412-1419.

12. Oldham, M., Gluckman, G. and Kim, L., 2004. 3D verification of a prostate IMRT treatment by polymer gel-dosimetry and optical-CT scanning. In Journal of Physics: Conference Series (Vol. 3, No. 1, p. 293). IOP Publishing.

13. Oldham, M., Thomas, A., O'Daniel, J., Juang, T., Ibbott, G., Adamovics, J. and Kirkpatrick, J.P., 2012. A quality assurance method that utilizes 3D dosimetry and facilitates clinical interpretation. International Journal of Radiation Oncology* Biology* Physics, 84(2), pp.540-546.

14. Thomas, A., Niebanck, M., Juang, T., Wang, Z. and Oldham, M., 2013. A comprehensive investigation of the accuracy and reproducibility of a multitarget single isocenter VMAT radiosurgery technique. Medical physics, 40(12), p.121725.

15. Bache, S., Malcolm, J., Adamovics, J., & Oldham, M. (2016). Optical-CT 3D dosimetry using Fresnel lenses with minimal refractive-index matching fluid. PloS one, 11(3)

16. Jackson, J., Juang, T., Adamovics, J. and Oldham, M., 2015. An investigation of PRESAGE® 3D dosimetry for IMRT and VMAT radiation therapy treatment verification. Physics in Medicine & Biology, 60(6), p.2217.

17. Vandecasteele, J., & De Deene, Y. 2013. Evaluation of radiochromic gel dosimetry and polymer gel dosimetry in a clinical dose verification. Physics in Medicine & Biology, 58(18), 6241.

18. Juang, T., 2015. Clinical and Research Applications of 3D Dosimetry. Durham, North Carolina, USA: Duke University.

19. De Deene, Y. 2002. Gel dosimetry for the dose verification of intensity modulated radiotherapy treatments. Zeitschrift für medizinische Physik, 12(2), 77-88

20. Schreiner, L. J. 2015. True 3D chemical dosimetry (gels, plastics): Development and clinical role. In Journal of Physics: Conference Series (Vol. 573, No. 1, p. 012003). IOP Publishing.

21. Doran, S., Al-Nowais, S., Krstajić, N., Adamovics, J., Kacperek, A., & Brunt, J. 2006. True-3D scans using PRESAGETM and Optical-CT: A case study in proton therapy. In Journal of Physics: Conference Series (Vol. 56, No. 1, p. 231). IOP Publishing.

22. Babic, S., Battista, J., & Jordan, K. 2008. Three-dimensional dose verification for intensity-modulated radiation therapy in the radiological physics centre head-and-neck phantom using optical computed tomography scans of ferrous xylenol–orange gel dosimeters. International Journal of Radiation Oncology* Biology* Physics, 70(4), 1281-1291.

23. Baldock, C., De Deene, Y., Doran, S., Ibbott, G., Jirasek, A., Lepage, M., ... & Schreiner, L. J. (2010). Polymer gel dosimetry. Physics in Medicine & Biology, 55(5), R1.

24. Umeyama, S., 1991. Least-squares estimation of transformation parameters between two point patterns. IEEE Transactions on Pattern Analysis & Machine Intelligence, (4), pp.376-380.

25. West, J.B., Fitzpatrick, J.M., Toms, S.A., Maurer Jr, C.R. and Maciunas, R.J., 2001. Fiducial point placement and the accuracy of point-based, rigid body registration. Neurosurgery, 48(4), pp.810-817.

26. Fitzpatrick, J.M., West, J.B. and Maurer, C.R., 1998. Predicting error in rigid-body point-based registration. IEEE transactions on medical imaging, 17(5), pp.694-702.

27. Fitzpatrick, J.M., West, J.B. and Maurer, C.R., 1998. Predicting error in rigid-body point-based registration. IEEE transactions on medical imaging, 17(5), pp.694-702.

28. EHLER, Eric D., et al. Patient specific 3D printed phantom for IMRT quality assurance. Physics in Medicine & Biology, 2014, 59.19: 5763.

Chapter 4

An End-to-End Approach to the Characterization of a

Stereotactic Radiosurgery Platform Using

Anthropomorphic 3D Dosimetry System

4.1 Introduction

Single-fraction stereotactic radiosurgery (SRS)[1-3] is a highly effective irradiation strategy for various intracranial metastases. With advancements in systematic management of primary tumors, SRS has gained widespread popularity in Radiation Oncology clinics, employing linear accelerators[4-6] and the volumetric modulated arc therapy (VMAT) technique. In comparison to the Gamma Knife radiosurgery platform, VMAT offers a significant advantage in terms of faster treatment delivery to multiple targets, utilizing a single isocenter by modulating multileaf collimators (MLC), gantry, and collimator rotation. Moreover, VMAT can be implemented in clinics without the need for a Gamma Knife installation[7-9].

A comprehensive evaluation of the linear accelerator[10, 11] performance is crucial to ensure minimal risk of compromised coverage and tissue toxicity, particularly given the 1-3 mm PTV margin. Publication have shown that the risk of compromised coverage increases with decreasing target volume, increasing rotational error and increasing distance from the isocenter. The other crucial components of SRS are its rapid dose falloff into the surrounding normal tissues, which could be quantified by the dose gradient index (DGI)[12, 13]. Rapid dose falloff permits minimal risk of brain radiatioin necrosis, the most significant late complication after cranial SRS. Many studies have correlated risk of necrosis to the volume of normal tissue irradiated at, or greater than, a specific dose. For instance, the risk of radionecrosits for V10 and V12 volume smaller than 2.2 cm3 and 1.6 cm3 was 4.7%, for 2.2 cm^3 - 6.3 cm^3 and 1.6 – 4.7 cm^3 was 11.9%[14-16]. For this reason, the dosimetric accuracy of the intermediate-to-low dose spillage in the treatment planning system, involving modeling of small fields, out-of-field dose, and MLC characteristics should be verified prior to clinical use.

Despite many advances in the SRS planning and delivery system, measurement quality assurance (QA) remains a challenge because of the debatable and unclear action levels. The main reason of the challenge is that the gamma passing rate, viewed as an index for delivered and measured dose comparison, is not a clinically relevant metric. Additionally, studies have shown a 3-mm shift was undetected by gamma analysis using 3%/1-3 mm criteria, which could result in loss of target coverage[17, 18]. Unlike planar gamma testing, utilizing 3D dose comparison with plan quality metrics has the potential to directly predict the clinical impact. However, there are challenges in establishing a standardized methodology, and currently, there is a lack of adequate tools for conducting end-to-end testing of single isocenter multi-target treatments. End-to-end testing, which focuses on testing an integrated system from the beginning to the end, can significantly enhance confidence in all aspects of the procedure while reducing costs and time. Unfortunately, more attention has been given to equipment-specific quality assurance (QA), overshadowing the importance of comprehensive end-to-end testing. This limited focus hampers our understanding of overall treatment uncertainties and neglects experimental verification of complex treatment modalities.

This study has two main objectives. Firstly, we aim to introduce a highly accurate and comprehensive end-to-end 3D dosimetry system capable of measuring DGI, V10, V12, as well as rotational and translational errors in the delivery of multitarget treatments in 3D space. This capability has not been previously demonstrated in published literature. Secondly, we assess and compare measured metrics from seven benchmark plans with various treatment geometries to enhance our understanding of overall delivery uncertainties and increase confidence in SRS treatments.

To achieve the first goal, we present an easy-to-use 3D Anthropomorphic dosimetry system with submillimeter accuracy for dosimetric and mechanical verification of SRS treatments. Previous studies[19, 20] have explored the application of the PRESAGE/optical 3D dosimetry system for IMRT and VMAT QA, respectively. However, these studies only compared 2D dose maps and profiles, and measurement accuracy was affected by artifacts from refraction, reflection, and impurities. In our study, we implemented a novel angular-sorted background subtraction method to mitigate these artifacts and customized the sensitivity of the PRESAGE phantom to accurately measure high dose radiation from SRS treatments. Additionally, we utilized a fiducial registration technique to detect sub-millimeter rotational and translational errors during SRS treatments.

The second focus of this study was to investigate the feasibility of characterizing a radiosurgery platform in a standardized manner using seven benchmark plans categorized into three modules. These modules address different aspects of machine delivery and modeling errors, as well as various types and complexities of SRS treatments. In 2009, TG-119 by the American Association of Physicists in Medicine[21] was published for verifying the commissioning and planning of intensity-modulated radiation therapy (IMRT) systems. However, those tests were not suitable for verifying SRS treatment platforms. In recent years, there has been a growing need for standardized SRS test cases similar to the original need for IMRT. Our study presents the first measured plan quality metrics and 3D rotational and translational errors for multitarget treatments using pre-defined target geometries in the test plans. Overall, this study introduces a high-fidelity end-to-end 3D dosimetry system and explores the standardized characterization of a radiosurgery platform, providing valuable insights into the dosimetric and mechanical aspects of SRS treatments.

This study aims to address the existing knowledge gap regarding the mechanical and dosimetric uncertainties associated with radiosurgery treatments. Additionally, the research further supports

the significance of conducting 3D end-to-end testing in the field. The proposed 3D dosimetry system holds potential for various applications, such as the commissioning of new radiosurgery platforms. It can also facilitate remote multi-institutional audits of radiosurgery treatments, enabling comprehensive evaluations across different healthcare facilities. Moreover, the system can serve as a remote commissioning service for developing countries, where access to dosimetry equipment and human resources may be limited.

4.2 Materials and Methods

4.2.1 The Development of an Integrated Anthropomorphic 3D Dosimetry System

The developed anthropomorphic 3D dosimetry system consists of a modified Stereotactic End-to-End Verification (STEEV) inhomogeneous phantom[22] (CIRS, Norfolk, VA) with a customized tissue-equivalent insert to integrate 3D dosimeters, 3D dosimeters, PRESAGE[23] (Heuris Pharma LLC, Skillman, NJ), and an in-house fast optical CT scanner utilizing fiber optic taper for the readout of 3D dose maps. In addition to the hardware components, an in-house developed Labview program for automatic optical scanning, and Matlab codes for image preprocessing, parallel beam filtered back projection (FBP) image reconstruction, angular-sorted background subtraction and dosimetric analysis. SlicerRT, an extension of 3D Slicer was adopted for 3D dose visualization, gamma test calculation and the analysis of plan quality metrics. The detailes of phantom construction, 3D dose acquisition, reconstruction techniques and the methodology of end-to-end verification are shown below.

4.2.1.1 An Anthropomorphic Phantom for 3D Dosimetry

Steev anthropomorphic phantom micmics patient's head and neck anatomy with the tissue- and bone-equivalent structures and accommodates a variety of interchangeable tissue equivalent inserts suitable for various dosimeters. In collaboration with CIRS, a fixed and movable tissue-

equivalent insert was customized to integrate a cylinder-shaped 3D dosimeter, PRESAGE (6 cm diameter, 6 cm height) with the Steev phantom (Figure 1). The homogeneity of Hounsfield Units (HU) values and the air gaps between each inserted component were verified using simulator CT scanning (SOMATOM Definition AS, Siemens Healthineers, Forchheim, Germany).
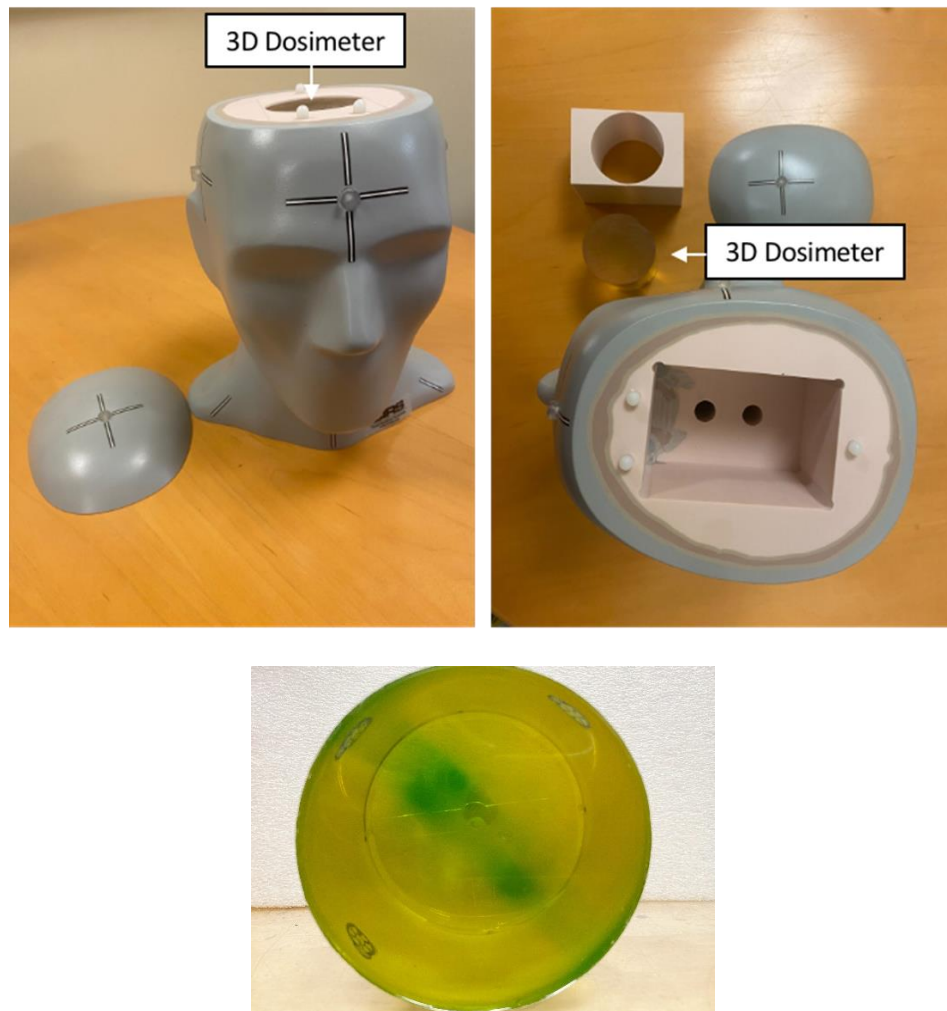
Figure 19. Photographs of the stereotactic end-to-end verification phantom, customized tissue-equivalent insert for a cylinder-shaped 3D dosimeter, and the PRESAGE 3D dosimeter.

4.2.1.2 3D Dosimeters for SRS Dose Verification

The sensitivity of 3D radiochromic dosimeters plays a crucial role in achieving optimal 3D dose measurements. It is important to find a balance between signal sensitivity and noise levels to ensure

accurate results. High sensitivity dosimeters can lead to signal saturation, which may affect the reliability of measurements. In the case of SRS plan measurements, the dose range typically varies from 1 Gy to 20 Gy. For SRS measurements, the main material of PRESAGE is polyurethane, which consists of 61% carbon, 20% oxygen, 10% nitrogen, and 9% hydrogen. It has an effective atomic number of 6.6 and a density of 1.05 g/cm3. In addition, PRESAGE dosimeters are made up of leucomalachite green (LMG) dye and a halocarbon radical initiator. The free radicals created from halocarbon radiolysis and oxidization during radiation interaction change the LMG into malachite green (MG) which has a maximum absorbance at 633 nm which is detected by the OCT scanner. The formulation is cured at room temperature by pouring it into molds with a diameter of 5.9 cm. The dosimeters are then placed in a pressurized tank at 60 psi for a minimum of 24 hours to facilitate proper curing. To verify the linear response of the dosimeter and its ability to handle doses up to 25 Gy, four 2 cm square photon fields with varying dose levels are delivered to the 3D dosimeter. This approach allows for the acquisition of net optical densities at eight different dose levels, measured at various depths within the dosimeter. The linearity of the dose response curve is evaluated, along with an assessment of the signal-to-noise ratio at each dose level to ensure reliable and accurate measurements.

4.2.1.3 Treatment Planning and Treatment Delivery

The anthropomorphic phantom with a 3D dosimeter inserted was CT-scanned using Siemnes Somatom Definition AS with slice resolution of 1 mm. SRS benchmark plans on the CT images were generated using HyperArc treatment planning system (Varian Medical System, Palo Alto, CA). The treatment fields consist of one full arc and three half arcs with 45, 315, 270 degree couch angles. The isocenter location and collimator rotation were optimized during treatment planning. The planning 3D dose matrices and structure sets were exported from the treatment planning

system for the comparison with measured 3D dose matrices. The treatment plans were then delivered to the phantom using a TrueBeam linear accelerator. The goal is to simulate a real patient's treatment from the CT simulation to treatment delivery and record the treatment uncertainties using the 3D dosimeter inside the phantom.

4.2.1.4 Optical Scanning and Angular-sorted Background Subtraction

An in-house broad-beam optical CT scanner with a fiber optic taper was used for the 3D dose readout of the 3D dosimeters under U.S. patent application entitled "Three-Dimensional Dosimetry Procedures, Methods and Devices, and Optical CT Scanner Apparatus Which Utilizes Fiber Optic Taper for Collimated Images[24]". The in-house optical CT scanner consists of four components, an LED light illuminator, an aquarium with a rotation stage and matching liquid inside, a fiber optic taper, and a fiber-coupled CCD detector. An optic fiber taper with the taper ratio of 3:1 was mounted to the exit window of the water tank for light collection, transfer, and demagnification. The smaller end of the optic fiber taper is connected to fiber optic window, bonded to a CCD camera (Allied Vision, Houston, Tx). An LED illuminator provides uniform and parallel red light with a peak wavelength of 625 nm and 20 nm FWHM. The 2D projection images were acquired using a 16 bit monochrome CCD camera from Allied Vision with 4008 x 2672 active pixels. Each dosimeter scan consisted of 360 2D projection images, acquired at angular increment of 1 degree. Background subtraction plays a critical role in 3D dosimetry as it helps correct noise arising from various sources such as light reflection and refraction, ring artifacts due to impurities in the optical system and dosimeters. However, it is essential to ensure that the dosimeter is scanned in the same position in the scanner as the background scan after irradiation. Mismatches between the two scans can introduce additional noise into the data. The proposed method, angular-sorted background subtraction, addresses this issue by utilizing a data reordering

technique. It leverages the fiducial marker present on the dosimeter to reorder the 360 2D projection images before image reconstruction. This reordering process ensures that the pre-irradiation background scan and the measurement scan are properly aligned, eliminating any mismatches. By aligning the scans accurately, the angular-sorted background subtraction technique effectively reduces noise caused by scan position discrepancies, enhancing the accuracy of the 3D dosimetry measurements.

4.2.1.5 3D Dose Reconstruction and Analysis

An in-house developed Matlab script was used for image processing and 3D dose reconstruction. The 2D projection images were rescaled to 1 mm resolution, to match the finest resolution in HyperArc treatment planning system. 360 projection images were converted to the sinogram domain and the sinograms were reconstructed using filtered back projection algorithm with parallel-beam geometry. Slicer RT, an open-source radiation therapy research toolkit for 3D Slicer, was implemented for the visualization of CT images, structure sets, measured dose matrix and planned dose matrix, the calculation of dose volume histogram (DVH), gamma test passing rates, plan quality metrics and the analysis of mechanical uncertainties. The previously published DGI[12], defined in equation 1 and 2, were used for this study

$$DGI = 100 - \left\{ 100 \cdot \left(\left(R_{eff,50\%Rx} - R_{eff,Rx} \right) - 0.3 \right) \right\} \qquad (1)$$

$$R_{eff} = \sqrt[3]{\frac{3V}{4\pi}} \qquad (2)$$

4.2.2 Dosimetric Verification Using EBT3 radiochromic film

CIRS film stack insert was used to measure multiple coronal planar doses in order to verify the measurement from the 3D dosimeter at certain slices. The film stack insert is a cube with tissue-equivalent material. It can accommodate 13 layers of radiochromic film with 4 mm thick spacers

in bewteen each film. The average HU of the film stack and the 3D dosimeter in CT images are 52 (SD 16) and 146 (SD 8). Higher standard deviation of the film stack is due to the presence of EBT3 radiochromic film. A 2-target SRS plan was delivered to both the 3D and film dosimeters in the Steev anthropomorphic phantom, as shown in Figure 2. To compare the dose distribution, 2D gamma test and isodose line comparison were employed.
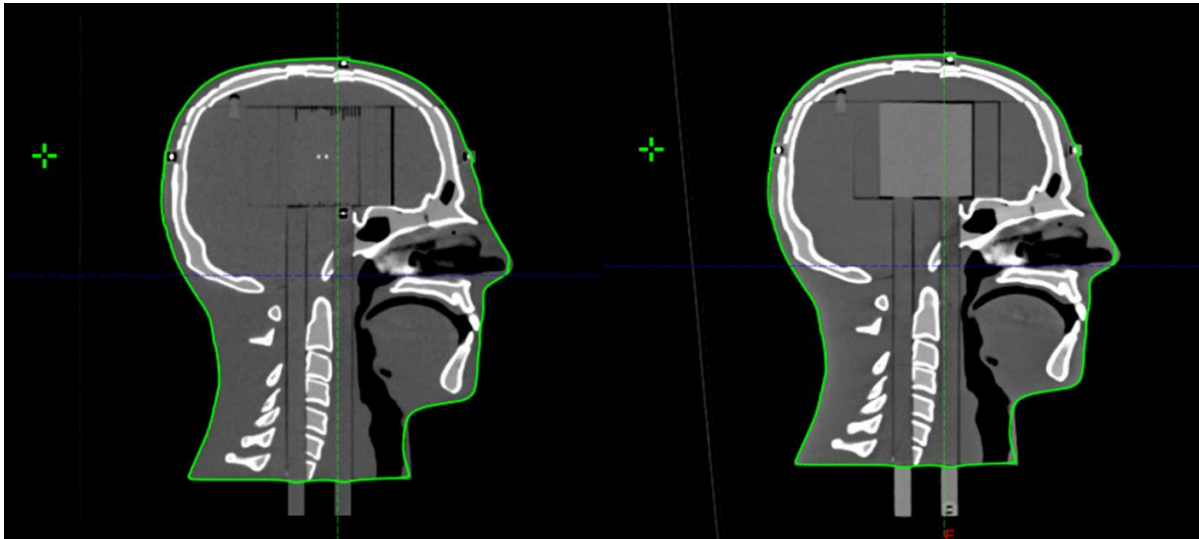
Figure 20. CT images of the stereotactic end-to-end verification phantom with the film stack inserted (left), and the 3D dosimeter inserted (right).

4.2.3 SRS Benchmark Plans for End-to-end Verification

The developed tool enables comprehensive end-to-end testing of all essential steps involved in a patient's treatment process. In order to characterize a radiosurgery system, seven benchmark plans with prescription dose of 18 Gy were designed to investigate specific aspects including off-axis errors, intermediate-to-low dose spillage, small field dosimetry, and multiple-target delivery (Figure 3). For the benchmark plans, the HyperArc system developed by Varian Medical Systems was utilized for automated treatment optimization and dose delivery in non-coplanar, MLC-based stereotactic radiotherapy. The TrueBeam system from Varian Medical Systems was used to deliver the plans, consisting of one full arc and three non-coplanar half arcs. The first module of the

benchmark plans aimed to assess off-axis mechanical and dosimetric errors. Two plans were designed with a single target at different off-axis distances, 0 cm and 7 cm as shown in (1) and (2) of Figure 3. Three fiducials were placed on the 3D dosimeter to facilitate set-up triangulation and registration between the planning dose images from the treatment planning system (TPS) and the measured dose images from the optical CT scanner. Cone-beam CT (CBCT) imaging was employed to minimize set-up uncertainties during dose delivery on the phantom. The results obtained provide valuable insights into mechanical dose delivery errors in an end-to-end context using varying off-axis distances. The second module comprised three SRS plans with two targets positioned at different distances from each other, specifically 6 mm, 12 mm, and 28 mm as illustrated in (3)-(5) of Figure 3. This module further evaluated the modeling of intermediate-to-low dose spillage between the two targets, which involves considering out-of-field dose and multileaf collimator characteristics. The potential risk of neurocognitive effects for patients arises from the intermediate-to-low dose spillage into normal brain tissue. The measured results were evaluated using planning metrics including DGI, V10, V12, and compared with the metrics obtained from the calculated dose distribution. The third module focused on the superposition of dose spillage from multiple targets. Two treatment plans were measured for (6) and (7) of Figure 3, one with five treatment targets and the other with ten. Similar to the previous module, planning metrics from the measured and calculated dose distributions were compared. Through the implementation of these benchmark plans, the study provides valuable information on various

110

aspects of the radiosurgery system, including mechanical and dosimetric errors, dose spillage modeling, and the impact of multiple targets.
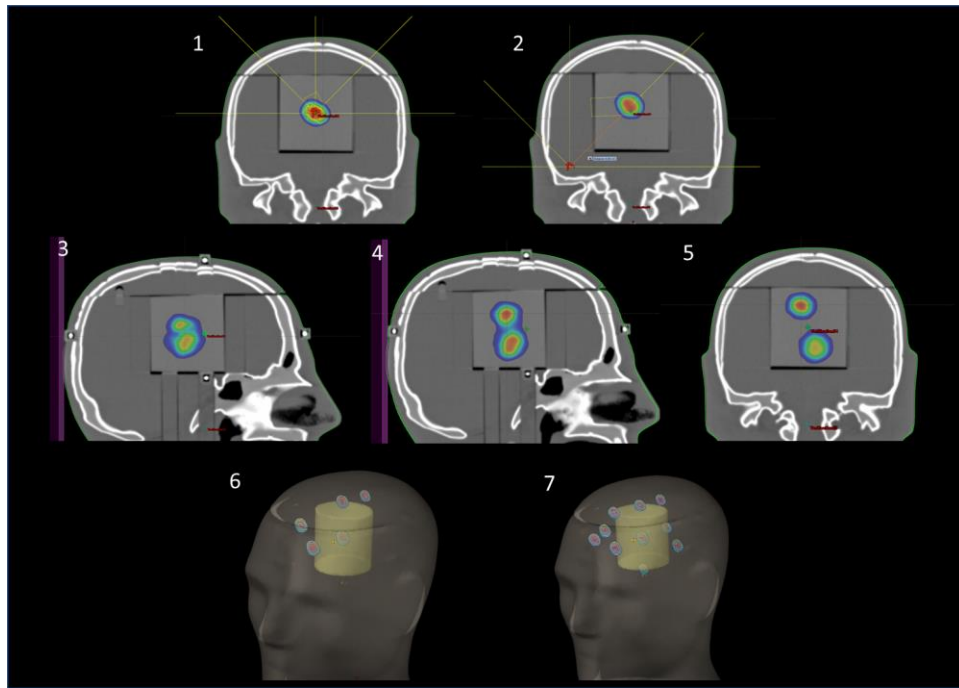
Figure 21. Seven benchmark plans for end-to-end SRS platform testing, encompassing (1) 1 target at 0 cm off-axis distance, (2) 1 target at 7 cm off-axis, (3) 2 targets with 6 mm separation, (4) 2 targets with 12 mm separation, (5) 2 targets with 28 mm separation, (6) 5 targets, and (7) 10 targets.

4.3 Results

4.3.1 Calibration of 3D Dosimeters for SRS Dose Verification

Figure 4 illustrates the linearity of the measured optical density in relation to the delivered dose. The left plot demonstrates the results obtained when employing dark field subtraction, which is a crucial step for accurate high dose measurements. In contrast, the right plot displays the results without dark field subtraction. The significance of dark field subtraction becomes evident when comparing the two plots. With dark field subtraction, the measured optical density exhibits a consistent and linear relationship with the delivered dose. The mean absolute percentage error

(MAPE) remains consistently low, with a value of 0.31% for dose levels up to 25 Gy. This indicates that the measured optical densities align closely with the expected linear relationship throughout the dose range. Conversely, without dark field subtraction, the measured optical densities deviate from the expected linear relationship, particularly in the high dose region where the dark field is significant compared to the measured signals. The percentage errors significantly increase as the dose levels rise. For instance, at 15 Gy, the percentage error reaches 1.3%, and it further increases to 6.8%, 10.6%, and 20.1% at 18 Gy, 20 Gy, and 25 Gy, respectively. This discrepancy highlights the importance of dark field subtraction for maintaining linearity and accuracy in high dose measurements. Furthermore, as the delivered dose increases, the relative standard deviation decreases due to the larger optical densities observed. The estimated scale of statistical noise is approximately 10 cGy. It is noteworthy that the relative standard deviation remains consistently below 2% for doses larger than 6 Gy, indicating good measurement precision within this dose range.
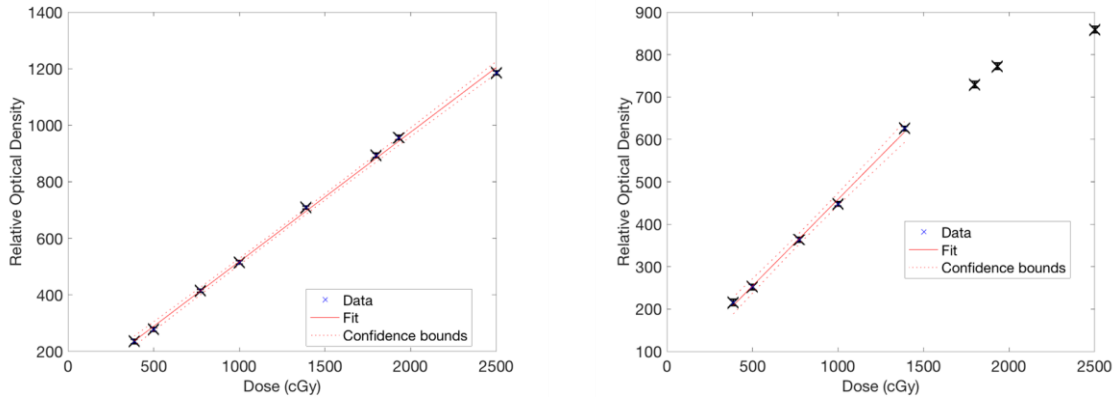
Figure 22. Linearity of measured optical density to dose in the dose range of 0-25 Gy, comparing results with (left) and without (right) dark field subtraction.

4.3.2 Angular-sorted Background Subtraction

To evaluate the impact of angular-sorted background subtraction on the quality of reconstructed dose images, an analysis was conducted involving two background scans. During each scan, the dosimeter was deliberately taken out of the tank and then carefully repositioned to replicate real measurement conditions. The reconstructed images resulting from the two repeat scans, along with the subtraction outcome, are presented in Figure 5. It is noteworthy that the structural artifacts observed in both scans should ideally be effectively eliminated through the subtraction process. Figure 6 provides valuable insights through line profiles of the two background scans, indicating consistent peak locations across the scans. After performing the subtraction, a substantial reduction of 77% was observed in the standard deviation of the background scan. However, it is important to acknowledge that some residual noise may persist, potentially attributed to random noise.
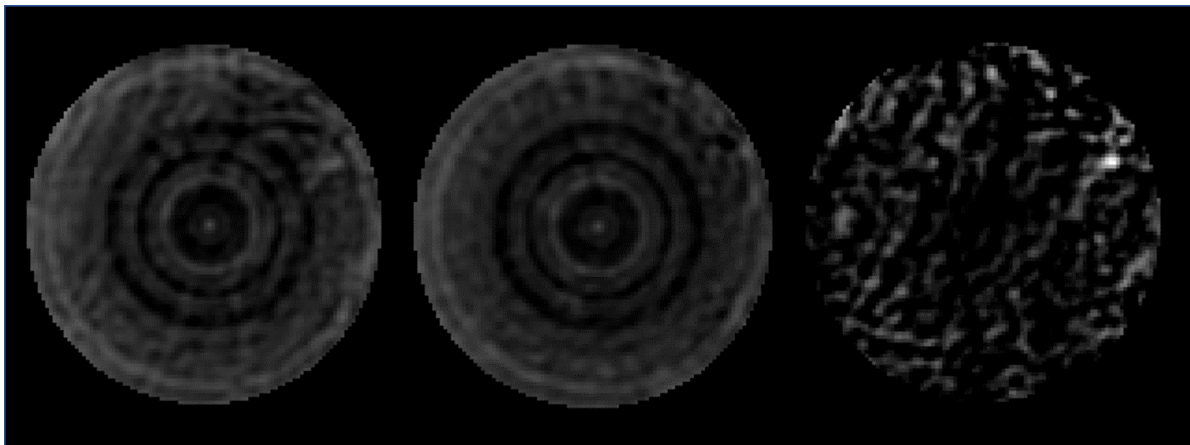
Figure 5. Reconstructed images of the two repeat background scans (left, middle) and the subtraction image obtained by subtracting the two scans (right).
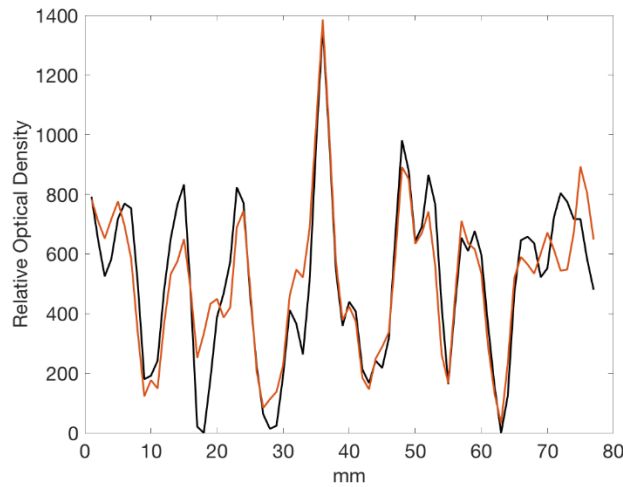
Figure 6. Line profiles across the two repeat background scans.

4.3.3 Dosimetric Verification Using EBT3 radiochromic film

The accuracy of the developed 3D dosimetry system was assessed by comparing two 2D dose planes, extracted from the measured 3D dose distribution, with film measurements. The results of this comparison are presented in Figure 7, which illustrates the agreement of isodose lines between the two dosimeters. Isodose lines representing 30%, 50%, 80%, 95%, and 105% of the prescription dose were plotted for visual comparison.

To provide a quantitative evaluation, a gamma comparison was conducted using criteria of 3% dose difference and 2 mm distance-to-agreement. The passing rates were determined to be 99.9% and 99.6% respectively, indicating a high level of agreement between the two dosimeters. These results further support the accuracy and reliability of the 3D dosimetry system.

114

Figure 8 provides additional insights through histograms displaying the relative dose difference for the two evaluated dose planes. The mean (standard deviation) of the relative dose difference between the film and 3D dosimeter measurements were calculated to be -1% (with a standard deviation of 2.2%) and -1.5% (with a standard deviation of 2.2%) respectively. These values fall well within the measurement uncertainty of the two dosimeters, further confirming the consistency and reliability of the 3D dosimetry system.
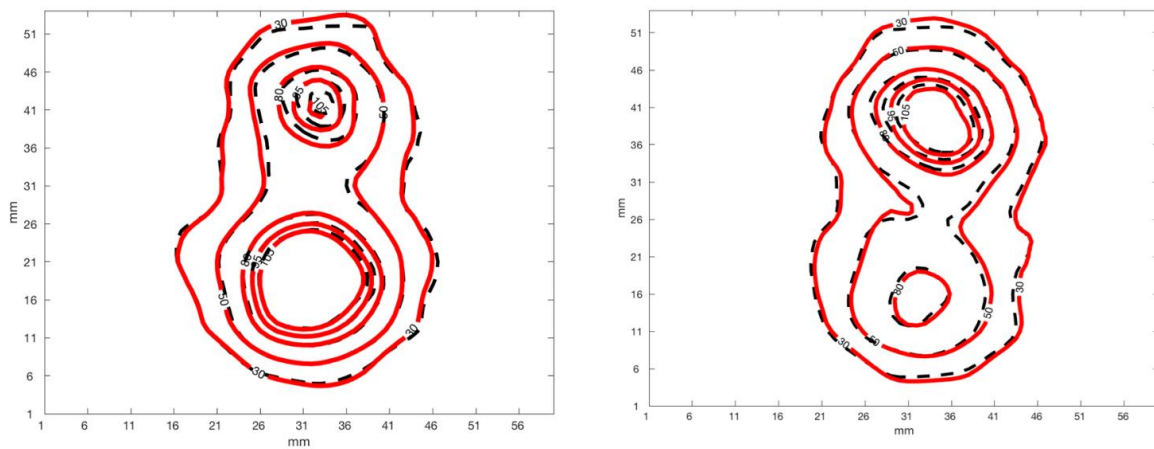
Figure 7. Comparison of isodose lines between the EBT3 film (black) and 3D dosimeter (red).
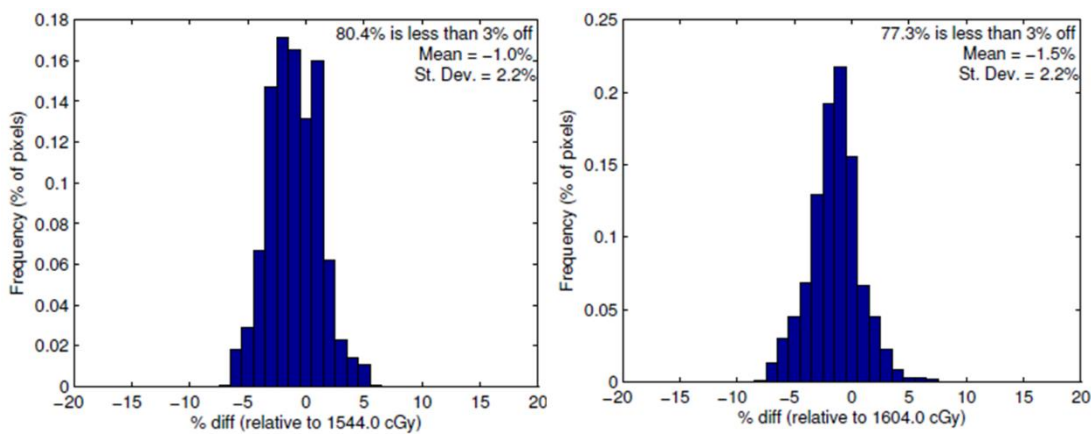
Figure 8. Histograms displaying the relative dose difference between 3D dosimeter and EBT3 film for the two evaluated dose planes.

4.3.4 SRS Benchmark Plans for End-to-end Verification

The first module of the study aimed to investigate off-axis mechanical and dosimetric errors using the developed 3D dosimetry system. Two treatment plans were examined, with a single target positioned at the isocenter and 7 cm away from the isocenter,extending from the center of the target to the isocenter. Measurements were performed using the 3D dosimetry system, and the obtained 3D isodose surfaces were compared with the corresponding treatment planning system (TPS) data for both plans. Figure 9 displays the comparison of the 3D isodose surfaces at 18 Gy, 12 Gy, and 9 Gy, respectively,between the measurements and the TPS for the two plans. For the plan with the target positioned at the isocenter, the isodose surfaces obtained from the measurements closely matched those from the TPS, with a deviation of less than 1 mm. However, for the plan with the target positioned 7 cm away from the isocenter, the deviation in the isodose surfaces between the measurements and the TPS increased, reaching up to 1.5 mm, as depicted in Figure 10. This suggests the presence of larger discrepancies in the dose distribution for off-axis targets.

To further evaluate the dosimetric comparison, gamma tests were performed using different criteria: 3%/3 mm, 3%/2 mm, and 2%/2 mm. For the plan with the target at the isocenter, the passing rates for all criteria were 100%, indicating excellent agreement between the measured and calculated dose distributions. For the plan with the target positioned 7 cm away from the isocenter, the passing rates decreased slightly. The passing rates were 100% for the 3%/3 mm criteria, 99.6% for the 3%/2 mm criteria, and 98.6% for the 2%/2 mm criteria. These results suggest that the

dosimetric agreement between the measurements and the TPS is slightly lower for the off-axis target plan compared to the plan at the isocenter.
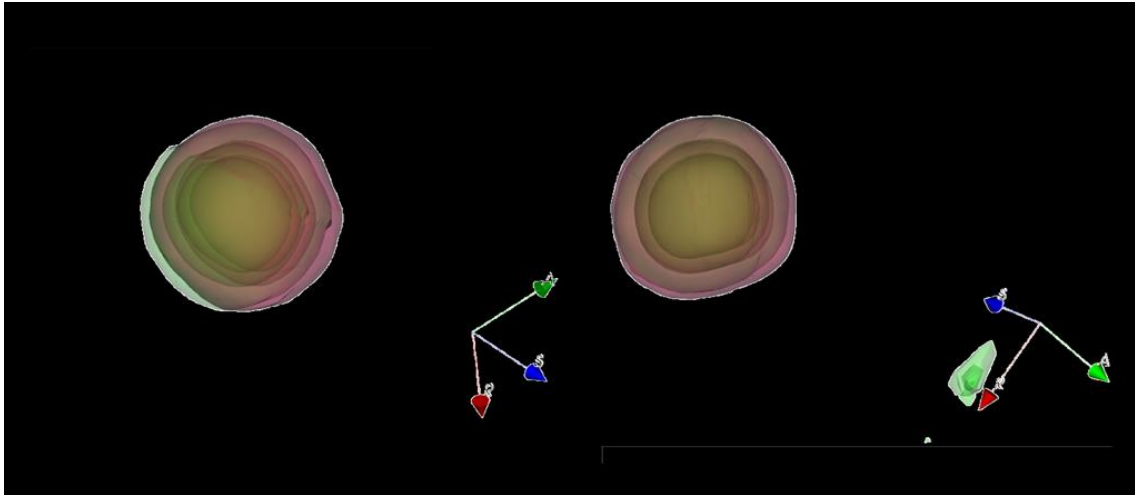
Figure 9. 3D isodose surface (18 Gy, 12 Gy, 9 Gy) comparison between the 3D dosimeter (red) and TPS (green) for the target at the isocenter (right) and 7 cm away from the isocenter (left)
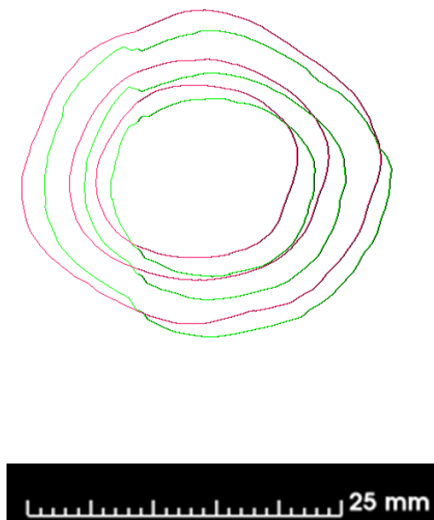
Figure 10. 2D isodose lines (18 Gy, 12 Gy, 9 Gy) comparison between the 3D dosimeter (red) and TPS (green) for the target at 7 cm away from the isocenter.

In the second module of the study, the main objective was to perform end-to-end testing of three SRS plans with two targets positioned at different distances from each other: 6 mm, 12 mm, and 28 mm, measured as the closest separation between the edges of the two targets. Figure 11 presents the 2D dose images on transverse, coronal, and sagittal planes for the treatment plan with a target separation of 12 mm, allowing for a visual comparison between the 3D measurements and the corresponding TPS calculations. In Figure 12, the isodose surface comparison and gamma maps are displayed. It is noticeable that the measured dose is higher than the calculated dose in the vicinity of the two closely spaced targets. In the plan with a 6 mm target separation, there are gamma failing points in this region, resulting in measured gamma passing rates of 99%, 98%, and 96% for the 3%/3mm, 3%/2mm, and 2%/2mm criteria, respectively. Similarly, in the plan with a 12 mm target separation, more gamma failing points are present between the two targets. The measured gamma passing rates for this plan are 97.1%, 96%, and 94.3% using the 3%/3mm, 3%/2mm, and 2%/2mm criteria, respectively. On the other hand, for the plan with a 28 mm target separation, the measured and calculated dose distributions demonstrate good agreement, with passing rates of 100%, 100%, and 97.3% using the 3%/3mm, 3%/2mm, and 2%/2mm criteria, respectively. In addition to the gamma tests, the study compared the DGI, V10, and V12 metrics obtained from the measurements and TPS calculations, as presented in Table 1. When the target separation is 28 mm, the measured metrics align well with the calculated values. However, for the other two plans, lower DGI values and higher V10 and V12 values were observed in the measurements compared to the TPS calculations. The largest discrepancies were observed in the

plan with a target separation of 12 mm, with a measured DGI that is 8.9 lower than the calculation,

and measured V10 and V12 values that are 1.38 and 1.31 higher than the calculation, respectively.
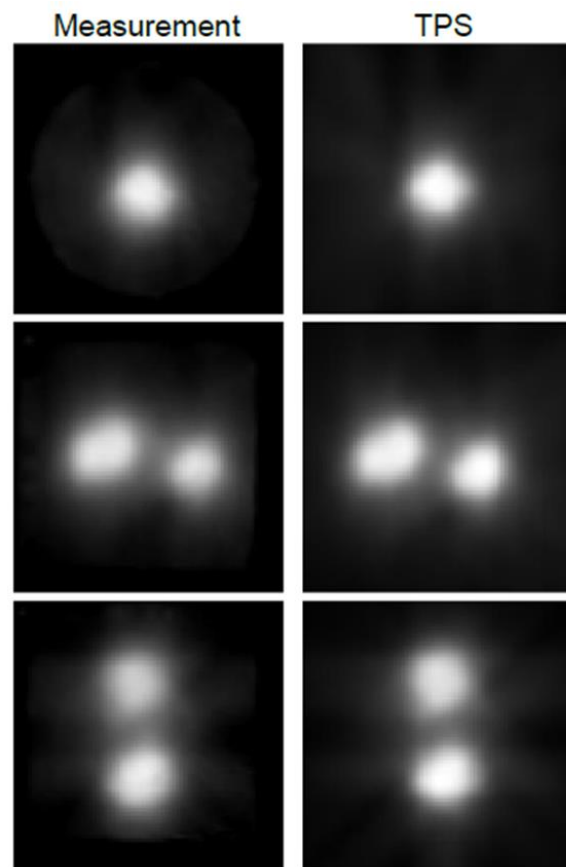
Figure 11. 2D dose images on transverse, coronal, and sagittal planes from the 3D dosimeter (left) and TPS (right) for the treatment plan with a target separation of 12 mm.
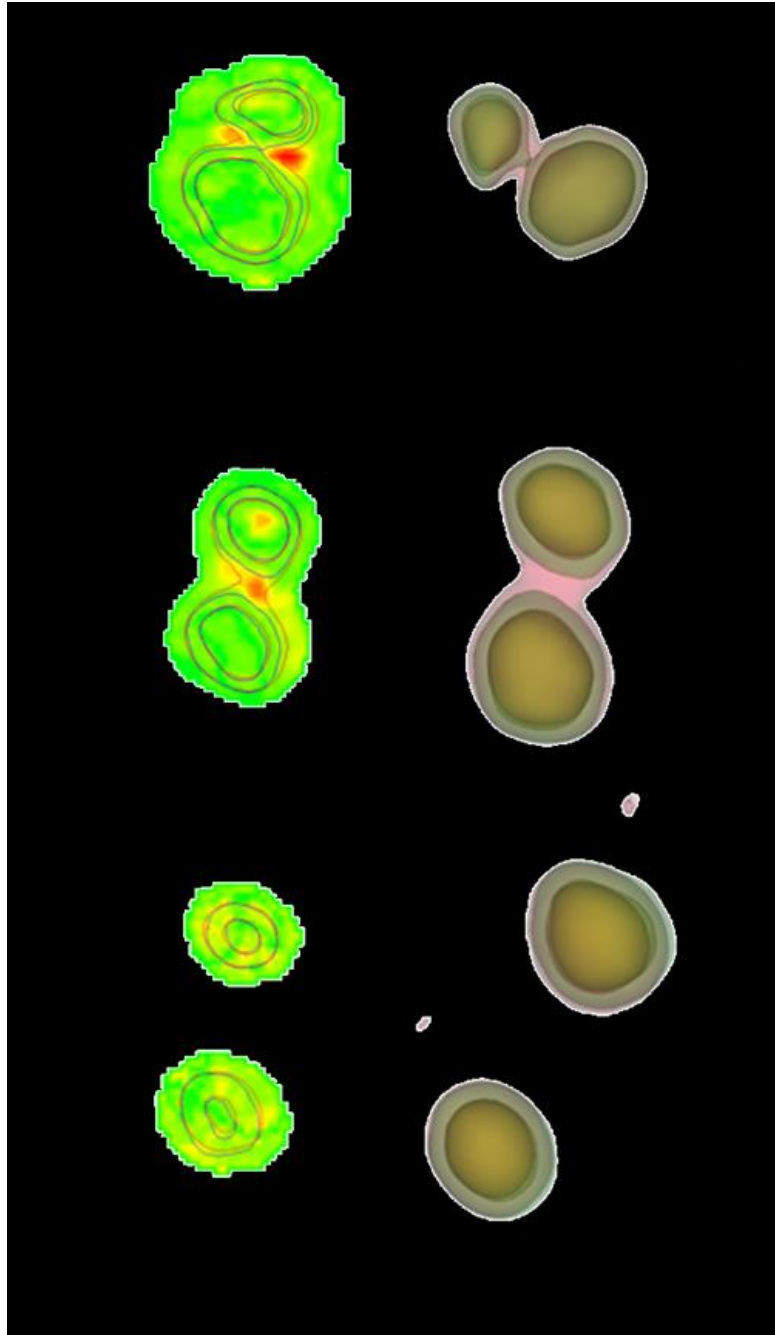
Figure 12. Comparison of isodose surfaces at 18 Gy and 12 Gy (right) between the 3D measurements (red) and treatment planning system (TPS) (green), along with the corresponding gamma maps (left), for treatment plans with target separations of 6 mm (top), 12 mm (middle), and 28 mm (bottom). In the gamma maps, gamma failing points are highlighted.

Table 2. Comparison of the DGI, V10, and V12 metrics between the 3D measurement

Target Separation (cm)	3D Measurement			TPS Calculation		
	DGI	V10 (cc)	V12 (cc)	DGI	V10 (cc)	V12 (cc)
0.6	73.6	9.39	6.88	77.2	9.37	6.61
1.2	71.68	11.36	8.257	80.6	9.98	6.95
2.8	83.8	8.13	6.17	83.1	8.32	6.17

In the third module of the study, two single-isocenter multitarget SRS plans were delivered to the anthropomorphic 3D dosimetry system, one with 5 targets and the other with 10 targets. The 3D dose distribution of one target at the isocenter was measured and compared to the TPS calculation. Figures 13 and 14 provide a visual comparison of the isodose surface and isodose lines in the transverse, coronal, and sagittal views. The measured dose distribution closely corresponds to the calculated dose distribution, except for the region connecting the two targets, where some deviations are observed. The closet distance between the two targets in these two plans are 2.5 cm. Gamma tests were performed using the criteria of 3%/3mm, 3%/2mm, and 2%/2mm, resulting in passing rates of 99.5%, 98.5%, and 95.1% for the 5-target plan, and 99.4%, 94.6%, and 92% for the 10-target plan. Table 2 presents the measured and calculated plan quality metrics. For the 5-target plan, the measured DGI is 7.43 lower compared to the calculated value, indicating a discrepancy in intermediate dose delivered. Additionally, the measured V10 and V12 values are 0.53 and 0.26 higher, respectively, compared to the calculated values. Similarly, for the 10-target plan, the measured DGI is 7.36 lower, and the measured V10 and V12 values are 0.87 and 0.54 higher, respectively, compared to the calculated values. These results indicate that while the

measured dose distributions closely resemble the calculated distributions for the individual targets, there are discrepancies in the region connecting the targets.
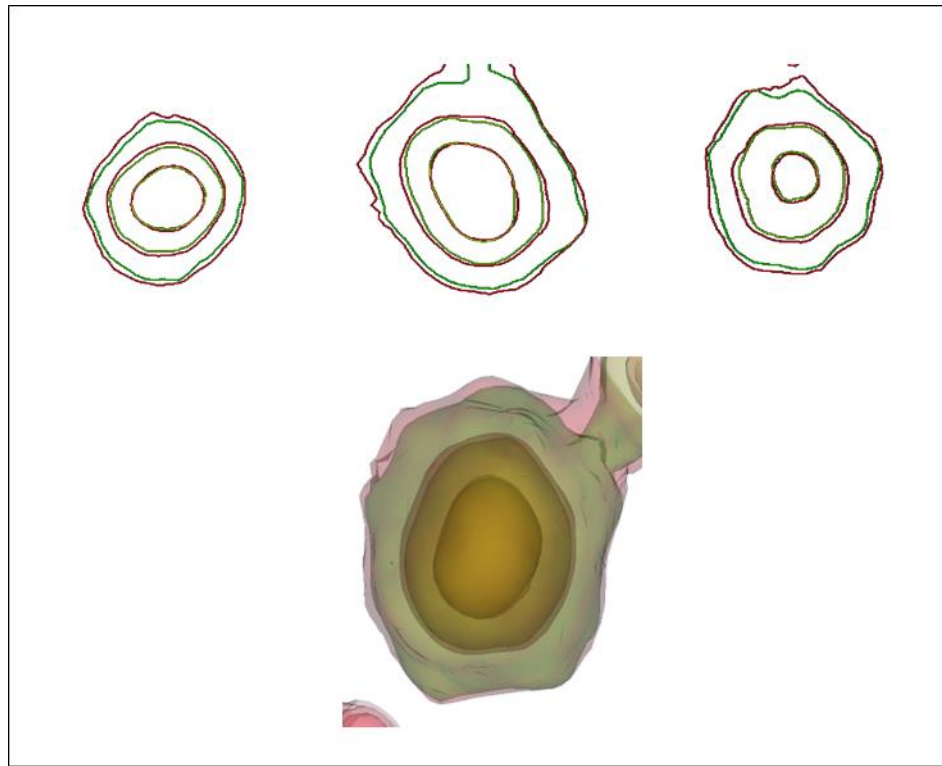
Figure 13. Comparison of isodose lines (18 Gy, 12 Gy, and 9 Gy) on the transverse, coronal, and sagittal planes (top) and isodose surface (bottom) between the 3D measurements (red) and TPS (green) for the treatment plan with 5 multiple targets.
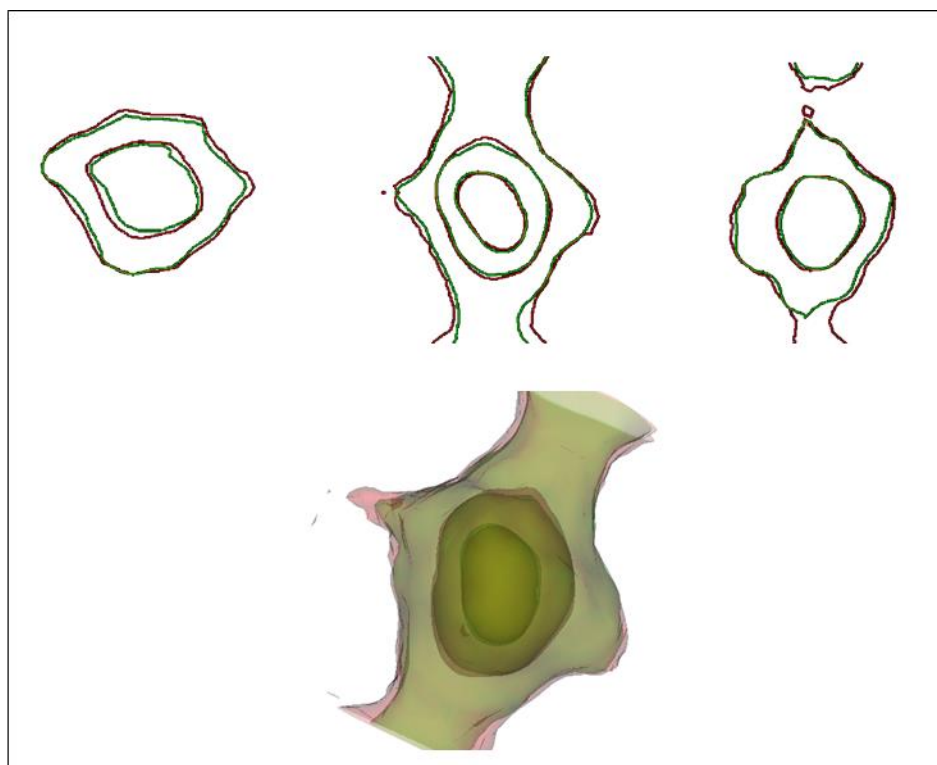
Figure 14. Comparison of isodose lines (18 Gy, 12 Gy, and 9 Gy) on the transverse, coronal, and sagittal planes (top) and isodose surface (bottom) between the 3D measurements (red) and TPS (green) for the treatment plan with 10 multiple targets.

Number of Targets	3D Measurement			TPS Calculation		
	DGI	V10 (cc)	V12 (cc)	DGI	V10 (cc)	V12 (cc)
5	80.91	5.15	3.6	88.34	4.62	3.34
10	78.12	5.77	4.09	85.48	4.90	3.55

Table 3. Comparison of the DGI, V10, and V12 metrics between the 3D measurement and TPS for the third module.

4.4 Discussion

This work aims to present a comprehensive and systematic end-to-end verification process of a radiosurgery platform utilizing a novel anthropomorphic 3D dosimetry system. The study specifically addresses the critical need for dosimetric and mechanical verification of the radiosurgery platform in the Radiation Oncology clinic, particularly when delivering high fractional doses to multiple targets with small setup margins. The linearity of the measured optical density in relation to the delivered SRS dose within the range of 0-25 Gy is paramount to achieve accurate 3D dose measurements, as any non-linearity could introduce systematic measurement errors. To address this, the feasibility of employing the 3D dosimeter, PRESAGE, with a novel formulation was assessed. The results indicate that this dosimeter formulation exhibits a clinically acceptable linear dose response and signal-to-noise ratio, making it suitable for SRS dosimetry applications.

The signal-to-noise ratio has traditionally posed a significant challenge in 3D dosimetry due to various sources of systematic and statistical noise. Using the in-house optical CT scanner with a fiber optic taper, the stray light contamination can be effectively mitigated. In addition, to enhance the acquisition of 3D dose data, an angular-sorted background subtraction technique was implemented. This technique effectively removes systematic uncertainties originating from impurities on the scanner window, within the dosimeter itself, and artifacts arising from light reflection and refraction. The results demonstrate that accurate background subtraction can reduce the standard deviation magnitude by an estimated 77%. This represents a significant improvement for 3D dosimetry and enhances its applicability in clinical practice.

The dosimetric verification of the developed 3D dosimetry system involved the utilization of a stack of radiochromic films, which were placed in the same anthropomorphic phantom with customized inserts. To the best of our knowledge, this study is the first to directly compare the

124

dose distributions acquired by these two dosimeters in an anthropomorphic phantom. Radiochromic films offer the advantage of a higher signal-to-noise ratio. However, due to their non-linear dose response, establishing the calibration curve becomes more labor-intensive. On the other hand, the 3D dosimeter facilitates a more efficient acquisition of 3D dose distribution. The results indicate that the measured dose differences between the two dosimeters fall within the measurement uncertainties of both systems.

In the first module of the study, an evaluation was conducted to examine the accuracy of the machine in delivering single-isocenter multitarget treatments when the targets are positioned off-axis. The measurements revealed a 1.5 mm shift in the dose distribution compared to the planned dose distribution when the target was positioned 7 cm off-axis. This shift in the dose distribution can be attributed to mechanical errors associated with the machine as well as uncertainties arising from the image-guided system. This assessment provides valuable insights into the machine's capability to accurately deliver treatments involving multiple targets positioned off-axis. Furthermore, the results indicate that conventional gamma tests, which are commonly used for dose verification, may not possess the required sensitivity to detect delivery errors up to 1.5 mm. The second module focused on investigating the discrepancy between the measurements and the TPS calculation of the intermediate-to-low dose spillage when the two targets are positioned close to each other at a certain distance. The measured higher dose in the intermediate dose region connecting the two targets may be attributed to uncertainties in the TPS modeling of out-of-field dose and MLC characteristics. As a result, lower DGI values and higher V10 and V12 values were observed in the measured 3D dose distribution compared to the TPS calculation. In the third module, the influence of irradiating multiple targets on the intermediate-to-low dose spillage was

examined. The measured V10 and V12 values agreed with the dose calculation within 1 cc. However, lower DGI values were obtained from the measurements compared to the calculation. These benchmark tests provide a comprehensive evaluation of the radiosurgery platform used for stereotactic radiosurgery treatments. They offer additional mechanical and dosimetric information that can enhance the current commissioning process. The study also investigates the feasibility of measuring plan quality metrics using 3D dosimetry and compares them with those obtained from the TPS. This provides valuable insights into the accuracy of MLC and out-of-field dose modeling. Additionally, the 3D gamma map assists in identifying the location of dose discrepancies in 3D space, which cannot be achieved through traditional 2D dose verification methods.

Given that radiosurgery necessitates precise and accurate dose delivery within 1 mm uncertainties, conducting end-to-end testing to evaluate the overall treatment uncertainty is vital. The anthropomorphic 3D dosimetry system described herein offers a methodology to simulate a patient's treatment from simulation to treatment delivery and assess the overall treatment uncertainty. This developed 3D dosimetry system can be utilized for commissioning newly acquired radiosurgery platforms or for remote auditing and verification of existing radiosurgery programs.

4.5 Conclusion

In conclusion, the study presents a novel anthropomorphic 3D dosimetry system designed for end-to-end testing of a single-isocenter radiosurgery platform. The investigation focused on evaluating the system's feasibility in measuring overall treatment uncertainties and dosimetric discrepancies by assessing benchmark plans. Notably, the system enables the measurement of essential plan quality metrics, including V10, V12, and DGI, in addition to conventional gamma tests. Moreover, the system effectively captures mechanical errors during off-axis target delivery and enables the

visualization of dose discrepancies in 3D space. This comprehensive evaluation capability enhances the commissioning and verification process, instilling greater confidence in the treatment modality and assuring patient safety.

References or Bibliography

1. Limon, D., McSherry, F., Herndon, J., Sampson, J., Fecci, P., Adamson, J., ... & Kim, G. J. (2017). Single fraction stereotactic radiosurgery for multiple brain metastases. Advances in radiation oncology, 2(4), 555-563.

2. Meijer, O. W. M., Vandertop, W. P., Baayen, J. C., & Slotman, B. J. (2003). Single-fraction vs. fractionated linac-based stereotactic radiosurgery for vestibular schwannoma: a single-institution study. International Journal of Radiation Oncology* Biology* Physics, 56(5), 1390-1396.

3. 3.Oh, B. C., Pagnini, P. G., Wang, M. Y., Liu, C. Y., Kim, P. E., Yu, C., & Apuzzo, M. L. (2007). Stereotactic radiosurgery: Adjacent tissue injury and response after high-dose single fraction radiation: Part i—histology, imaging, and molecularevents. Neurosurgery, 60(1), 31-45.

4. Bernard, M. E., Wegner, R. E., Reineman, K., Heron, D. E., Kirkwood, J., Burton, S. A., & Mintz, A. H. (2012). Linear accelerator based stereotactic radiosurgery for melanoma brain metastases. Journal of Cancer Research and Therapeutics, 8(2), 215-221.

5. Lim, M., Gibbs, I. C., Adler Jr, J. R., Martin, D. P., & Chang, S. D. (2003). The efficacy of linear accelerator stereotactic radiosurgery in treating glomus jugulare tumors. Technology in cancer research & treatment, 2(3), 261-265.

6. Gigliotti, M. J., Hasan, S., Liang, Y., Chen, D., Fuhrer, R., & Wegner, R. E. (2018). A 10-year experience of linear accelerator-based stereotactic radiosurgery/radiotherapy (SRS/SRT) for paraganglioma: a single institution experience and review of the literature. Journal of radiosurgery and SBRT, 5(3), 183.

7. Wu, A., Lindner, G., Maitz, A. H., Kalend, A. M., Lunsford, L. D., Flickinger, J. C., & Bloomer, W. D. (1990). Physics of gamma knife approach on convergent beams in stereotactic radiosurgery. International Journal of Radiation Oncology* Biology* Physics, 18(4), 941-949.

8. Grandhi, R., Kondziolka, D., Panczykowski, D., Monaco, E. A., Kano, H., Niranjan, A., ... & Lunsford, L. D. (2012). Stereotactic radiosurgery using the Leksell Gamma Knife Perfexion unit in the management of patients with 10 or more brain metastases. Journal of neurosurgery, 117(2), 237-245.

9. Maitz, A. H., Wu, A., Lunsford, L. D., Flickinger, J. C., Kondziolka, D., & Bloomer, W. D. (1995). Quality assurance for gamma knife stereotactic radiosurgery. International journal of radiation oncology, biology, physics, 32(5), 1465-1471.

10. Hartgerink, D., Swinnen, A., Roberge, D., Nichol, A., Zygmanski, P., Yin, F. F., ... & Zindler, J. (2019). LINAC based stereotactic radiosurgery for multiple brain metastases: guidance for clinical implementation. Acta Oncologica, 58(9), 1275-1282.

11. Topkan, E., Kucuk, A., Senyurek, S., Sezen, D., Durankus, N. K., Akdemir, E. Y., ... & Selek, U. (2021). Stereotactic Radiosurgery Techniques and Quality Assurance for Brain Metastases. Highlights on Medicine and Medical Research Vol. 2, 114-131.

12. Reynolds, T. A., Jensen, A. R., Bellairs, E. E., & Ozer, M. (2020). Dose gradient index for stereotactic radiosurgery/radiation therapy. International Journal of Radiation Oncology* Biology* Physics, 106(3), 604-611.

13. Raza, G. H., Capone, L., Tini, P., Giraffa, M., Gentile, P., & Minniti, G. (2022). Single-isocenter multiple-target stereotactic radiosurgery for multiple brain metastases: dosimetric evaluation of two automated treatment planning systems. Radiation Oncology, 17(1), 116.

14. Sahgal, A. (Ed.). (2021). Image-guided hypofractionated stereotactic radiosurgery: a practical approach to guide treatment of brain and spine tumors. CRC Press.

15. Milano, M. T., Grimm, J., Niemierko, A., Soltys, S. G., Moiseenko, V., Redmond, K. J., ... & Kleinberg, L. R. (2021). Single-and multifraction stereotactic radiosurgery dose/volume tolerances of the brain. International Journal of Radiation Oncology* Biology* Physics, 110(1), 68-86.

16. Weingarten, N., Kruser, T. J., & Bloch, O. (2019). Symptomatic radiation necrosis in brain metastasis patients treated with stereotactic radiosurgery and immunotherapy. Clinical Neurology and Neurosurgery, 179, 14-18.

17. Osei, E., Graves, S., & Darko, J. (2022). Retrospective analysis of portal dosimetry pre-treatment quality assurance of intracranial SRS/SRT VMAT treatment plans. Journal of Radiotherapy in Practice, 21(4), 540-552.

18. Hsieh, E. S., Hansen, K. S., Kent, M. S., Saini, S., & Dieterich, S. (2017). Can a commercially available EPID dosimetry system detect small daily patient setup errors for cranial IMRT/SRS?. Practical radiation oncology, 7(4), e283-e290.

19. Sakhalkar, H., Sterling, D., Adamovics, J., Ibbott, G., & Oldham, M. (2009). Investigation of the feasibility of relative 3D dosimetry in the Radiologic Physics Center Head and Neck IMRT phantom using Presage/optical-CT. Medical physics, 36(7), 3371-3377.

20. Oldham, M., Thomas, A., O'Daniel, J., Juang, T., Ibbott, G., Adamovics, J., & Kirkpatrick, J. P. (2012). A quality assurance method that utilizes 3D dosimetry and facilitates clinical interpretation. International Journal of Radiation Oncology* Biology* Physics, 84(2), 540-546.

21. Ezzell, G. A., Burmeister, J. W., Dogan, N., LoSasso, T. J., Mechalakos, J. G., Mihailidis, D., ... & Xiao, Y. (2009). IMRT commissioning: multiple institution planning and dosimetry comparisons, a report from AAPM Task Group 119. Medical physics, 36(11), 5359-5373.

22. Dimitriadis, A., Tsang, Y., Thomas, R. A., Palmer, A. L., Eaton, D., Lee, J., ... & Clark, C. H. (2020). Multi-institutional dosimetric delivery assessment of intracranial stereotactic radiosurgery on different treatment platforms. Radiotherapy and Oncology, 147, 153-161.

23. Zhao, L., Newton, J., Oldham, M., Das, I. J., Cheng, C. W., & Adamovics, J. (2012). Feasibility of using PRESAGE® for relative 3D dosimetry of small proton fields. Physics in Medicine & Biology, 57(22), N431.

24. Patent Application Publication: Pub No: US 2022/0412877 A1. Three-Dimensional Dosimetry Procedures, Methods and Devices, and Optical CT Scanner Apparatus Which Utilizes Fiber Optic Taper for Collimated Images.

Chapter 5

Small Field Data Acquisition for Megavoltage and

Kilovoltage Photon Beams using 3D Optical-CT

Dosimetry System

5.1 Introduction

With the improvements of the treatment planning, online-imaging, and delivery system for radiotherapy, more modulated and conformal dose distribution can be delivered to the target precisely without overdosing the normal tissue. In addition, further dose escalation to improve the tumor control rate can be achieved. Using linear accelerator for treatment delivery, small megavoltage photon fields can be formed by jaws, multileaf collimators, and cones[1, 2]. What sets the small field apart from the conventional field is the loss of lateral charge particle equilibrium when the beam half width is smaller than the maximum range of secondary electrons. The penumbrae at each side of the field overlap with each other's, and thus the profile looks like a Gaussian curve. Depending on the detector size and the field size, the detector may be larger than the field size, and thus a correction factor is necessary to correct the initial measurements. The volume average effect influences the detected signal, when the detector size is larger than the field size and the signal produced is proportional to the mean dose delivered to the sensitive volume of the detector[3]. In addition, Bragg-Gray cavity[4] theory cannot be applied to the small field condition due to the perturbation of the charged particle fluence by the presence of a detector. Due to the difficulty of small field dosimetry, International Atomic Energy Agency (IAEA) technical report 483[3] and American Association of Medical Physics (AAPM) task group 155[5] have been published to address the issue and provide dosimetry guidance.

To acquire relative dosimetry of small photon fields, the dosimeters need to have high spatial resolution. In addition, the positioning of the detectors is important to avoid dose underestimation. The ideal dosimeters to measure relative small field dosimetry are water equivalent (energy independent), linear response to the dose delivered[6-8]. However, most of the detectors require some sorts of corrections. For output factor measurements, volume average effect, dose rate dependence

and energy dependence can influence the dose measurements. For PDD and beam profiles measurements, spatial resolution, orientation dependence, energy dependence, and dose rate dependence are important. Many types of dosimeters have been used for small field dosimetry, including ion chambers[9], silicon diodes[10], diamond detectors[11], plastic and organic scintillators[12], films[13], metal oxide semiconductor field-effect transistors (MOSFETs)[14], thermoluminescent dosimeters (TLD), optically stimulated luminescence detectors (OSLDs)[15]. However, each dosimeter has its own limitations and uncertainties. Published guidance should be followed when using these dosimeters to avoid gross dosimetry errors.

Small field dosimetry for kilovoltage photon beams is more challenging than megavoltage photon beams[19-20]. First, the dose fall-off of kilovoltage beam is much faster than megavoltage beam, and thus the required resolution of the detectors is higher. Secondly, photoelectric effect is the primary interaction process for kilovoltage beam, and thus the atomic number of the detectors can influence the dose measurements. One of the major applications of kilovoltage small field dosimetry is the dosimetry for small animal radiation platform. Animal models have been heavily utilized in the research of novel cancer treatment strategies. More advanced types of animal radiation platform have been commonly adopted in the labs. These small animal radiation platforms[16-18] have the capability to perform online imaging when test subject is on the couch, generate treatment plans, and deliver small photon fields. Ensuring the accuracy of research findings relies on the dosimetry methodology to verify the administered dose.

The dosimeters suitable for kilovoltage small field dosimetry include radiochromic film, OSLDs, MOSFETs, diamond detectors, alanine – electron para-magnetic resonance due to their high resolution/small sensitive volume[19, 20]. For point dose measurements, the positioning of the dosimeter inside the small field can influence the dose measured. Radiochromic films have been

found to be useful for surface dose and percentage depth dose measurements. A good agreement between the radiochromic film and Monte Carlo simulation for small field dosimetry has been reported[13]. However, radiochromic films present energy dependence in the kilovoltage energy range. Similarly, for OSLD, due to the high effective atomic number, the energy dependence should be investigated for each beam quality[21]. MOSFET detector was found to be energy independent for certain kilovoltage energy range, and nearly independent of the angle of incidence of the beam[22]. Monte Carlo study of microdiamond detector has shown that the diamond detector has inter-detector response variation at low-energy photon beams due to the effective thickness of the active volume[23]. In addition, the relative intrinsic energy response of the detector is two times higher in 25, and 50 kV photon beams compared to the megavoltage beam.

3D dosimeter, PRESAGE, combined with optical CT scanner, can provide high resolution dose images without energy dependence and dose rate dependence. In addition, the 3D dose can be acquired simultaneously without the positioning uncertainties. In this study, the methodology was employed to acquire the dosimetry data of small megavoltage and kilovoltage photon beams (225 kV). For megavoltage study, dose distributions, beam profiles, and PDD curves of the small photon fields, formed by MLC, with field sizes of 6, 8, 10, 12 and 15 mm were measured. In addition, small treatment fields with field sizes smaller than 2 cm were measured and compared with the treatment planning system. For kilovoltage study, beam profiles and PDD curves of the photon beams with the field sizes of 3 mm and 1 cm from a pre-clinical platform, Small Animal Radiation Research Platform (SARRP) (Xstrahl, Suwanee, GA) were measured. The results were compared with those from the EBT3 radiochromic films. This study aims to investigate the dosimetric accuracy for the 3D dosimetry system to evaluate small photon fields. The results can provide insight into its utility for small field dosimetry.

5.2 Materials and Methods

5.2.1 Determination of the absorbed dose in water for small photon fields

For conventional broad beams, a reference field with 10×10 cm field size is used for the determination of absolute dose following AAPM TG51 (MV)[24] or TG61 (kV)[25] and the reference ionization chamber is sent to Accredited Dosimetry Calibration Laboratories for the calibration coefficient in terms of absorbed dose to water of the ionization chamber measured under reference conditions at a standard laboratory. Co-60 and UW250-M photon beams were used in ADCL for the calibration coefficient of megavoltage and kilovoltage photon beam. Machine specific reference (MSR) fields were introduced in IAEA TR483[3] for radiation platforms where the conventional 10 cm field size cannot be formed. The MSR fields have dimensions that are as close as possible to 10 cm or the largest field size the machine can form. Most importantly, they should extend at least a distance of charge particle equilibrium beyond the outer boundaries of the reference ionization chamber. After the dose of MSR field is determined, the clinical small field dose can be determined using small field detectors, such as ion chamber, plastic scintillator, diamond, and diode using output correction factors. In this study, the megavoltage photon measurement using linear accelerators has the MSR field with field size of 10 cm. However, for the measurements on SARRP, a machine specific reference field with the effective field size of 14 $\times$ 14 cm at 35 cm source to axis distance was used. The output factor for the treatment field size was measured using EBT3 radiochromic films. After the determination of the dose at the reference point, the dose at other points can be determined by the relative dosimetry (beam profiles, percent depth dose curves) acquired using the 3D optical CT dosimetry system.

5.2.2 Irradiation of the 3D dosimeters and radiochromic films

In the megavoltage photon study, 3D cylindrical dosimeters with 10 cm diameter and 9 cm height were irradiated using Truebeam (Varian, Palo Alto, CA) using 6M photon beam with the field sizes of 6 × 6, 8 × 8, 10 × 10, 12 × 12, 15 × 15 mm^2, formed by the MLC. The dosimeter was positioned vertically (Figure 1c). Acuros (AXB) dose calculation algorithm was employed. For background subtraction, to ensure that the dosimeter can be placed at the same location within the optical CT scanner after the irradiation, the dosimeter was irradiated with the scanning holder attached. Around 8 Gy was delivered to the depth of the maximum dose. Besides regular fields, intensity modulated radiotherapy (IMRT) treatment fields with the field sizes ranging from 8 mm to 3 cm were delivered to the 3D dosimeters with the dosimeters positioned horizontally (Figure 1b), which includes a C-spine stereotactic radiosurgery treatment plan, a skull base treatment plan, and a pancreas treatment plan. The measured results were compared with those from the treatment planning system. In order to compare the measurements obtained from the 3D dosimeter with the EBT3 film, an anterior-posterior modulated field was delivered to both the 3D dosimeter and EBT3 film with the same source-to-surface distance. The treatment plan dose was generated by performing a CT scan of the PRESAGE phantom and then using the resulting phantom geometry for treatment plan calculation. The highest resolution for treatment plan dose calculation is 1 mm.

In the kilovoltage photon study, 3D cylindrical dosimeters with 6 cm diameter and 6 cm height were used to evaluate the characteristics of 220 kVp/13 mA photon beams from the SARRP with the field sizes of 3 mm and 1 cm, formed by interchangeable fixed collimators. Figure 1a shows the dosimeter setup in the irradiator. EBT3 film was employed to verify the measured results. Two methods of film measurements were conducted, axial film measurement and vertical film measurement. For axial film measurements, the EBT3 films were stacked between solid water phantoms. This means that multiple films were placed on top of each other, creating a stack. The

beam enters the stack of film perpendicular to the film surface. On the other hand, in vertical film measurements, a single EBT3 film is placed with its surface parallel to the beam axis. To acquire the calibration curve for the EBT3 film, a series of films were irradiated to known doses ranging from 0 to 7 Gy at a depth of 2 cm in the solid water phantom. This process is commonly referred to as film calibration. The purpose of film calibration is to establish a relationship between the measured response of the film and the corresponding radiation dose delivered to the film. By exposing the film to a range of known doses, a calibration curve can be generated, which allows for the conversion of the film's optical density (OD) values to dose values in subsequent measurements

(a)
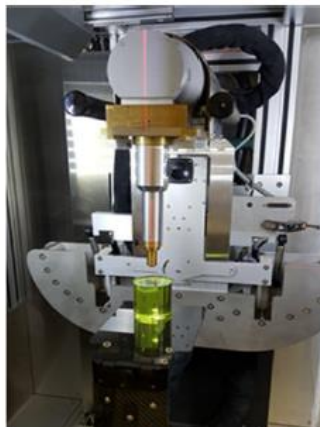
(b)
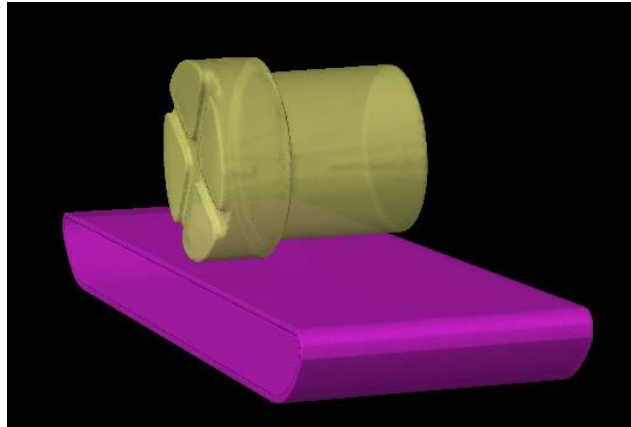
(c)
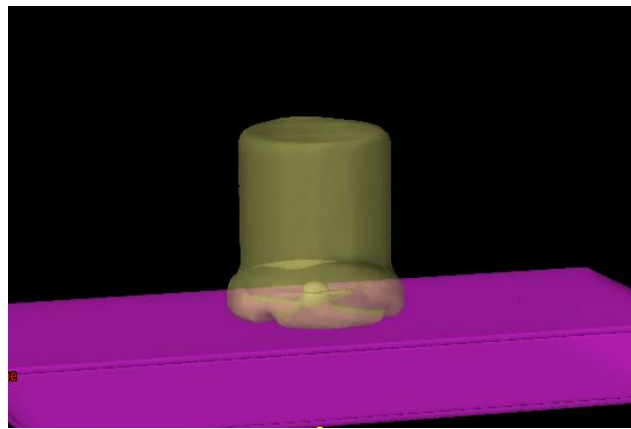
Figure 23. 3D dosimeter setup for megavoltage and kilovoltage small field irradiation (a) photograph showcasing the 3D dosimeter setup in SARRP, (b) diagram illustrating the placement of the dosimeter horizontally to the LINAC couch, and (c) diagram illustrating the placement of the dosimeter vertically to the LINAC couch.

5.2.3 Readout of the 3D dosimeters and EBT3 films

The readouts of irradiated PRESAGE dosimeters were performed with an in-house optical CT scanner. The dosimeters were put at the center of the rotation stage in the OCT scanner for evaluation. A total of 1200 projection images with a spatial resolution of 20 um were acquired for each scan. For background subtraction, the blank dosimeters before irradiation were scanned.

Before each scan, the optical CT scanner was checked for its alignment and cleanliness to prevent any structural artifacts. To scan the EBT3 films, a commercial Epson Expression 11000XL flatbed scanner was used for the readout of high resolution (300 dpi) images. Similar to the 3D dosimeters, a blank film was scanned for the optical density calculation. It's noteworthy that EBT3 radiochromic films have the characteristic of post-irradiation optical density growth. According to previous studies, optical densities can increase by about 2.5% between 24 hours and 14 days post irradiation and stabilize over the next 6 months. Ideally, the scanning time of the measurement films should be consistent with the scanning time of the calibration films.

5.2.4 Reconstruction and analysis of high-resolution 3D dose images

An in-house reconstruction code written using Matlab was employed to reconstruct the 3D dose distribution. Filtered back projection was performed using the inverse radon transform function. Before reconstruction, the projection images were cropped so that the center of the projection images corresponds to the center of the rotating stage. The measured image intensities were converted to optical densities using the background scan. The measured optical CT signals were then transformed to sinograms as the inputs to the inverse radon transform function. Each slice of the reconstructed image can be written as 16-bit tiff image. The 3D dosimeter, PRESAGE, has linear dose response, and thus the reconstructed image intensities are directly proportional to the dose delivered. 2D gamma tests were performed using a commercial software, DoseLab (Varian, Palo Alto, CA). PDD curves, beam profiles, and 2D isodose lines comparison were plotted using Matlab. The 3D dose images were resized to 1 mm resolution when comparing with the calculated dose images from the treatment planning system. When comparing with the films, 3D dose images with sub-millimeter resolution were used. In the megavoltage photon study, isodose lines, PDD curves, and beam profiles from 3D dosimeters were compared with the calculated dose.

Furthermore, the dose distributions obtained from regular and treatment field measurements were assessed using gamma tests. This involved comparing the results obtained from the 3D dosimeter with both the measured dose using EBT3 and the calculated dose. In the kilovoltage photon study, the PDD curves, beam profiles, and measured dose parameters such as penumbra, FWHM, symmetry, and flatness were compared between PRESAGE and EBT3 films.

5.3 Results

5.3.1 Small field dosimetry on megavoltage photon beam

5.3.1.1 Small field measurements with field size smaller than 1 cm

Small photon fields created by the MLC were measured using PRESAGE and EBT3 films. The measured results from both methods were compared with the calculated dose obtained from the TPS. Figure 2 displays dose images of photon fields with field sizes of 6×6, 8×8, and 10×10 mm² obtained from EBT3 film, PRESAGE, and TPS. It can be observed that there is end leaf leakage in each image. The beam profile across each field was plotted in Figure 3. For the 6×6 mm² field size, the penumbras and FWHM measured by all three methods agree within a 1% margin. For the 8×8 mm² and 10×10 mm² field sizes, the penumbras and FWHM measured by PRESAGE align with the film results within 1%. However, TPS overestimates the FWHM by 10% and underestimates the relative dose in low-dose regions (10% isodose line) by approximately 3%. The PDD curves obtained from PRESAGE align with those from TPS within a 1.4% margin after reaching the depth of maximum dose (Figure 4). Figure 5 illustrates a comparison of isodose lines between PRESAGE and TPS, as well as PRESAGE and film for the three measured field sizes. The dose images acquired by PRESAGE and film exhibit higher spatial resolution compared to the TPS calculation, and thus both measurements are in agreement with each other. Using gamma

tests with a criteria of 2% dose difference and 1.5 mm distance-to-agreement, the passing rates

between PRESAGE and film are 99.5%, 98.9%, and 99.5% for the field sizes of 6, 8, and 10 mm,

respectively. However, the passing rates between PRESAGE and TPS are 93.7%, 88.2%, and

90.1% for the same field sizes. Table 1 provides a summary of these results.
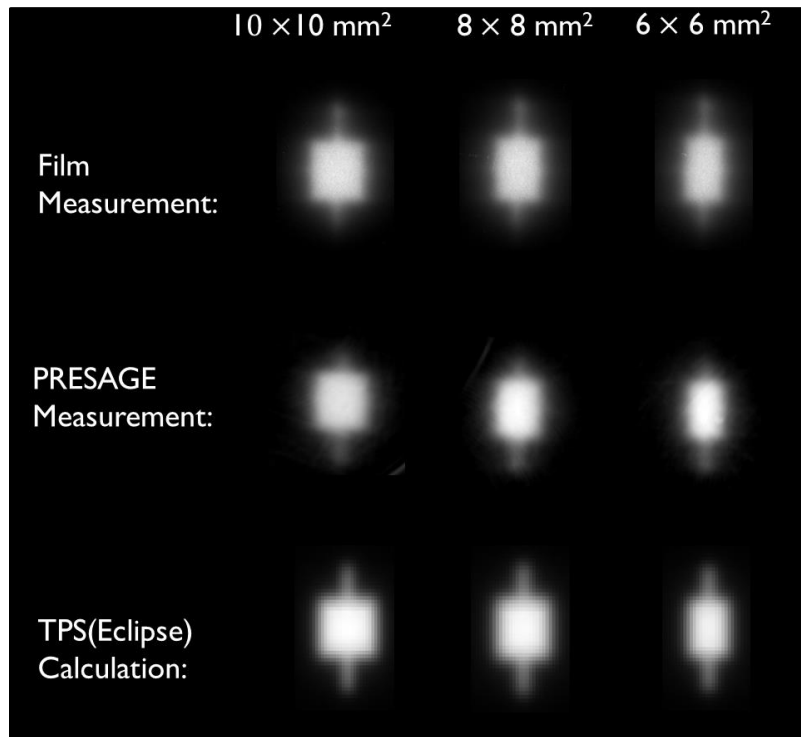
Figure 24. Comparison of acquired dose images for photon fields with field sizes of 6 × 6,8 × 8, and 10 × 10 mm2 from EBT3 film, PRESAGE, and TPS.
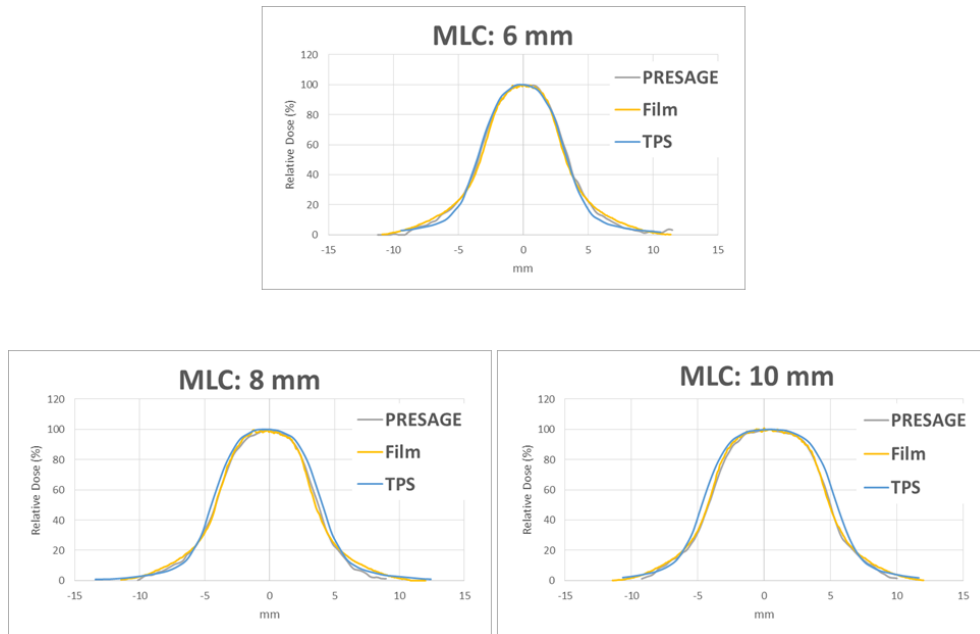
Figure 25. Beam profiles comparison across the measured photon fields with field sizes of 6 × 6, 8 × 8, and 10 × 10 mm2 using EBT3 film, PRESAGE, and TPS.

Field Size	Max Percent Difference (%) Before D$_{max}$
6 mm	2.5
8 mm	3.7
10 mm	3.5

Field Size	Max Percent Difference (%) After D$_{max}$
6 mm	1.40
8 mm	1.12
10 mm	0.92
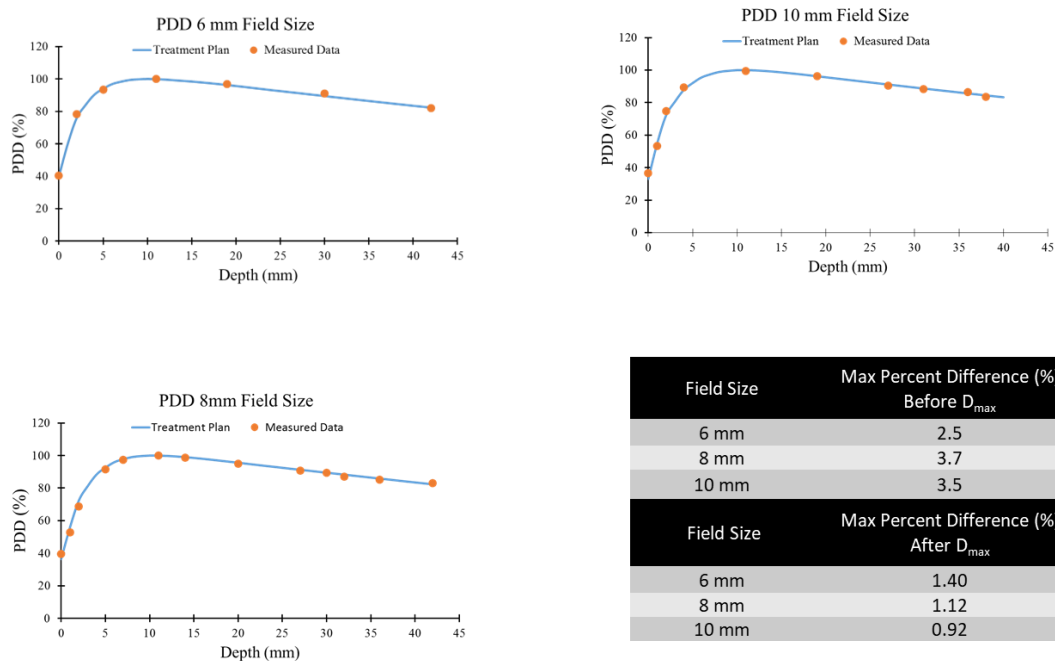
Figure 26. PDD curves comparison across the measured photon fields with field sizes of 6 × 6, 8 × 8, and 10 × 10 mm2 using PRESAGE, and TPS.
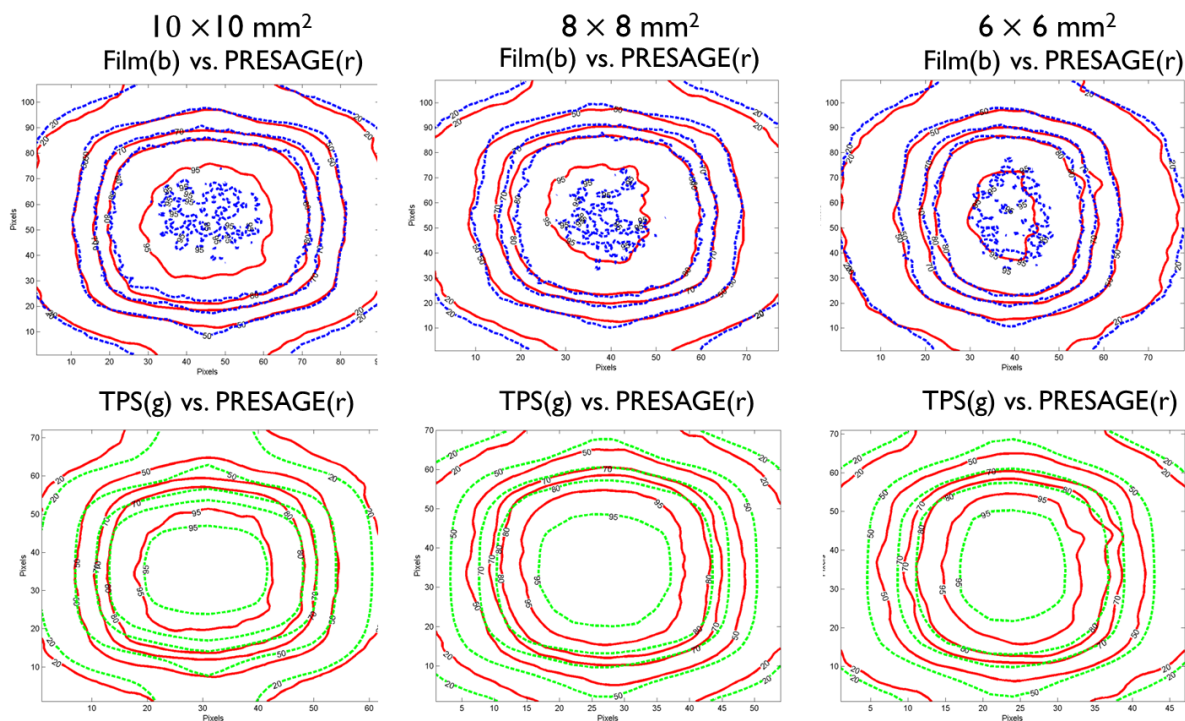
Figure 27. Isodose lines comparison across the measured photon fields with field sizes of 6 × 6, 8 × 8, and 10 × 10 mm2 using EBT3 film, PRESAGE, and TPS.

Table 4. Gamma passing rates comparison between PRESAGE and EBT3 film, as well as between PRESAGE and TPS, for the examined field sizes. Gamma criteria utilized: 2% dose difference and 1.5 mm distance-to-agreement.

10×10 mm^2	8×8 mm^2	6×6 mm^2
Film(b) vs. PRESAGE(r)	Film(b) vs. PRESAGE(r)	Film(b) vs. PRESAGE(r)
99.6%	98.9%	99.5%
TPS(g) vs. PRESAGE(r)	TPS(g) vs. PRESAGE(r)	TPS(g) vs. PRESAGE(r)
93.7%	88.2%	90.1%

5.3.1.2 Small field measurements with field size larger than 1 cm

Megavoltage photon fields with field sizes of 1.2 cm and 1.5 cm, created by the MLC, were measured using PRESAGE. The results obtained from PRESAGE were then compared with the calculated doses from the TPS. Figure 6 illustrates the reconstructed dose image obtained from the 3D dose measurement. The images clearly display the leaf end leakage and the shape of the MLC. Isodose line comparisons for the two measured field sizes are presented in Figure 7. By employing gamma comparison with a criteria of 2% dose difference and 2 mm distance-to-agreement, passing rates of 98.6% and 98.7% were achieved for the field sizes of 1.5 cm and 1.2 cm, respectively. This indicates a high level of agreement between the measured and calculated doses. The measured beam profiles align with the calculated beam profiles, as demonstrated in Figure 8.
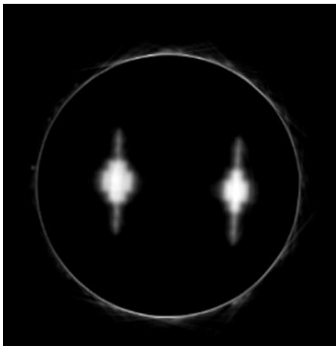
Figure 28. Reconstructed image from the 3D dosimeter for photon fields with field sizes of 1.2 cm and 1.5 cm, formed by MLC.
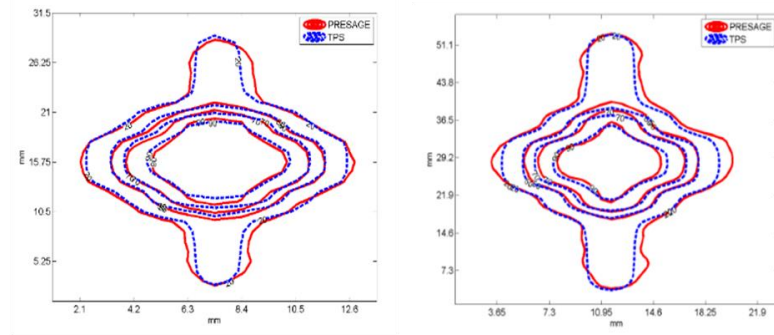
Figure 29. Comparison of isodose lines from the 3D dosimeter and TPS for photon fields with field sizes of 1.2 cm and 1.5 cm, formed by MLC.
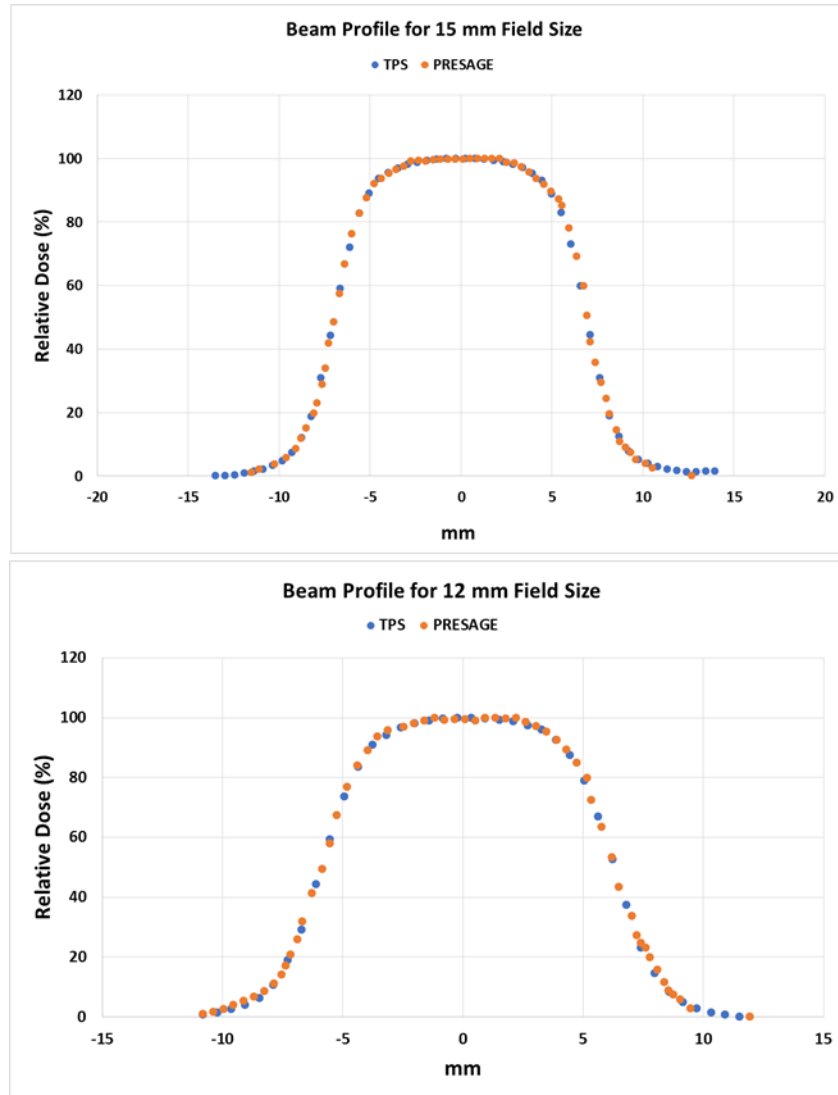
Figure 30. Comparison of beam profiles from the 3D dosimeter and TPS for photon fields with field sizes of 1.2 cm and 1.5 cm, formed by MLC.

5.3.1.3 Small treatment field measurements

For a small treatment field in a C-spine SRS treatment plan, with a field size corresponding to the 50% isodose line measuring 0.88 cm, PRESAGE was used for measurement and the results were registered to the TPS calculation for dose comparison. In the isodose line comparison, the relative dose was normalized to the dose maximum. By utilizing 3D dosimetry, 2D gamma tests were conducted at different treatment depths. Figure 9 presents the delivered dose cloud and the isodose

line comparison at two different treatment depths. Using a criteria of 2% dose difference and 1 mm distance-to-agreement, passing rates of 97.1% and 98% were achieved. This indicates a high level of agreement between the measured and calculated doses. In addition to PRESAGE, ArcCHECK (Sun Nuclear, FL), a clinically implemented cylindrical 2D diode array, was utilized to measure the passing rate for the same treatment plan. The passing rate obtained from ArcCHECK was 89%. Furthermore, using EBT3 radiochromic film, the passing rate was found to be 97.4%.
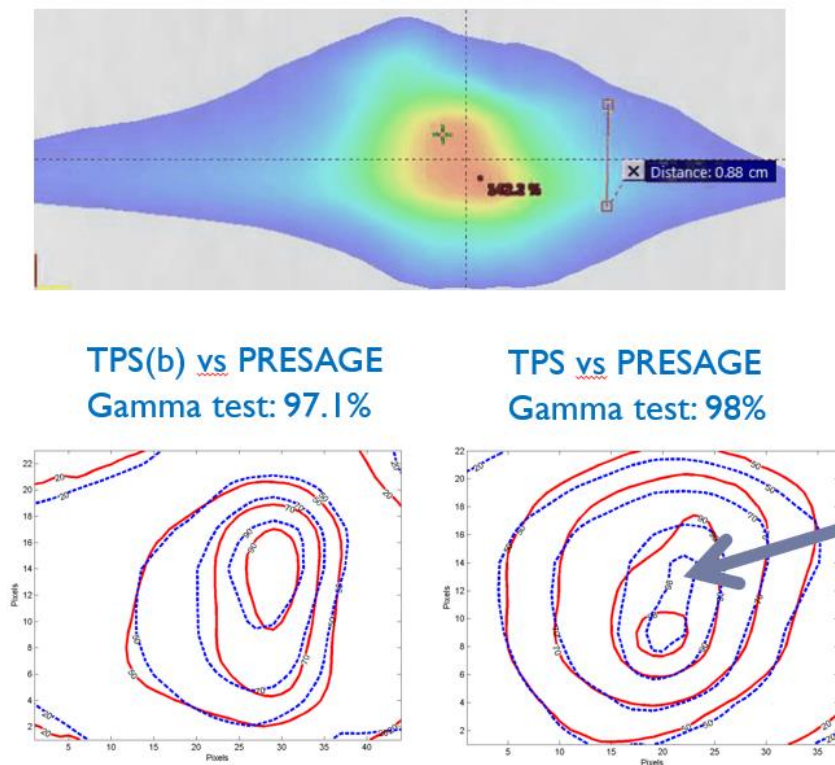
Figure 31. Top: Delivered dose cloud with a field size (50% isodose line) of 0.88 cm. Bottom: Comparison of isodose lines between the 3D dosimeter and treatment planning system (TPS) at two different treatment depths.

A treatment plan targeting a skull base tumor, with a field size of 2 cm, was measured using PRESAGE. Figure 10 showcases the treatment dose cloud and the corresponding isodose line

146

comparison. By applying a criteria of 2% dose difference and 1 mm distance-to-agreement, a gamma passing rate of 96.7% was achieved. This indicates a strong agreement between the measured dose using PRESAGE and the calculated dose. For this particular case, when the same treatment plan was measured using ArcCHECK, a cylindrical 2D diode array, the passing rate obtained was 94%.
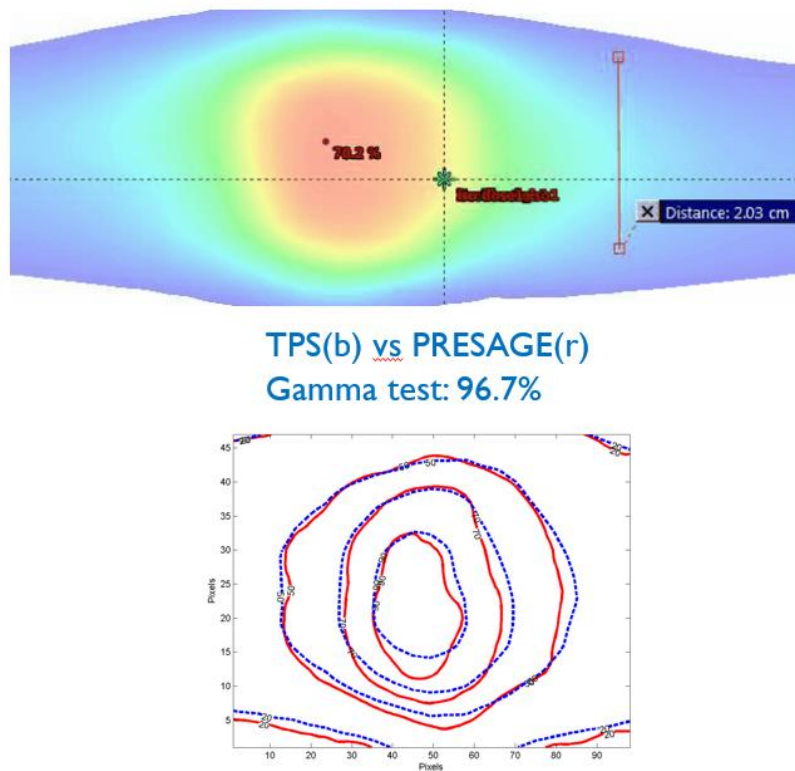
Figure 32. Top: Delivered dose cloud with a field size (50% isodose line) of 2 cm. Bottom: Comparison of isodose lines between the 3D dosimeter and treatment planning system (TPS).

To validate the measured dose from PRESAGE, a modulated field with a field size of 3 cm was delivered to both PRESAGE and radiochromic film in the anterior-posterior setup. The radiochromic film was positioned at the treatment depth where the prescription dose was delivered. The 2D dose plane at the same treatment depth, derived from the measured 3D dose cloud obtained

by PRESAGE, was compared with the dose measurement from the film. Unlike the comparison with the treatment planning system (TPS), this comparison allows for the exclusion of uncertainties stemming from the dose calculation. Furthermore, measured dose distributions can offer higher resolution compared to the calculated ones. Figure 11 illustrates the two measured dose clouds and the corresponding isodose line comparison. By employing a criteria of 2% dose difference and 1 mm distance-to-agreement, a passing rate of 99% was achieved. These findings highlight the reliability and accuracy of PRESAGE as a dosimeter, as well as its capability to capture dose distributions with higher resolution compared to the calculated doses. The
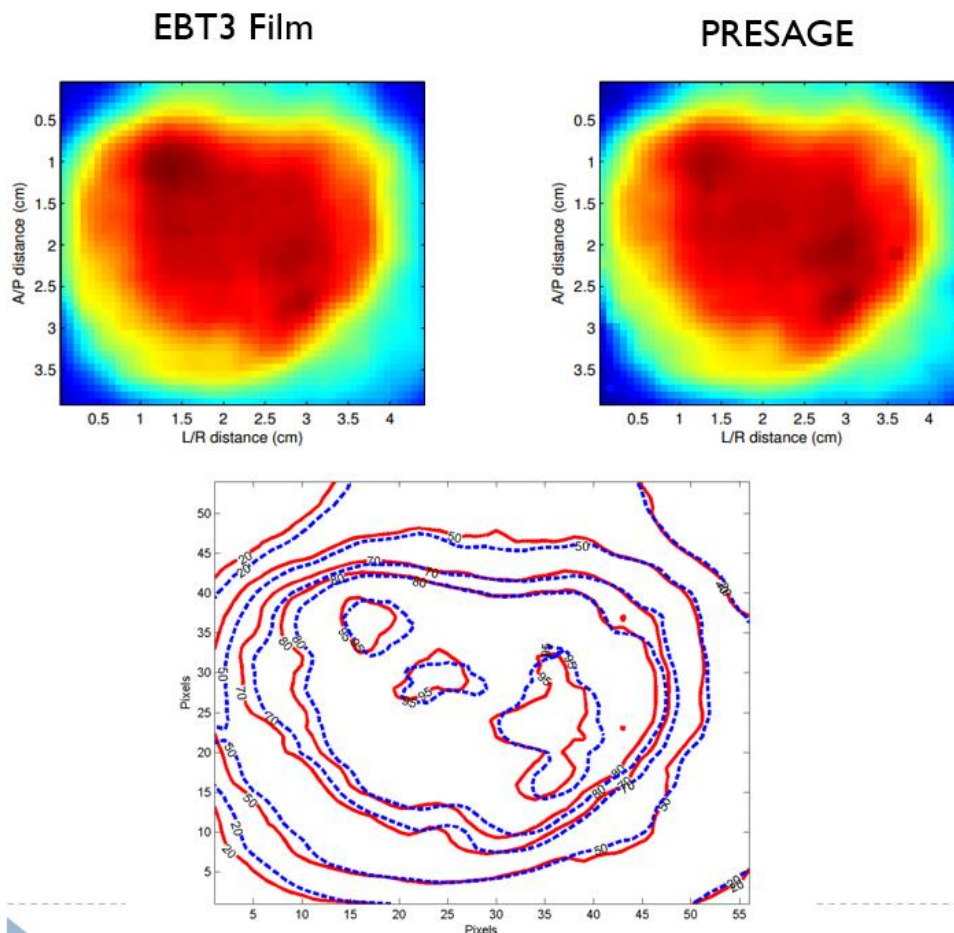
Figure 33. Top: Delivered dose cloud with a field size (50% isodose line) of 3 cm from the EBT3 film and 3D dosimeter. Bottom: Comparison of isodose lines between the 3D dosimeter and EBT3 film.

comparison with the radiochromic film further confirms the agreement between PRESAGE measurements and an independent dosimeter.

5.3.2 Small field dosimetry on kilovoltage photon beam

Following the guidelines provided by AAPM TG61, the output of the SARRP at the isocenter was determined to be 312 cGy/min at a depth of 2 cm in water, with a source-to-axis distance of 35 cm. To account for the energy dependence of EBT3 radiochromic film, a calibration curve was generated using the same machine by delivering known doses. The calibration curve was established using eight dose levels ranging from 0 to 7 Gy, and a third-order polynomial fitting was applied. For PRESAGE measurements, the calibration curve exhibited linearity for kilovoltage photons. Both calibration curves are displayed in Figure 12. Figure 13 presents the results of the PDD and beam profiles obtained from EBT3 film and PRESAGE for field sizes of 3 mm and 10 mm at depths of 10 mm, 20 mm, and 30 mm. In the comparison of PDD curves, the differences in PDD between PRESAGE and film measurements, both axial and vertical, were within 1% for depths shallower than 3 cm. However, at depths greater than 3 cm, PRESAGE measured a higher dose than EBT3 film by up to 3% and 4% for field sizes of 3 mm and 1 cm, respectively. Regarding the beam profile comparison, various dosimetry parameters including penumbra (distance between 20% and 80% isodose lines), FWHM, flatness, and symmetry were evaluated. Generally, for a field size of 3 mm, the penumbra and FWHM measurements at the three different depths agreed within 0.1 mm. For a field size of 10 mm, the penumbra difference measured was approximately 0.5 mm. Symmetry measurements exhibited an agreement within 1%, and flatness measurements agreed within 2%. Detailed results can be found in Tables 2 and 3. These findings demonstrate the accuracy and consistency of PRESAGE measurements

149

compared to EBT3 film, with minimal differences in dosimetric parameters for various field sizes

and depths.
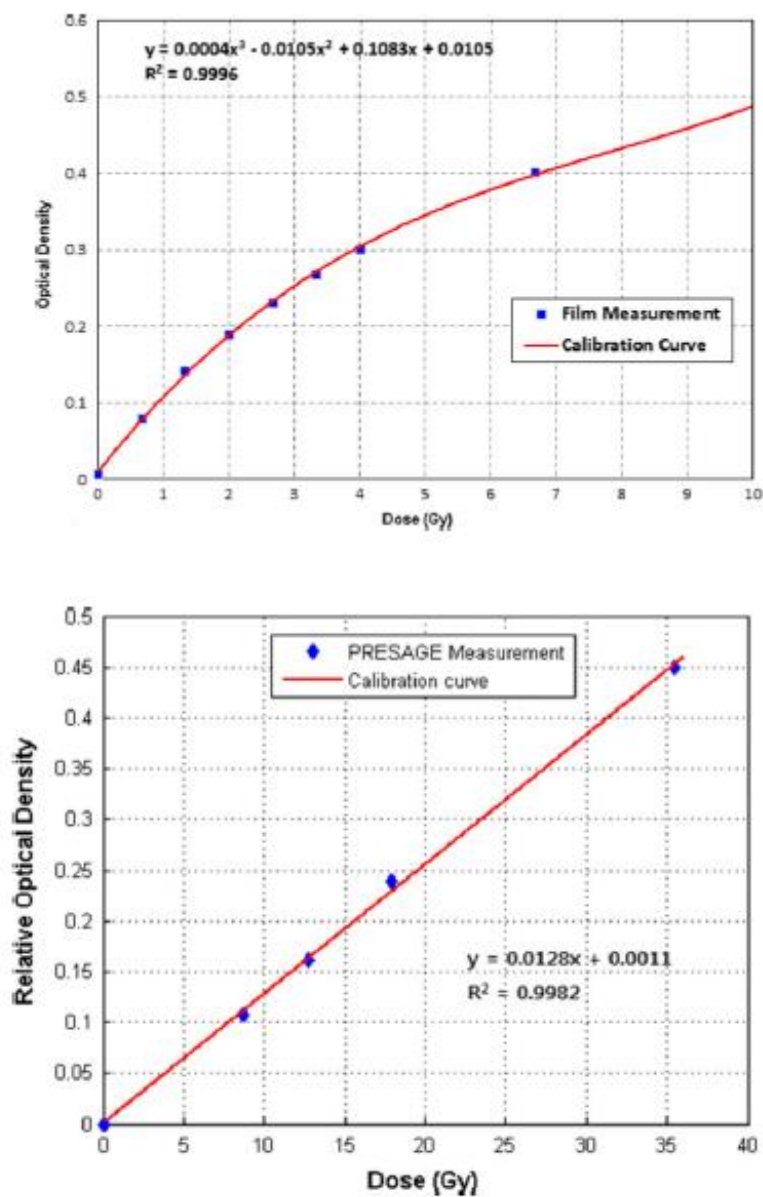
Figure 33. Calibration curves generated for kilovoltage dose measurements using EBT3 film (top) and the 3D dosimeter (bottom).
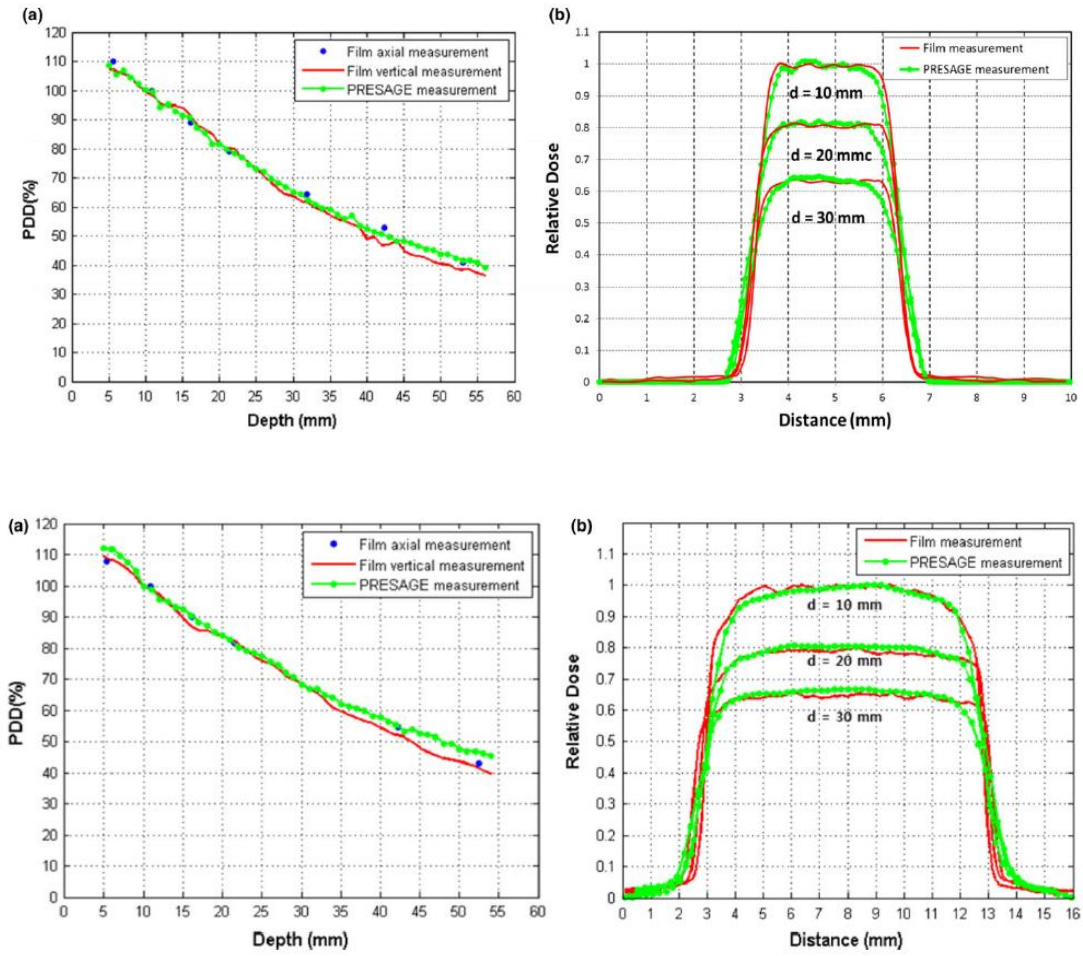
Figure 34. Comparison of PDD and beam profiles results from the EBT3 film and PRESAGE for the field sizes of 3 mm (top) and 10 mm (bottom) at the depths of 10 mm, 20 mm and 30 mm

Table 5. Comparison of penumbra, FWHM, symmetry, and flatness between EBT3 film and PRESAGE for the photon field with a 3 mm field size.

151

Measurement Depth (mm)	EBT3 Film			PRESAGE			Absolute difference		
	10	20	30	10	20	30	10	20	30
Penumbra (mm)	0.41	0.46	0.43	0.50	0.56	0.54	0.09	0.10	0.11
FWHM (mm)	3.04	3.12	3.22	3.06	3.13	3.21	0.02	0.01	0.01
Symmetry (%)	0.65	1.30	1.45	1.20	0.77	1.70	0.55	0.53	0.25
Flatness (%)	2.15	2.83	5.60	3.70	4.55	4.00	1.55	1.72	1.57

Table 6. Comparison of penumbra, FWHM, symmetry, and flatness between EBT3 film and PRESAGE for the photon field with a 10 mm field size.

Measurement Depth (mm)	EBT3 Film			PRESAGE			Absolute difference		
	10	20	30	10	20	30	10	20	30
Penumbra (mm)	0.47	0.48	0.49	0.95	0.98	0.99	0.48	0.50	0.50
FWHM (mm)	9.80	10.17	10.51	9.83	10.10	10.35	0.03	0.07	0.16
Symmetry (%)	0.45	1.35	0.65	0.46	0.80	0.60	0.01	0.55	0.05
Flatness (%)	1.93	2.33	1.13	2.30	2.63	3.40	0.37	0.03	2.27

5.4 Discussion

This study presents a comprehensive evaluation of the 3D dosimetry capabilities on small field dosimetry. In the first part, small MV photon fields formed by MLC were measured. The results from the 3D measurement agree with those from the EBT3 radiochromic films for all the measured field sizes, which has verified the accuracy of the dose measurements from the 3D dosimetry system. EBT3 radiochromic films have been recognized as the current standard of relative dosimetry, with the accuracy of dose measurement within 2%. However, due to the limitation of 2D measurements, multiple measurements are necessary to acquire comprehensive beam data. In addition, the alignment of the film with the beam axis is important for the PDD measurements of small fields if the film is placed parallel to the beam axis. For the photon fields with field sizes

smaller than 1 cm, the gamma passing rates between the PRESAGE and TPS are lower than those between the PRESAGE and radiochromic film, which shows that the discrepancies may come from the TPS dose calculation on small fields. The MLC positioning error is also critical for small field dosimetry. In figure 3, the discrepancies of profiles between measurement (PRESAGE and films) and TPS for FS 6, 8, 10 mm can be attributed to TPS calculation modeling or the MLC positioning error. In addition, the TPS dose calculation has the limitation of calculation resolution (1 mm), and out-of-field dose calculation. The input dosimetric leaf gap (DLG) in the TPS can influence the modeling of multileaf collimators, and thus the penumbra. The agreement has potential to be improved with the optimization of DLG value. For the small field measurements with the field sizes of 1.2 and 1.5 cm, the TPS dose calculation matches with the 3D measurements. The measured results using 3D dosimeter correspond to the measurements using other detectors in the previous publications. A study compared the measured PDD curves and beam profiles of a photon field with 1 cm field size using a microdiamond detector with the calculated results from TPS calculation. In general, the calculated PDD curves agree with the measured PDD curves. Using 1%/1mm criteria, the passing rate of the PDD and profiles measurements are over 96% and 98.5%, respectively. All points pass gamma with the criteria of 2%/2mm.

Using 3D dosimetry, small treatment fields can be measured and compared with the TPS calculation. The methodology provides an additional option to verify the radiation treatment fields. In this study, three treatment fields with field sizes ranging from 8 mm to 3 cm were evaluated. Using PRESAGE, all treatment plans passed the gamma tests with the passing rates ranging from 97% to 99%. One plan that passed the gamma test using PRESAGE failed the gamma test using the ArcCHECK dosimeter, which may be caused by the alignment of the dosimeter or the inter-diode spacing. An advantage of using 3D dosimetry for treatment field verification is that the

153

measured dose is the true combination of each delivered field in 3D space, and thus the measured dose discrepancies is close to actual treatment discrepancies. In addition, the location of the dose discrepancy can be identified. Using current patient QA methods, only the dose at a certain plane is evaluated. The dose discrepancies could be washed out if multiple fields are overlayed. The treatment field verification could be more clinically meaningful if 3D dose distribution is acquired.

In the kilovoltage study, there's overall good agreement for PDD curves from the 3D dosimeter and film at depths less than 3 cm. However, at the larger depth, PRESAGE measurements show a 3% higher depth dose, compared with the film vertical measurement. The discrepancy may be due to misalignment between the film and the beam path, especially when small treatment fields are measured. To overcome this issue, film axial measurements were conducted and the results match with PRESAGE measurements. Another discrepancy was shown in the penumbra measurements of the beam profiles. The slightly larger penumbra measured by PRESAGE may be due to the larger spatial resolution compared with the film. Although OCT scanner can provide submillimeter resolution, it could be compromised by the lower signal-to-noise ratio compared with EBT3 film. Due to the inherent tradeoff between signal-to-noise ratio and resolution when reconstructing 3D dose, the resolution was reduced to increase the signal to noise ratio. Lower resolution could lead to lower gradient of the penumbra measured. The advantage of using 3D dosimeter for the small field acquisition is that it doesn't require labor-intensive alignment of the dosimeter with the beam path. The 3D measurements are more efficient than other 2D or point dose measurements as comprehensive beam data can be acquired in one dosimeter and a single OCT scan. The 3D dosimeter itself is close to water-equivalent so no correction factor is needed.

The dosimetric investigation in this study provides an insight into the utility of a 3D dosimetry system on small field measurements. There are several challenges in small field dosimetry, such

as beam alignment, lack of charge particle equilibrium, beam spectrum change, volume average effect, and uncertainty in reference dosimetry. According to IAEA technical report 483, current dosimeters require correction factors applied to the measured signals. In addition, most of the dosimeters are not tissue-equivalent, and thus uncertainties from the spectrum change could be introduced. The presented 3D dosimetry system is a robust alternative to the existing small field dosimeters. The appealing characteristics of 3D dosimetry system includes energy independence, high resolution, linear dose response, and measurement efficiency. It could be applied to different radiation platforms for the evaluation of dosimetry accuracy and understanding of the comprehensive dosimetric characteristics.

5.5 Conclusion

In conclusion, the accurate measurement of small field dosimetry plays a crucial role in modern radiotherapy. With the advancements in radiation therapy techniques, the delivery of precise and accurate radiation doses to treatment targets has become possible, leading to the common use of small treatment fields with minimal prescribed margins in clinical practice. Additionally, for kilovoltage applications, small animal irradiators have been developed to deliver radiation fields with high precision, aided by online imaging. This study conducted a comprehensive evaluation of a 3D dosimetry system's capabilities in small field dosimetry for both kilovoltage and megavoltage photon beams. The methodology employed demonstrated the system's ability to provide clinically acceptable 3D dose measurements for photon fields with field sizes smaller than 1 cm, eliminating the need for dose corrections. PDD curves, beam profiles, and dose distributions were efficiently acquired using a single dosimeter. The evaluated 3D dosimetry system holds significant potential for applications in evaluating modern radiation platforms, verifying dose calculations from TPS, and validating measurements from other dosimeters. Its capacity to

accurately measure dose distributions in small fields contributes to enhancing the overall quality

assurance and precision of radiation therapy treatments.

References or Bibliography

1. Nutting, C., Dearnaley, D. P., & Webb, S. (2000). Intensity modulated radiation therapy: a clinical review. The British journal of radiology, 73(869), 459-469.

2. Cho, B. (2018). Intensity-modulated radiation therapy: a review with a physics perspective. Radiation oncology journal, 36(1), 1.

3. Palmans, H., Andreo, P., Huq, M. S., Seuntjens, J., Christaki, K. E., & Meghzifene, A. (2018). Dosimetry of small static fields used in external photon beam radiotherapy: summary of TRS-483, the IAEA–AAPM international Code of Practice for reference and relative dose determination. Medical physics, 45(11), e1123-e1145.

4. Ma, C. M., & Nahum, A. E. (1991). Bragg-Gray theory and ion chamber dosimetry for photon beams. Physics in medicine & biology, 36(4), 413.

5. Das, I. J., Francescon, P., Moran, J. M., Ahnesjö, A., Aspradakis, M. M., Cheng, C. W., ... & Sauer, O. A. (2021). Report of AAPM Task Group 155: megavoltage photon beam dosimetry in small fields and non-equilibrium conditions. Medical physics, 48(10), e886-e921.

6. Parwaie, W., Refahi, S., Ardekani, M. A., & Farhood, B. (2018). Different dosimeters/detectors used in small-field dosimetry: Pros and cons. Journal of medical signals and sensors, 8(3), 195

7. Lam, S. E., Bradley, D. A., & Khandaker, M. U. (2021). Small-field radiotherapy photon beam output evaluation: Detectors reviewed. Radiation Physics and Chemistry, 178, 108950.

8. Bagheri, H., Soleimani, A., Gharehaghaji, N., Mesbahi, A., Manouchehri, F., Shekarchi, B., ... & Dadgar, H. A. (2017). An overview on small-field dosimetry in photon beam radiotherapy: Developments and challenges. Journal of cancer research and therapeutics, 13(2), 175-185.

9. Laub, W. U., & Wong, T. (2003). The volume effect of detectors in the dosimetry of small fields used in IMRT. Medical physics, 30(3), 341-347.

10. Yarahmadi, M., Wegener, S., & Sauer, O. A. (2017). Energy and field size dependence of a silicon diode designed for small-field dosimetry. Medical Physics, 44(5), 1958-1964.

11. Talamonti, C., Kanxheri, K., Pallotta, S., & Servoli, L. (2021). Diamond detectors for radiotherapy X-ray small beam dosimetry. Frontiers in Physics, 9, 632299.

12. Beddar, S., Tendler, I., Therriault-Proulx, F., Archambault, L., & Beaulieu, L. (2021). Recent advances and clinical applications of plastic scintillators in the field of radiation therapy. Plastic Scintillators: Chemistry and Applications, 425-460.

13. Gonzalez-Lopez, A., Vera-Sanchez, J. A., & Lago-Martin, J. D. (2015). Small fields measurements with radiochromic films. Journal of Medical Physics/Association of Medical Physicists of India, 40(2), 61.

14. Amin, M. N., Heaton, R., Norrlinger, B., & Islam, M. K. (2011). Small field electron beam dosimetry using MOSFET detector. Journal of Applied Clinical Medical Physics, 12(1), 50-57.

15. Pham, C. (2013). Characterization of OSLDs for use in small field photon beam dosimetry.

16. Verhaegen, F., Granton, P., & Tryggestad, E. (2011). Small animal radiotherapy research platforms. Physics in Medicine & Biology, 56(12), R55.

17. Verhaegen, F., Dubois, L., Gianolini, S., Hill, M. A., Karger, C. P., Lauber, K., ... & Georg, D. (2018). ESTRO ACROP: Technology for precision small animal radiotherapy research: Optimal use and challenges. Radiotherapy and Oncology, 126(3), 471-478.

18. Yahyanejad, S., van Hoof, S. J., Theys, J., Barbeau, L. M., Granton, P. V., Paesmans, K., ... & Vooijs, M. (2015). An image guided small animal radiation therapy platform (SmART) to monitor glioblastoma progression and therapy response. Radiotherapy and Oncology, 116(3), 467-472.

19. Hill, R., Healy, B., Holloway, L., Kuncic, Z., Thwaites, D., & Baldock, C. (2014). Advances in kilovoltage x-ray beam dosimetry. Physics in Medicine & Biology, 59(6), R183.

20. Chow, J. C., Leung, M. K., Lindsay, P. E., & Jaffray, D. A. (2010). Dosimetric variation due to the photon beam energy in the small-animal irradiation: A Monte Carlo study. Medical physics, 37(10), 5322-5329.

21. McGrath, A. (2020). Relative dosimetry measurements in kilovoltage X-rays with OSLDs. Physical and Engineering Sciences in Medicine, 43(1), 289-295.

22. Ehringfeld, C., Schmid, S., Poljanc, K., Kirisits, C., Aiginger, H., & Georg, D. (2005). Application of commercial MOSFET detectors for in vivo dosimetry in the therapeutic x-ray range from 80 kV to 250 kV. Physics in Medicine & Biology, 50(2), 289.

23. Damodar, J., Odgers, D., Pope, D., & Hill, R. (2018). A study on the suitability of the PTW microDiamond detector for kilovoltage x-ray beam dosimetry. Applied Radiation and Isotopes, 135, 104-109.

24. Almond, P. R., Biggs, P. J., Coursey, B. M., Hanson, W. F., Huq, M. S., Nath, R., & Rogers, D. W. (1999). AAPM's TG-51 protocol for clinical reference dosimetry of high-energy photon and electron beams. Medical physics, 26(9), 1847-1870.

25. Ma, C. M., Coffey, C. W., DeWerd, L. A., Liu, C., Nath, R., Seltzer, S. M., & Seuntjens, J. P. (2001). AAPM protocol for 40–300 kV x-ray beam dosimetry in radiotherapy and radiobiology. Medical physics, 28(6), 868-893.

Chapter 6

Summary and Conclusion

In modern radiotherapy, the increasing complexity of radiation dose delivery necessitates the use of quality assurance tools for comprehensive dose measurements[1, 2]. In this study, we commissioned a parallel-beam fiber optic CT scanner for clinical 3D radiation dosimetry. The scanner offers an efficient and accurate solution for reading 3D dosimeters. Its novel design reduces both systematic and statistical uncertainties, eliminates structural artifacts on dose images[3], and simplifies the scanning and analysis process, making 3D dosimetry more accessible for clinical applications.

In Chapter 2, we investigated the measurement uncertainty, operational procedures, and clinical utility of the novel optical CT scanner. A systematic analysis was conducted to assess the uncertainties associated with each component of the scanner. The benchmark results demonstrated promising outcomes, with maximum uncertainties within 1% for all mechanical tests. By implementing rigorous background subtraction and camera calibration techniques, the overall measurement uncertainty can be reduced to less than 1% within the optimal dose range. Through adequate background subtraction procedures, we achieved a remarkable 77% reduction in measurement uncertainty by mitigating the influence of structural artifacts, ambient light, and refractive light from the beam path. Notably, the scanner exhibited excellent reproducibility, as evidenced by the mean and standard deviation of dose differences in three repeat scans, which were smaller than 0.4% and 1.1%, respectively. For dose distribution measurements, a diverse range of treatment fields were evaluated using the developed system. The gamma comparison demonstrated a strong agreement between 3D measurements, treatment planning system calculations, and EBT3 film dosimetry. With gamma criteria of 3%/2mm and 2%/2mm, the majority of passing rates fell within the range of 98% to 100%. Overall, the findings highlight the robustness and accuracy of the optical CT scanner for clinical 3D radiation dosimetry. The system's

ability to provide reliable measurements and excellent agreement with established dosimetry methods reinforces its potential for enhancing quality assurance in modern radiotherapy practice.

To enhance the clinical utility of 3D dosimetry, we proposed a robust and accurate methodology for registering treatment planning coordinates with 3D dosimeter coordinates. In Chapter 3, we utilized fiducial-based registration to align the optical CT dose images with the simulation CT dosimeter images, establishing a correlation between the two coordinate systems. Moreover, by utilizing the fiducial coordinates, we mapped patients' anatomical structures to the dosimeter coordinates, enabling structure-by-structure 3D dose comparison. The results demonstrate that the estimated target registration error of the proposed methodology is smaller than 0.3 mm, indicating its high accuracy. With the successful registration of the measurement and planning spaces, 3D intensity-modulated radiation therapy (IMRT) quality assurance (QA) can be conducted. This enables the acquisition of measured dose-volume histograms (DVHs) for the targets and organs at risk, providing valuable information for evaluation. Additionally, the identification of gamma failing points in 3D space allows for a comprehensive assessment of dose discrepancies. This study aims to provide clinicians with more clinically relevant information for the evaluation of individual treatment plans, surpassing the limitations of traditional 2D gamma tests. By incorporating the proposed methodology, clinicians can make informed clinical judgments based on the measured DVHs and the evaluation of gamma failing points in 3D space. This approach enhances the assessment of treatment plans and supports the optimization of radiation therapy delivery, ultimately improving patient care.

To enable the application of 3D dosimetry in the end-to-end testing of radiosurgery platforms, we proposed an anthropomorphic 3D dosimetry system in Chapter 4. This system incorporates a stereotactic end-to-end verification inhomogeneous phantom (STEEV), a customized tissue-

equivalent insert, and 3D dosimeters for a comprehensive dosimetry study of intracranial radiosurgery. We aimed to investigate the feasibility of using this system to characterize a radiosurgery platform by assessing mechanical and dosimetric errors in off-axis delivery[4] and the accuracy of treatment planning dose calculation, which involves modeling small fields, out-of-field dose[5], and MLC characteristics[6]. The results demonstrated that the 3D dosimetry system has the capability to accurately measure high fractional doses up to 25 Gy and detect submillimeter mechanical errors in 3D space. Through the performance of seven benchmark plans, we observed a maximum dose distribution shift of 1.5 mm compared to the planned dose distribution when the target was positioned 7 cm off-axis. Additionally, the measured dose distribution exhibited lower DGI values and higher V10 and V12 values compared to the treatment planning. These benchmark tests provided a comprehensive evaluation of the radiosurgery platform's performance for single-isocenter multitarget treatments. The findings from these tests contribute to enhancing the current commissioning process by identifying potential machine capabilities and discrepancies between measured and planned dose distributions. By utilizing the proposed 3D dosimetry system, clinicians and physicists can have greater confidence in the accuracy and efficacy of radiosurgery treatments.

In Chapter 5 of the study, we utilized the 3D dosimetry methodology to acquire high-resolution dose measurements for small megavoltage and kilovoltage photon fields. This methodology allowed for accurate dose measurements without being influenced by energy dependence or dose rate dependence. For the megavoltage beam data measurements, we observed that when the measured field size was smaller than 1 cm, the gamma passing rates between the PRESAGE dosimeter and the treatment planning system (TPS) were lower compared to the passing rates between the PRESAGE dosimeter and radiochromic film. This suggests that discrepancies in dose

calculations for small fields may arise from the TPS. However, for field sizes of 1.2 cm and 1.5 cm, the TPS dose calculation showed good agreement with the 3D measurements. With a gamma criteria of 1%/1mm, the passing rates for PDD (percentage depth dose) and profile measurements exceeded 96% and 98.5%, respectively. All points passed the gamma criteria of 2%/2mm. In the kilovoltage study, there was overall good agreement between the PDD curves obtained from the 3D dosimeter and film measurements at depths less than 3 cm. However, at larger depths, the PRESAGE measurements showed a 3% higher depth dose compared to the vertical film measurement. This discrepancy could be attributed to misalignment between the film and the beam path, especially when measuring small treatment fields. Furthermore, variations in the kilovoltage photon beam spectrum occur with depth due to the atomic number properties of PRESAGE, which further contribute to this inconsistency. The 3D dosimetry measurements demonstrated their efficiency compared to other 2D or point dose measurements, as comprehensive beam data could be acquired using a single dosimeter and a single optical CT scan. The 3D dosimeter itself closely resembled water-equivalent material, eliminating the need for correction factors. By employing the 3D dosimetry methodology described in Chapter 5, we can obtain accurate and comprehensive dose measurements for small megavoltage and kilovoltage photon fields.

References or Bibliography

1. Klein, E. E., Hanley, J., Bayouth, J., Yin, F. F., Simon, W., Dresser, S., ... & Holmes, T. (2009). Task Group 142 report: Quality assurance of medical accelerators a. Medical physics, 36(9Part1), 4197-4212.

2. Bissonnette, J. P., Balter, P. A., Dong, L., Langen, K. M., Lovelock, D. M., Miften, M., ... & Yoo, S. (2012). Quality assurance for image-guided radiation therapy utilizing CT-based technologies: a report of the AAPM TG-179. Medical physics, 39(4), 1946-1963.

3. Oldham, M., & Kim, L. (2004). Optical-CT gel-dosimetry II: Optical artifacts and geometrical distortion. Medical physics, 31(5), 1093-1104.

4. Prentou, G., Pappas, E. P., Logothetis, A., Koutsouveli, E., Pantelis, E., Papagiannis, P., & Karaiskos, P. (2020). Dosimetric impact of rotational errors on the quality of VMAT-SRS for multiple brain metastases: comparison between single-and two-isocenter treatment planning techniques. Journal of Applied Clinical Medical Physics, 21(3), 32-44.

5. Huang, J. Y., Followill, D. S., Wang, X. A., & Kry, S. F. (2013). Accuracy and sources of error of out-of field dose calculations by a commercial treatment planning system for intensity-modulated radiation therapy treatments. Journal of applied clinical medical physics, 14(2), 186-197.

6. 6.Vieillevigne, L., Khamphan, C., Saez, J., & Hernandez, V. (2019). On the need for tuning the dosimetric leaf gap for stereotactic treatment plans in the Eclipse treatment planning system. Journal of applied clinical medical physics, 20(7), 68-77.

Chapter 7

Suggestions for Future Study

While the parallel-beam optical CT scanner with a fiber optic taper has significantly improved the readout process of 3D dosimeters and enhanced the accuracy and efficiency of 3D dosimetry, there are a few limitations that could be addressed in future studies. One such limitation is the dynamic range of the CCD camera, which refers to the ratio of the maximum possible signal to the dark noise signal. In certain high-dose measurements, the dynamic range of the camera may not be sufficient. This can result in signal saturation, where the measured signal exceeds the camera's capacity to accurately record it, or weak signals close to the level of dark noise on the projection images. Signal saturation can lead to erroneous dose measurements, while weak signals can result in measurements with a poor signal-to-noise ratio. To mitigate these limitations, the current system allows for the adjustment of exposure time to ensure that the measured signal has an adequate signal-to-noise ratio. However, this adjustment may also lead to signal saturation in the background or low-dose regions, which can affect the accuracy of the measurements in those areas. To address these limitations in future studies, improvements can be made to expand the dynamic range of the CCD camera, allowing for more accurate and reliable measurements across a wider signal range.

To increase the clinical utility of the developed optical CT scanner, two important areas for improvement can be focused on. Firstly, expanding the field-of-view of the optical scanner to cover the entire treatment field is crucial. This can be achieved through advancements in various components, including a broader beam source, an enlarged water tank, a larger 3D dosimeter, and an optic fiber taper with an increased taper ratio. By extending the field-of-view, the optical scanner can capture a more comprehensive representation of the dose distribution, enabling accurate measurements for larger treatment fields. Secondly, the current reliance on a matching liquid in the water tank to mitigate reflection and refraction effects presents practical challenges.

The liquid needs to be maintained at room temperature and may need to be replaced regularly, which can be labor-intensive and time-consuming. Therefore, innovative ways to mitigate reflection and refraction without the need for a matching liquid should be explored. This would simplify the scanning process and reduce the maintenance efforts associated with liquid replacement, making the optical CT scanner more convenient and efficient for clinical application.

To enhance the tomographic image quality and mitigate streaks and ring artifacts, the use of an iterative algorithm instead of the commonly employed filtered backprojection (FBP) method is recommended. Previous studies have demonstrated the superiority of an ordered subsets (OS)-based simultaneous algebraic reconstruction technique (SART) with total variation (TV) minimization over FBP methods. This approach effectively reduces noise, preserves spatial gradients, and suppresses artifacts, all while maintaining image resolution and accuracy. Moreover, optimizing the hardware and 3D dosimeters can contribute to increased signal-to-noise ratio. CCD binning, which combines charge packets from adjacent pixels, significantly reduces the impact of read noise by amplifying the signal. Additionally, the sensitivity of the 3D dosimeter can be optimized to measure the specific dose range of interest by adjusting its formulation. These improvements in both software and hardware components can lead to improved image quality and enhance the overall performance of the optical CT scanner.

The current implementation of 3D dosimetry is limited to relative dosimetry and does not provide accurate absolute dose measurements. To achieve precise absolute dosimetry, it is essential to improve the reproducibility of measurements and reduce intra- and inter-dosimeter variability, as these factors directly impact the calibration accuracy of the dosimeters. The optical CT scanner developed in this study has demonstrated measurement reproducibility within 1%, which is a significant improvement. However, further advancements are required to enhance the intra- and

inter-dosimeter variability. One challenge related to dosimeter variability is their sensitivity to light and high temperatures, which can result in variations during dosimeter storage and transportation. Additionally, precise formulation and ambient condition during curing process are necessary to ensure uniform intra- and inter-dosimeter sensitivity. Addressing these issues can contribute to reducing dosimeter differences and improving the accuracy of absolute dose measurements. The availability of absolute dosimetry would allow the 3D dosimeters to determine the exact delivered dose instead of relative percentages. This enhancement would significantly increase the utility and applicability of 3D dosimetry in clinical practice.

In the rapidly evolving field of Radiation Oncology, advanced quality assurance tools are essential to address the increasing complexity of treatment delivery and ensure accurate and safe radiation treatments. The commissioned 3D dosimetry system holds tremendous potential for future applications in the clinic and research settings. It can provide a comprehensive view of patients' treatment plans and dosimetric characteristics, instilling confidence in clinicians and minimizing the risk of radiation incidents. In the future, studies exploring various avenues to maximize the system's potential will be conducted.